

Научном већу Института за физику у Београду

Београд, 28. 11. 2018.

Предмет: Покретање поступка за избор у звање истраживач сарадник

Молим Научно веће Института за физику у Београду да покрене поступак за мој избор у звање истраживач сарадник.

У прилогу достављам:

1. мишљење руководиоца пројекта са предлогом комисије за избор у звање;
2. стручну биографију;
3. преглед научне активности;
4. списак и копије објављених научних радова и других публикација;
5. уверење о последњем овереном и уписаном семестру на докторским студијама;
6. фотокопију диплома са основних и мастер студија;
7. потврду о прихватању предлога теме докторске дисертације.

С поштовањем,

Ана Худомал
истраживач приправник

Ana Hudomal

Научном већу Института за физику у Београду

Београд, 20. новембар 2018. године

Предмет: Мишљење руководиоца пројекта о избору Ане Худомал у звање истраживач сарадник

Ана Худомал је запослена у Лабораторији за примену рачунара у науци, у оквиру Националног центра изузетних вредности за изучавање комплексних система Института за физику у Београду и ангажована је на пројекту основних истраживања Министарства просвете, науке и технолошког развоја Републике Србије ОН171017, под називом "Моделирање и нумеричке симулације сложених вишечестичних физичких система". На поменутом пројекту ради на темама из физике ултрахладних квантних гасова у присуству јаких синтетичких магнетних поља под руководством др Иване Васић. С обзиром да испуњава све предвиђене услове у складу са Правилником о поступку, начину вредновања и квантитативном исказивању научноистраживачких резултата истраживача МПНТР, сагласан сам са покретањем поступка за избор Ане Худомал у звање истраживач сарадник.

За састав комисије за избор Ане Худомал у звање истраживач сарадник предлажем:

- (1) др Ивана Васић, виши научни сарадник, Институт за физику у Београду,
- (2) др Антун Балаж, научни саветник, Институт за физику у Београду,
- (3) доц. др Божидар Николић, доцент Физичког факултета Универзитета у Београду.



др Антун Балаж
научни саветник
руководилац пројекта ОН171017

Биографија Ане Худомал

Ана Худомал је рођена 8. 3. 1991. године у Београду, где је завршила основну школу и Математичку гимназију. Основне академске студије на Физичком факултету Универзитета у Београду, смер Теоријска и експериментална физика, започела је 2010. године и завршила јула 2014. године са просечном оценом 10,0. Мастер академске студије на истом факултету, смер Теоријска и експериментална физика, завршила је октобра 2015. године са просечном оценом 10,0, одбранивши мастер рад на тему „New Periodic Solutions to the Three-Body Problem and Gravitational Waves” („Нова периодична решења проблема три тела и гравитациони таласи”). Мастер рад је урађен под руководством др Вељка Дмитрашиновића, научног саветника Института за физику у Београду.

Од 2007. до 2011. године Ана Худомал је била стипендиста Републичке фондације за развој научног и уметничког подмлатка, затим од 2011. до 2013. стипендиста града Београда, док је од 2013. до 2015. била стипендиста Фонда за младе таленте Републике Србије. Ана Худомал је током академске 2014/2015. године учествовала у извођењу наставе на Физичком факултету Универзитета у Београду, као сарадник у настави на предмету Квантна теоријска физика (предметни наставник доц. др Душко Латас).

Новембра 2015. године уписала је докторске академске студије на Физичком факултету Универзитета у Београду, ужа научна област физика кондензоване материје. Под руководством др Иване Васић ради на темама везаним за ултрахладне квантне гасове у оптичким решеткама са синтетичким магнетним пољима, са циљем разумевања улоге атомских интеракција у овим системима. Од марта 2016. године Ана Худомал је запослена у Институту за физику у Београду као истраживач приправник у Лабораторији за примену рачунара у науци, у оквиру Националног центра изузетних вредности за изучавање комплексних система, на пројекту основних истраживања „*Моделирање и нумеричке симулације сложених вищечестичних система*” (ОН171017) Министарства просвете, науке и технолошког развоја Републике Србије, којим руководи др Антун Балаж. Поред тога, учествовала је и на билатералним пројектима са Немачком (Гете универзитет у Франкфурту) и са Хрватском (Универзитет у Загребу), под руководством др Иване Васић. До сада је похађала неколико школа за докторанде, међу којима су International School on Thermal, Quantum, and Topological Phase Transitions – Bad Endorf, Germany (2016), Winter School on Topological Matter in Artificial Gauge Fields – Dresden, Germany (2018), ICAP2018 Summer School – Barcelona, Spain (2018).

До сада, Ана Худомал има један рад објављен у часопису категорије M21a, два рада објављена у часописима категорије M21, као и 5 саопштења са међународних скупова штампаних у изводу (M34).

Преглед научне активности Ане Худомал

Током мастер студија, истраживање Ане Худомал било је фокусирано на проналажење и карактеризацију периодичних решења за класичан проблем три тела која међусобно интерагују гравитационом силом. Њутнов проблем три тела је један од најстаријих нерешених проблема физике и математике, формулисан у 17. веку, а до првих решења за периодичне орбите дошли су Ојлер и Лагранж у 18. веку. У последњим деценијама употреба модерних рачунара је омогућила интензиван нумерички приступ и систематизацију нових класа решења. У сарадњи са др Вељком Дмитрашиновићем и др Милованом Шуваковом са Института за физику у Београду, Ана Худомал је испитивала гравитационе таласе које би емитовала три тела која се крећу по новооткривеним орбитама и показала да би овакви системи могли бити извори детектабилних сигнала. Поред тога, Ана је радила на проналажењу нових периодичних орбита, као и на потврди и објашњењу линеарне везе између периода орбите и броја симбола у алгебарском опису њене топологије, која представља уопштену верзију трећег Кеплеровог закона.

На докторским студијама, под руководством др Иване Васић са Института за физику у Београду, Ана Худомал се у свом научном раду бави особинама ултрахладних квантних гасова у присуству јаких синтетичких магнетних поља. Проучавање ултрахладних квантних гасова је важна тема савремене физике. Настанак ове области је подстакнут потрагом за Бозе-Ајнштајн кондензатом - стањем које је предвиђено постулатима квантне статистичке физике уведеним почетком двадесетог века. Први Бозе-Ајнштајн кондензати у системима ултрахладних атома су остварени 1995. године и овај успех је награђен Нобеловом наградом за физику 2001. године. У раним експериментима коришћени су слабо интерагујући бозонски атоми, што је одговарајући режим за постизање кондензата. Данас се у системима ултрахладних атома проучавају различити физички режими, што ове системе чини правим квантним симулаторима. Посебно је интересантно што се у овим системима јачина и тип међуатомских интеракција могу контролисати, па интеракције могу бити слабе или јаке, кратко- или дугодометне. Увођењем стојећих светлосних таласа реализовани су периодични потенцијали за атоме, што је омогућило проучавање модела налик моделима физике чврстог стања. Ипак, компонента која је дуго била недоступна је јако синтетичко магнетно поље, које може да делује на неутралне атоме кроз Лоренцову силу. Почев од 2013. године, јака синтетичка магнетна поља се успешно реализују у периодично вођеним оптичким решеткама. На овај начин може се реализовати један од основних модела физике кондензованог стања, Харпер-Хофштетер модел. Важна карактеристика овог модела су тополошке инваријанте енергетских зона, тзв. Чернови бројеви, који су у основи квантног Холовог ефекта.

Недавно мерење Черновог броја је прекретница која је означила реализацију тополошке енергетске зоне у системима хладних атома. Подстакнута овим експериментом, Ана Худомал је истраживала одговор некохерентних бозона на спољашњу силу у вођеним оптичким решеткама. Применом апроксимативног аналитичког развоја по инверзној фреквенцији вођења, кандидаткиња је показала присуство додатних чланова у ефективном Хамилтонијану и испитала њихов утицај на тополошке

карактеристике ефективног Хамилтонијана. Главни фокус овог истраживања је био на улози слабих атомских интеракција, које су укључене у опис употребом теорије средњег поља. Користећи нумеричке симулације и аналитичке увиде, кандидаткиња је утврдила да интеракције доприносе атомским прелазима између различитих енергетских зона ефективног модела, чиме се усложњава експериментална процедура у складу са очекивањима. Међутим, добијени резултати такође показују да слабе атомске интеракције олакшавају мерење Черновог броја на неколико начина. Како се очекује да мерење Черновог броја постане рутински алат у блиској будућности - први корак у припреми занимљивијих тополошких фаза - досада добијени резултати везани за ефекте слабих интеракција су од значаја и за будуће експерименте.

Списак публикација Ане Худомал

Радови у међународним часописима изузетних вредности (категорија M21a):

1. V. Dmitrašinović, M. Šuvakov, and **A. Hudomal**,
Gravitational Waves from Periodic Three-Body Systems,
Phys. Rev. Lett. **113**, 101102 (2014) [ISSN=1079-7114, IF(2014)=7.512].

Радови у врхунским међународним часописима (категорија M21):

1. **A. Hudomal**, I. Vasić, H. Buljan, W. Hofstetter, and A. Balaž,
Dynamics of weakly interacting bosons in optical lattices with flux,
Phys. Rev. A **98**, 053625 (2018) [ISSN=2469-9934, IF(2017)=2.909].
2. V. Dmitrašinović, **A. Hudomal**, M. Shibayama, and A. Sugita,
Linear Stability of Periodic Three-body Orbits with Zero Angular Momentum and
Topological Dependence of Kepler's Third Law: a Numerical Test,
J. Phys. A: Math. Theor. **51**, 315101 (2018) [ISSN=1751-8121, IF(2017)=1.963].

Саопштења са међународног скупа штампана у изводу (M34):

1. **A. Hudomal**, I. Vasić, H. Buljan, W. Hofstetter, and A. Balaž, Transport in optical lattices with flux, 26th International Conference on Atomic Physics, 22 - 27 July 2018, Barcelona, Spain.
2. **A. Hudomal**, I. Vasić, H. Buljan, W. Hofstetter, and A. Balaž, Artificial gauge potentials in periodically driven optical lattices: numerical simulations of atomic transport, DPG Spring Meeting, 5 - 9 March 2018, Erlangen, Germany.
3. **A. Hudomal**, I. Vasić, H. Buljan, W. Hofstetter, and A. Balaž, Transport in optical lattices with flux, Winter School on Topological Matter in Artificial Gauge Fields, 26 February - 6 March 2018, Dresden, Germany.
4. **A. Hudomal**, I. Vasić, H. Buljan, W. Hofstetter, and A. Balaž, Transport dynamics in optical lattices with flux, The 6th International School and Conference on Photonics, 28 August - 1 September 2017, Belgrade, Serbia.
5. **A. Hudomal**, I. Vasić, W. Hofstetter, and A. Balaž, Transport dynamics in optical lattices with flux, DPG Spring Meeting, 6 - 10 March 2017, Mainz, Germany.



Gravitational Waves from Periodic Three-Body Systems

V. Dmitrašinović and Milovan Šuvakov

Institute of Physics, University of Belgrade, Pregrevica 118, Zemun, Post Office Box 57, 11080 Beograd, Serbia

Ana Hudomal

Fizički fakultet, University of Belgrade, Studentski Trg 12, 11000 Belgrade, Serbia

(Received 30 May 2014; revised manuscript received 14 July 2014; published 4 September 2014)

Three bodies moving in a periodic orbit under the influence of Newtonian gravity ought to emit gravitational waves. We have calculated the gravitational radiation quadrupolar waveforms and the corresponding luminosities for the 13 + 11 recently discovered three-body periodic orbits in Newtonian gravity. These waves clearly allow one to distinguish between their sources: all 13 + 11 orbits have different waveforms and their luminosities (evaluated at the same orbit energy and body mass) vary by up to 13 orders of magnitude in the mean, and up to 20 orders of magnitude for the peak values.

DOI: 10.1103/PhysRevLett.113.101102

PACS numbers: 04.30.Db, 04.25.Nx, 95.10.Ce, 95.30.Sf

Direct detection of gravitational waves [1,2] ought to come about in the foreseeable future, due to the substantial effort made at the operational and/or pending detectors. One of the most promising candidates for astrophysical sources of gravitational waves are the coalescing, i.e., inspiraling and finally merging binary compact stars [3,4]. Binary coalescence is the only source for which there is a clear prediction of the signal and an estimate of the detection distance limit, as general relativists have completed numerical simulations of mergers of compact binaries, such as neutron stars and/or black holes, Refs. [5–7].

Slowly changing, quasiperiodic two-body orbits are weak sources of gravitational radiation, Refs. [8,9]—only accelerated collapse leads to an increase in energy loss. The major part of the emitted energy in a binary coalescence comes from the final merger of two neutron stars, or black holes, that produces an intense burst of gravitational radiation. Of course, such mergers are one-off events, never to be repeated in the same system, so their detection is subject to their (poorly known) distribution in our Galaxy. It is therefore interesting to look for periodic sources of intense gravitational radiation.

There is now a growing interest in three-body systems as astrophysical sources of gravitational waves, Refs. [10–12]. These early works did not find a substantial increase in the luminosity (emitted power) from representative three-body orbits belonging to three families that were known at the time, Refs. [13–22], over the luminosity from a comparable periodic two-body system [23]. The luminosity of a (quadrupolar) gravitational wave is proportional to the square of the third time derivative of the quadrupole moment, see Refs. [8,9], which, in turn, is sensitive to close approaches of two bodies in a periodic orbit [24]. Thus, getting as close as possible to a two-body collision without actually being involved in one, is a desirable property of the radiating system.

Recently 13 new distinct periodic orbits belonging to 12 (new) families have been discovered in Ref. [25], as well as 11 “satellite orbits” in the figure-eight family [26]. Some of these three-body orbits pass very close to binary collisions and yet avoid them, so they are natural candidates for periodic sources of intense gravitational radiation.

In this Letter we present our calculations of quadrupolar waveforms, Fig. 1, and of luminosities, see Table I and Fig. 2 of gravitational radiation emitted by the 13 + 11 recently discovered periodic three-body gravitating orbits, Refs. [25,26]. We have also calculated waveforms of all published Broucke-Hadjidemetriou-Henon (BHH) orbits [14–20], which we omit from this Letter for the sake of brevity, and because they are closely related to Henon’s “criss-cross” one, studied in Ref. [10]. The waves of the 13 + 11 new orbits show clear distinctions in form and luminosity, thus ensuring that they would be distinguishable (provided their signals are strong enough to be detected).

We consider systems of three equal massive particles moving periodically in a plane under the influence of Newtonian gravity. The quadrupole moment I_{ij} of three bodies with equal masses $m_n = m$, ($n = 1, 2, 3$) is expressed as $I_{ij} = \sum_{n=1}^3 m x_n^i x_n^j$, where x_n^i is the location of n th body, and the spatial dimension indices i and j run from 1 to 3 (with $x^1 = x$, $x^2 = y$, $x^3 = z$). The reduced quadrupole Q_{ij} is defined as $Q_{ij} = I_{ij} - \frac{1}{3} \delta_{ij} \sum_{k=1}^3 I_{kk}$. The gravitational waveforms denoted by h_{ij}^{TT} are, asymptotically,

$$h_{ij}^{TT} = \frac{2G}{rc^4} \frac{d^2 Q_{ij}}{dt^2} + \mathcal{O}\left(\frac{1}{r^2}\right), \quad (1)$$

where r is the distance from the source, Refs. [8,9]. Here, TT means (i) transverse ($\sum_{i=1}^3 h_{ij}^{TT} \hat{n}^i = 0$) and (ii) traceless ($\sum_{i=1}^3 h_{ii}^{TT} = 0$), where \hat{n}_i denotes the unit vector of the gravitational wave’s direction of propagation. The two

TABLE I. Initial conditions and periods of three-body orbits. $\dot{x}_1(0)$, $\dot{y}_1(0)$ are the first particle's initial velocities in the x and y directions, respectively, T is the period of the (rescaled) orbit to normalized energy $E = -1/2$, Θ is the rotation angle (in radians) and $\langle P \rangle$ is the mean luminosity (power) of the waves emitted during one period. Other two particles' initial conditions are specified by these two parameters, as follows: $x_1(0) = -x_2(0) = -\lambda$, $x_3(0) = 0$, $y_1(0) = y_2(0) = y_3(0) = 0$, $\dot{x}_2(0) = \dot{x}_1(0)$, $\dot{x}_3(0) = -2\dot{x}_1(0)$, $\dot{y}_2(0) = \dot{y}_1(0)$, $\dot{y}_3(0) = -2\dot{y}_1(0)$. The Newtonian coupling constant G is taken as $G = 1$ and the masses are equal $m_{1,2,3} = 1$.

Name	$\dot{x}_1(0)$	$\dot{y}_1(0)$	λ	T	$\Theta(\text{rad})$	$\langle P \rangle$
Moore's figure eight	0.216 343	0.332 029	2.574 29	26.128	0.245 57	1.35×10^0
Simo's figure eight	0.211 139	0.333 568	2.583 87	26.127	0.277 32	1.36×10^0
(M8) ⁷	0.147 262	0.297 709	3.008 60	182.873	0.269 21	2.46×10^0
I.A.1 butterfly I	0.147 307	0.060 243	4.340 39	56.378	0.034 78	1.35×10^5
I.A.2 butterfly II	0.196 076	0.048 690	4.016 39	56.375	0.066 21	5.52×10^6
I.A.3 bumblebee	0.111 581	0.355 545	2.727 51	286.192	-1.090 4	1.01×10^5
I.B.1 moth I	0.279 332	0.238 203	2.764 56	68.464	0.899 49	5.25×10^2
I.B.2 moth II	0.271 747	0.280 288	2.611 72	121.006	1.138 78	1.87×10^3
I.B.3 butterfly III	0.211 210	0.119 761	3.693 54	98.435	0.170 35	3.53×10^5
I.B.4 moth III	0.212 259	0.208 893	3.263 41	152.330	0.503 01	7.48×10^5
I.B.5 goggles	0.037 785	0.058 010	4.860 23	112.129	-0.406 17	1.33×10^4
I.B.6 butterfly IV	0.170 296	0.038 591	4.226 76	690.632	0.038 484	1.23×10^{13}
I.B.7 dragonfly	0.047 479	0.346 935	2.880 67	104.005	-0.406 199	1.25×10^6
II.B.1 yarn	0.361 396	0.225 728	2.393 07	205.469	-1.015 61	2.33×10^6
II.C.2a yin-yang I	0.304 003	0.180 257	2.858 02	83.727	0.659 242	1.31×10^5
II.C.2b yin-yang I	0.143 554	0.166 156	3.878 10	83.727	-0.020 338	1.31×10^5
II.C.3a yin-yang II	0.229 355	0.181 764	3.302 84	334.877	0.472 891	7.19×10^{10}
II.C.3b yin-yang II	0.227 451	0.170 639	3.366 76	334.872	0.254 995	7.19×10^{10}

independent waveforms $h_{+,x}$ of a quadrupolar gravitational wave propagating along the z axis, Refs. [8,9] can be expressed as

$$h_+ = \frac{2G}{c^4 r} \sum_{i=1}^3 m_i (\dot{x}_i^2 + x_i \ddot{x}_i - \dot{y}_i^2 - y_i \ddot{y}_i), \quad (2)$$

$$h_x = \frac{2G}{c^4 r} \sum_{i=1}^3 m_i (\ddot{x}_i y_i + 2\dot{x}_i \dot{y}_i + x_i \ddot{y}_i), \quad (3)$$

where r denotes the distance from the source to the observer. We set the units of $G = c = m = 1$ throughout this Letter.

Here the coordinate axes x and y are chosen so that they coincide with the orbits' two (reflection) symmetry axes, when they exist, i.e., when the orbits are from class I, as defined in Ref. [25]. Otherwise, e.g., when only a single point reflection symmetry exists, as in class II orbits, the x , y axes are taken to be the eigenvectors of the moment-of-inertia tensor. The rotation angle necessary for each orbit to be aligned with these two axes is given in Table I [27].

The first gravitational radiation waveforms for periodic three-body systems were studied in Refs. [10–12]. They calculated the quadrupole radiation waveforms for three periodic orbits of the following three-equal-mass systems: (i) of the Lagrange “equilateral triangle” orbit [13], (ii) of Henon's “criss cross” [19], and (iii) of Moore's “figure eight” [21]. These three orbits are characteristic

representatives of the (only) three families of periodic three-body orbits known at the time. Reference [10] found distinct gravitational waveforms for each of the three families, thus suggesting that one might be able to distinguish between different three-body systems as sources of gravity waves by looking at their waveforms [28].

In the meantime 13 + 11 new orbits belonging to 12 new families have been found, Refs. [25,26]. The families of three-body orbits can be characterized by their topological properties viz. the conjugacy classes of the fundamental group, in this case, the free group on two letters (a , b), Ref. [29]. The free group element tells us the number of times the system's trajectory on the shape sphere passes around one or another (prechosen) two-body collision point within one period. Every time the system is close to a two-body collision the (relative) velocities, accelerations, and the third derivatives of relative coordinates increase, so that the luminosity of gravitational radiation also increases; i.e., there is a burst of gravitational radiation. This argument can be made more quantitative by appealing to two-body results of Ref. [8], as is shown in footnote [30].

We show the gravitational radiation waveforms $h_{+,x}$ in Fig. 1, emitted by three massive bodies moving according to the orbits from Refs. [25,26] belonging to these families, where Eqs. (2) and (3) are used as the definitions of the two waveforms.

First, we note that all of the calculated three-body orbits' waveforms are distinct [31], thus answering (in the

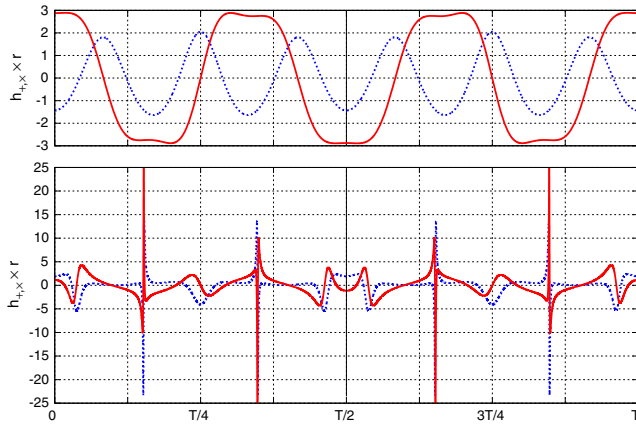


FIG. 1 (color online). The gravitational radiation quadrupolar waveforms $h_{+, \times} \times r$ as functions of the elapsed time t in units of the period T , for two periodic three-body orbits (in units of Gm/c^2 ; we have set $G = m = c = 1$ throughout this Letter) and r is the radial distance from the source to the observer. Dotted (blue) and solid (red) curves denote the $+$ and \times modes, respectively. Top: Simo's figure eight, Ref. [22]; and bottom: orbit I.B.1 Moth I. Note the symmetry of these two graphs under the (time-)reflection about the orbits' midpoint $T/2$ during one period T .

positive) the question about their distinguishability posed in Ref. [10]. In Fig. 1 we also show the gravitational waveform of one "old" orbit: Simo's figure eight, (discovered in 2002) belonging to the figure-eight family. Simo's figure eight is an important example, as it is virtually

indistinguishable from Moore's one, and yet the two have distinct gravitational waveforms, see our Fig. 1, and Fig. 2 in Ref. [10]. That is so because these two figure-eight solutions have distinct time dependences of the hyperradius R , where $R^2 \sim (1/m)\delta_{ij}\sum_{k=1}^3 I_{kk}$, so that the two orbits have different quadrupolar waveforms.

Note, moreover, the symmetry of the waveforms in Fig. 1 with respect to reflections of time about the midpoint of the period $T/2$: this is a consequence of the special subset of initial conditions (vanishing angular momentum and passage through the Euler point on the shape sphere) that we used. There are periodic three-body orbits, such as those from the BHH family, that do not have this symmetry.

The gravitational waveforms' maxima range from 20 to 50 000 in our units, with the energy fixed at $E = -1/2$. This large range of maximal amplitudes is due to the differences in the proximity of the approach to two-body collisions in the corresponding orbits. One can explicitly check that the bursts of gravitational radiation during one period correspond to close two-body approaches.

As stated above, the (negative) mean power loss $\langle dE/dt \rangle$ of the three-body system, or the (positive) mean luminosity (emitted power) of quadrupolar gravitational radiation $\langle P \rangle$, averaged over one period, is proportional to the square of the third time derivative of the (reduced) quadrupole moment $Q_{jk}^{(3)}$, $\langle dE/dt \rangle = -\langle P \rangle = -\frac{1}{5}(G/c^5)\sum_{j,k=1}^3 \langle Q_{jk}^{(5)} \dot{Q}_{jk} \rangle = -\frac{1}{5}(G/c^5)\sum_{j,k=1}^3 \langle Q_{jk}^{(3)} \ddot{Q}_{jk}^{(3)} \rangle$, (for an original derivation see Refs. [8,9], for pedagogical ones, see Refs. [1,2]). But,

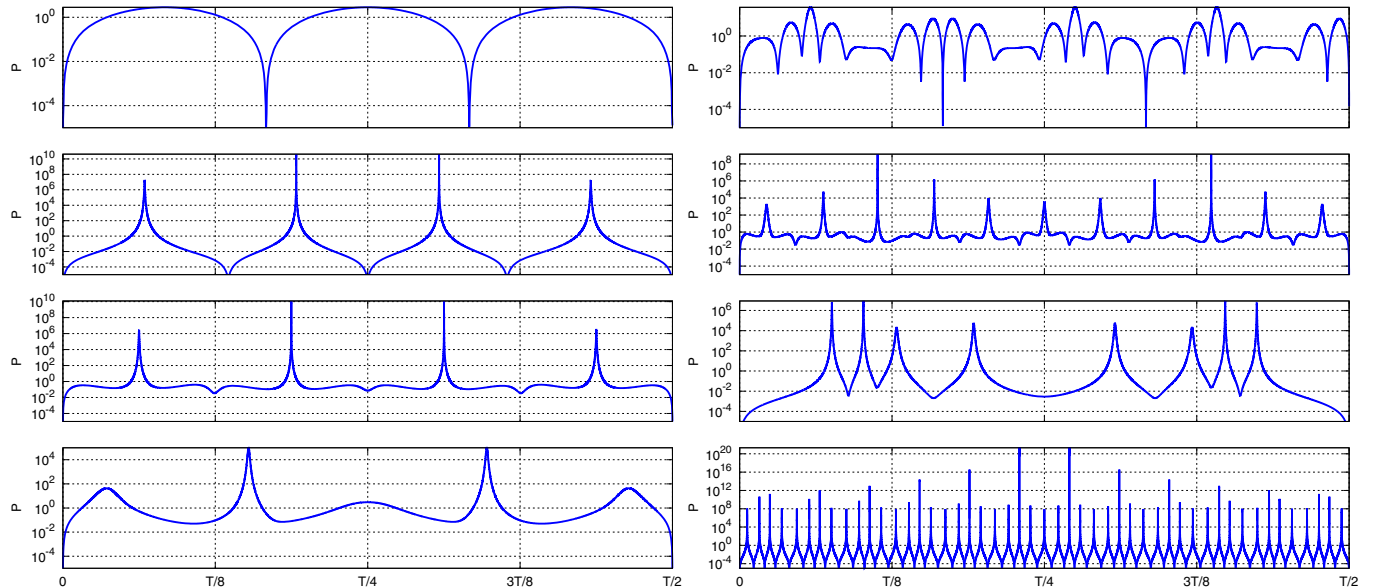


FIG. 2 (color online). The instantaneous (time unaveraged) luminosity P of quadrupolar gravitational radiation emitted from periodic three-body orbits as a function of the elapsed time t in units of the period T . Note the logarithmic scale for the luminosity P (y axis). Top left: Moore's figure eight; second from top left: I.A.2 butterfly II; third from top left: II.B.7 dragonfly; bottom left: I.B.1 moth I; top right: $(M8)^7$; second from top right: I.A.3 bumblebee; second from bottom right: I.B.5 goggles; bottom right: II.B.6 butterfly IV.

$Q_{jk}^{(3)}$ are proportional to the first time derivatives of the gravitational waveforms $Q_{jk}^{(3)} = (d/dt)Q_{jk}^{(2)} \propto (d/dt)h_{+, \times}$. The peak amplitudes of gravitational waveforms $h_{+, \times}$, in turn, grow in the vicinity of two-body collisions [30], which explains the burst of gravitational radiation as one approaches a two-body collision point.

The mean and instantaneous luminosities, expressed in our units, of these orbits, normalized to $E = -1/2$, are shown in Table I and Fig. 2, respectively. Note that in Table I we show only three orbits belonging to the figure-eight family: Moore's, Simo's, and the stable choreography (M8)⁷; they have all the same order of magnitude of the mean luminosity [32], whereas the butterfly I and butterfly II orbits, which belong to the same topological family, have mean luminosities that differ by more than a factor of 40.

Generally, the mean luminosities of these orbits cover 13 orders of magnitude, ranging from 1.35 (Moore's figure eight) to 1.23×10^{13} (I.B.6 butterfly IV) in our units; see Table I. The peak instantaneous luminosities have an even larger range: 20 orders of magnitude; see Fig. 2. Here, the symmetric form of the instantaneous (time unaveraged) power $P = \frac{1}{5}(G/c^5) \sum_{j,k=1}^3 Q_{jk}^{(3)} Q_{jk}^{(3)}$ was used. This gives us hope that at least some of these three-body periodic orbits can, perhaps, lead to detectable gravitational radiation signals.

It is a different question if some or all of these sources of gravitational radiation would be observable by the present-day and the soon-to-be-built gravitational wave detectors: that strongly depends on the absolute values of the masses, velocities, and the average distances between the three celestial bodies involved, as well as on the distribution of such sources in our Galaxy.

Moreover, note that all of the newly found and analyzed three-body orbits have zero angular momentum, and many of them are unstable. It is well known [16–20] that by changing the angular momentum within the same family of three-body orbits, the stability of an orbit changes as well. So, it may happen that a previously stable orbit turns into an unstable one, and vice versa. For this reason it should be clear that a careful study of gravitational-radiation-induced energy- and angular-momentum dissipation is necessary for these orbits [33]. Moreover, if realistic results are to be obtained, post-Newtonian approximations will have to be applied in the future. Such relativistic corrections are most important at large velocities, i.e., precisely near close approaches that are so crucial for large gravitational radiation. Thus, the present Letter is meant only to highlight the possibilities in this field, and should be viewed as an invitation to join in the more realistic future studies.

V.D. and M. Š. were financially supported by the Serbian Ministry of Science and Technological Development under Grants No. OI 171037 and No. III 41011. A.H. was supported by the City of Belgrade

studentship (Gradska stipendija grada Beograda) during the year 2012-2013, and was a recipient of the "Dositeja" stipend for the year 2013-2014, from the Fund for Young Talents (Fond za mlade talente -stipendija "Dositeja") of the Serbian Ministry for Youth and Sport.

-
- [1] C. W. Misner, K. S. Thorne, and J. A. Wheeler, *Gravitation* (Freeman, San Francisco, CA, 1973).
 - [2] A. P. Lightman, W. H. Press, R. H. Price, and S. A. Teukolsky, *Problem Book in Relativity and Gravitation* (Princeton University Press, Princeton, NJ, 1975).
 - [3] C. Cutler *et al.*, *Phys. Rev. Lett.* **70**, 2984 (1993).
 - [4] C. Cutler and K. S. Thorne, in *General Relativity and Gravitation: Proceedings of the 16th International Conference*, edited by N. T. Bishop and S. D. Maharaj (World Scientific, Singapore, 2002), p. 72.
 - [5] M. Campanelli, C. O. Lousto, P. Marronetti, and Y. Zlochower, *Phys. Rev. Lett.* **96**, 111101 (2006).
 - [6] J. G. Baker, J. Centrella, D.-I. Choi, M. Koppitz, and J. van Meter, *Phys. Rev. Lett.* **96**, 111102 (2006).
 - [7] F. Pretorius, *Phys. Rev. Lett.* **95**, 121101 (2005).
 - [8] P. C. Peters and J. Mathews, *Phys. Rev.* **131**, 435 (1963).
 - [9] P. C. Peters, *Phys. Rev.* **136**, B1224 (1964).
 - [10] Y. Torigoe, K. Hattori, and H. Asada, *Phys. Rev. Lett.* **102**, 251101 (2009).
 - [11] T. Chiba, T. Imai, and H. Asada, *Mon. Not. R. Astron. Soc.* **377**, 269 (2007).
 - [12] H. Asada, *Phys. Rev. D* **80**, 064021 (2009).
 - [13] J. L. Lagrange, *Miscellanea Taurinensia* **4**, 118 (1772); *Oeuvres* **2**, 67; *Mécanique Analytique*, 262; 2nd ed. **2**, 108; *Oeuvres* **12**, 101.
 - [14] R. Broucke and D. Boggs, *Celest. Mech.* **11**, 13 (1975).
 - [15] R. Broucke, *Celest. Mech.* **12**, 439 (1975).
 - [16] J. D. Hadjidemetriou, *Celest. Mech.* **12**, 155 (1975).
 - [17] J. D. Hadjidemetriou and Th. Christides, *Celest. Mech.* **12**, 175 (1975).
 - [18] J. D. Hadjidemetriou, *Celest. Mech.* **12**, 255 (1975).
 - [19] M. Henon, *Celest. Mech.* **13**, 267 (1976).
 - [20] M. Henon, *Celest. Mech.* **15**, 243 (1977).
 - [21] C. Moore, *Phys. Rev. Lett.* **70**, 3675 (1993).
 - [22] C. Simó, in *Celestial Mechanics*, edited by A. Chenciner, R. Cushman, C. Robinson, and Z. J. Xia (Am. Math. Soc., Providence, RI, 2002).
 - [23] The question of distinguishability between various three-body and two-body sources' of gravitational radiation was also raised in Ref. [10].
 - [24] The proximity to a two-body collision can be defined mathematically by using the so-called hyperspherical variables, and the shape-sphere variables, in particular; see Refs. [25,29]. Of course, it is not just the proximity to the two-body collision point that is driving this surge of emitted power, but also the accompanying increase in the velocities, accelerations, and third derivatives of the relative positions; see the text below.
 - [25] Milovan Šuvakov and V. Dmitrašinović, *Phys. Rev. Lett.* **110**, 114301 (2013).

- [26] M. Šuvakov, *Celest. Mech. Dyn. Astron.* **119**, 369 (2014).
- [27] When the orbit passes through the Euler point twice, such as in the yin-yang orbits, there are two different sets of initial conditions, and, consequently, two different rotation angles—we indicate exactly which one of the two solutions is taken. The total energy has been scaled to $E = -1/2$ for all solutions, so as to provide a meaningful comparison of peak amplitudes and luminosities.
- [28] A more detailed study of the waveforms emanating from the Lagrangian three-body orbit can be found in Ref. [12].
- [29] M. Šuvakov and V. Dmitrašinović, *Am. J. Phys.* **82**, 609 (2014).
- [30] The following argument was suggested by one of the referees: If a section of the trajectory of two bodies (within a three-body system) that approach a two-body collision can be approximated by an ellipse, then the luminosity P is proportional to $P \sim (1 - e^2)^{-7/2}$, see Eq. (5.4) in Ref. [9], where e is the eccentricity of the ellipse. Therefore, P grows without bounds as $e \rightarrow 1$, i.e., as the orbit approaches a two-body collision.
- [31] We do not show these waveforms here, except for the two in Fig. 1, for brevity's sake, and because many are fairly similar to the second waveform in Fig. 1—regular sequences of spikes.
- [32] Note that the figure-eight family members have, on the average, the lowest luminosity among the orbits considered here.
- [33] We plan to do such a study, which cannot be completed, however, without an extension of each orbit to a family of orbits with nonvanishing angular momenta. So far, only the BHH family has been extended in such a way, but even that one case is not complete [34].
- [34] M. R. Janković and M. Šuvakov (to be published).

Dynamics of weakly interacting bosons in optical lattices with fluxAna Hudomal,¹ Ivana Vasić,¹ Hrvoje Buljan,² Walter Hofstetter,³ and Antun Balaz̃¹¹*Scientific Computing Laboratory, Center for the Study of Complex Systems, Institute of Physics Belgrade, University of Belgrade, 11080 Belgrade, Serbia*²*Department of Physics, Faculty of Science, University of Zagreb, 10000 Zagreb, Croatia*³*Institut für Theoretische Physik, Johann Wolfgang Goethe-Universität, 60438 Frankfurt am Main, Germany*

(Received 19 September 2018; published 26 November 2018)

Realization of strong synthetic magnetic fields in driven optical lattices has enabled implementation of topological bands in cold-atom setups. A milestone has been reached by a recent measurement of a finite Chern number based on the dynamics of incoherent bosonic atoms. The measurements of the quantum Hall effect in semiconductors are related to the Chern-number measurement in a cold-atom setup; however, the design and complexity of the two types of measurements are quite different. Motivated by these recent developments, we investigate the dynamics of weakly interacting incoherent bosons in a two-dimensional driven optical lattice exposed to an external force, which provides a direct probe of the Chern number. We consider a realistic driving protocol in the regime of high driving frequency and focus on the role of weak repulsive interactions. We find that interactions lead to the redistribution of atoms over topological bands both through the conversion of interaction energy into kinetic energy during the expansion of the atomic cloud and due to an additional heating. Remarkably, we observe that the moderate atomic repulsion facilitates the measurement by flattening the distribution of atoms in the quasimomentum space. Our results also show that weak interactions can suppress the contribution of some higher-order nontopological terms in favor of the topological part of the effective model.

DOI: [10.1103/PhysRevA.98.053625](https://doi.org/10.1103/PhysRevA.98.053625)**I. INTRODUCTION**

Ultracold atoms in optical lattices provide a perfect platform for quantum simulations of various condensed-matter phenomena [1]. Yet, since charge-neutral atoms do not feel the Lorentz force, a big challenge in this field was realization of synthetic magnetic fields. After years of effort, artificial gauge potentials for neutral atoms were implemented by exploiting atomic coupling to a suitable configuration of external lasers [2,3]. These techniques were further extended to optical lattices, leading to the realization of strong, synthetic, magnetic fields. As a result, important condensed-matter models—the Harper-Hofstadter [4] and the Haldane model [5]—are nowadays available in cold-atom setups [6–9]. The key property of these models is their nontrivial topological content. In the seminal TKNN paper [10] it was shown that the quantization of the Hall conductivity observed in the integer Hall effect can be directly related to the topological index of the microscopic model—the Chern number.

Cold-atom realizations of topological models exploit periodic driving, either through laser-assisted tunneling [6,7] or by lattice shaking [8]. Using Floquet theory [11,12], a periodically driven system can be related to the time-independent effective Hamiltonian that corresponds to a relevant condensed-matter system. The mapping is known as Floquet engineering and its important features in the context of optical lattices are discussed in Refs. [13–20]. Because of important differences of cold-atom setups and their condensed-matter counterparts, new quench protocols for probing topological features were proposed [21–25]. Following up on these studies, the deflection of an atomic cloud as a response to external force was used to experimentally measure the Chern number in a nonelectronic system for the first time [26].

While Floquet engineering is a highly flexible and powerful technique, it poses several concerns. One of the main open questions is related to the interplay of driving and interactions which can heat up the system to a featureless, infinite-temperature regime according to general considerations [27,28]. In particular, it is shown that an initial Bose-Einstein condensate in a periodically driven optical lattice may become unstable due to two-body collisions [29] or through the mechanism of parametric resonance [28,30–36]. The preparation protocol, stability and a lifetime of strongly correlated phases, expected in the regime of strong interactions under driving is a highly debated topic at the moment [28,37,38].

In order to further explore the role of weak atomic interactions in probing topological features, here we consider the dynamics of weakly interacting incoherent bosons in a driven optical lattice exposed to an external force. The setup that we consider includes all basic ingredients for the Chern-number measurement [22,26]—the Chern number of the topological band can be extracted from the center-of-mass motion of atomic cloud in the direction transverse to the applied force. We assume an ideal initial state where the lowest topological band of the effective model is almost uniformly populated. The optimal loading sequence necessary to reach this state is considered in Refs. [39,40]. Following the recent experimental study [26], we assume that atoms are suddenly released from the trap and exposed to a uniform force. We perform numerical simulations for the full time-dependent Hamiltonian and take into account the effects of weak repulsive interactions between atoms within the mean-field approximation. We make a comparison between the dynamics governed by the effective and time-dependent Hamiltonian and delineate the

contribution of interactions to the center-of-mass response and to the overall cloud expansion dynamics. Our results show that interactions lead to the undesirable atomic transitions between topological bands [41], but we also find that a weak atomic repulsion can facilitate the Chern-number measurements in several ways.

The paper is organized as follows. In Sec. II we describe the model and introduce a method that we apply for the description of incoherent bosons. In Sec. III we address the dynamics of noninteracting incoherent bosons, and then in Sec. IV we address the regime of weak repulsive interactions. Finally, we summarize our results in Sec. V. Appendixes A to F provide further details.

II. MODEL AND METHOD

In this section, we first present the driven model introduced in Ref. [26], and then derive the corresponding effective model and discuss its basic characteristics. At the end, we explain our choice of the initial state and outline the method that we use to treat the dynamics of weakly interacting incoherent bosons.

A. Effective Floquet Hamiltonian

Interacting bosons in a two-dimensional optical lattice can be described by the Bose-Hubbard Hamiltonian

$$\begin{aligned} \hat{H}_{\text{BH}} = & -J_x \sum_{l,m} (\hat{a}_{l+1,m}^\dagger \hat{a}_{l,m} + \hat{a}_{l-1,m}^\dagger \hat{a}_{l,m}) \\ & -J_y \sum_{l,m} (\hat{a}_{l,m+1}^\dagger \hat{a}_{l,m} + \hat{a}_{l,m-1}^\dagger \hat{a}_{l,m}) \\ & + \frac{U}{2} \sum_{l,m} \hat{n}_{l,m} (\hat{n}_{l,m} - 1), \end{aligned} \quad (1)$$

where $\hat{a}_{l,m}^\dagger$ and $\hat{a}_{l,m}$ are creation and annihilation operators that create and annihilate a particle at the lattice site $(l, m) = la\mathbf{e}_x + ma\mathbf{e}_y$ (a is the lattice constant), $\hat{n}_{l,m} = \hat{a}_{l,m}^\dagger \hat{a}_{l,m}$ is the number operator, J_x and J_y are the hopping amplitudes along \mathbf{e}_x and \mathbf{e}_y , and U is the on-site interaction. In the derivation of the model (1) we use the single-band tight-binding approximation [1]. Although the experimental setup [26] is actually three dimensional, with an additional confinement in the third direction, our study is simplified to a two-dimensional lattice.

In order to engineer artificial gauge field in the experiment [26], hopping along \mathbf{e}_x was at first inhibited by an additional staggered potential

$$\hat{W} = \frac{\Delta}{2} \sum_{l,m} (-1)^l \hat{n}_{l,m}, \quad (2)$$

and then restored using resonant laser light. The experimental setup can be described by a time-dependent Hamiltonian

$$\tilde{H}(t) = \hat{H}_{\text{BH}} + \hat{V}(t) + \hat{W}, \quad (3)$$

where $\hat{V}(t)$ is a time-dependent modulation

$$\begin{aligned} \hat{V}(t) = & \kappa \sum_{l,m} \hat{n}_{l,m} \left[\cos\left(\frac{l\pi}{2} - \frac{\pi}{4}\right) \cos\left(\omega t - \frac{m\pi}{2} + \phi_0\right) \right. \\ & \left. + \cos\left(\frac{l\pi}{2} + \frac{\pi}{4}\right) \cos\left(-\omega t - \frac{m\pi}{2} + \frac{\pi}{2} + \phi_0\right) \right], \end{aligned} \quad (4)$$

κ is the driving amplitude, and $\omega = \Delta$ is the resonant driving frequency. We set the relative phase ϕ_0 between the optical-lattice potential and the running waves used for laser-assisted tunneling to $\phi_0 = \pi/4$.

Using Floquet theory, the time-evolution operator corresponding to the Hamiltonian (3) can be represented as

$$\hat{U}(t, t_0) = e^{-i\hat{W}t} e^{-i\hat{K}(t)} e^{-i(t-t_0)\hat{H}_{\text{eff}}} e^{i\hat{K}(t_0)} e^{i\hat{W}t_0}, \quad (5)$$

where \hat{H}_{eff} is the full time-independent effective Hamiltonian that describes slow motion and $\hat{K}(t)$ is the time-periodic kick operator that describes micromotion [13,14].

For the moment, in this subsection we first consider the noninteracting model $U = 0$. We also assume that the driving frequency ω is the highest energy scale, but that it is still low enough that the lowest-band approximation used in deriving Eq. (1) is still valid. In the leading order of the high-frequency expansion, the effective Hamiltonian \hat{H}_{eff} is given by

$$\begin{aligned} \hat{H}_{\text{eff},0} = & J'_x \sum_{l,m} [e^{i((m-l-1)\pi/2 - \pi/4)} \hat{a}_{l+1,m}^\dagger \hat{a}_{l,m} + \text{H.c.}] \\ & - J'_y \sum_{l,m} (\hat{a}_{l,m+1}^\dagger \hat{a}_{l,m} + \hat{a}_{l,m-1}^\dagger \hat{a}_{l,m}), \end{aligned} \quad (6)$$

where the renormalized hopping amplitudes are $J'_x = \frac{J_x \kappa}{\sqrt{2\omega}} = J_y$ and $J'_y = J_y (1 - \frac{\kappa^2}{2\omega^2})$. A schematic representation of this model is presented in Fig. 1(a). The unit cell is shaded and the full lattice is spanned by the vectors $\mathbf{R}_1 = (4, 0)$ and $\mathbf{R}_2 = (1, 1)$. Particle hopping around a plaquette in the counterclockwise direction acquires a complex phase $-\frac{\pi}{2}$ and the model is equivalent to the Harper-Hofstadter Hamiltonian [4] for the case $\alpha = 1/4$ [4]. The explicit form of the kick operator $\hat{K}(t)$ from Eq. (3) is given in Appendix A.

Following Refs. [13,14], we find that additional corrections of the order J'_x/ω contribute to the system's dynamics and we introduce another approximation for the effective Hamiltonian

$$\begin{aligned} \hat{H}_{\text{eff},1} = & \hat{H}_{\text{eff},0} + \frac{J_x^2}{\omega} \sum_{l,m} (-1)^l (2\hat{a}_{l,m}^\dagger \hat{a}_{l,m} \\ & + \hat{a}_{l+2,m}^\dagger \hat{a}_{l,m} + \hat{a}_{l-2,m}^\dagger \hat{a}_{l,m}). \end{aligned} \quad (7)$$

The derivation of Hamiltonian (7) is given in Appendix A and its schematic representation is given in Fig. 1(b). The J_x^2/ω correction introduces next-nearest-neighbor hopping along x direction with opposite signs for lattice sites with either even or odd x -coordinate l . This term does not change the total complex phase per plaquette, but the unit cell is now doubled and thus the first Brillouin zone is halved. A similar term was engineered on purpose in order to implement the Haldane model [8].

In the next subsection we investigate properties of energy bands of both effective Hamiltonians, $\hat{H}_{\text{eff},0}$ and $\hat{H}_{\text{eff},1}$. We use the units where $\hbar = 1$ and $a = 1$. Unless otherwise stated, we set the parameters to the following values: lattice size 100×100 sites, hopping amplitudes $J'_x = J_y = 1 \equiv J$, and the driving amplitude $\kappa = 0.58\omega$. This value of the driving amplitude was chosen to be the same as in the experiment [26]. In order to set the renormalized hopping amplitude along \mathbf{e}_x to $J'_x = 1$, the initial hopping amplitude has to be

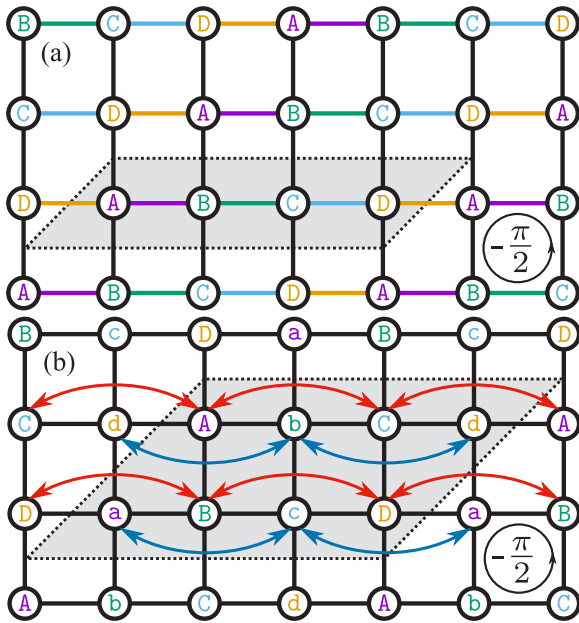


FIG. 1. Schematic representation of the model. The unit cells are shaded. (a) Effective Hamiltonian without correction, $\hat{H}_{\text{eff},0}$ (6). Vertical links correspond to real hopping amplitudes (along \mathbf{e}_y direction), while the horizontal links to the right of lattice sites labeled A, B, C, and D correspond to complex hopping amplitudes with phases $\frac{3\pi}{4}$, $\frac{\pi}{4}$, $-\frac{\pi}{4}$, and $-\frac{3\pi}{4}$, respectively (when hopping from left to right). (b) Effective Hamiltonian with correction, $\hat{H}_{\text{eff},1}$ (7). Red lines represent positive next-nearest-neighbor hopping amplitudes (connecting uppercase letters), while the blue lines represent negative next-nearest-neighbor hopping amplitudes (connecting lowercase letters). Nearest-neighbor hopping amplitudes are the same as in (a).

$J_x = \sqrt{2}\omega/\kappa = 2.44$, and the correction term is therefore proportional to $J_x^2/\omega = 5.95/\omega$, so it cannot be safely neglected unless the driving frequency is very high.

B. Band structure

Momentum-space representations of the effective Hamiltonians $\hat{H}_{\text{eff},0}$ and $\hat{H}_{\text{eff},1}$, denoted by $\hat{\mathcal{H}}_{\text{eff},0}(\mathbf{k})$ and $\hat{\mathcal{H}}_{\text{eff},1}(\mathbf{k})$, respectively, are derived in Appendix B. Band structures for the effective Hamiltonian $\hat{\mathcal{H}}_{\text{eff},0}$ without the J_x^2/ω correction, Eq. (B1), as well as for the effective Hamiltonian $\hat{\mathcal{H}}_{\text{eff},1}$

including the correction term, Eq. (B2), are shown in Fig. 2 for the two values of driving frequencies $\omega = 20$ and $\omega = 10$.

The Hamiltonian $\hat{H}_{\text{eff},0}$ is the Harper-Hofstadter Hamiltonian for the flux $\alpha = 1/4$. It has four energy bands, where the middle two bands touch at $E = 0$ and can therefore be regarded as a single band; see Fig. 2(a). The topological content of these bands is characterized by the topological index called the Chern number. The Chern number is the integral of the Berry curvature [42] over the first Brillouin zone divided by 2π ,

$$c_n = \frac{1}{2\pi} \int_{\text{FBZ}} \boldsymbol{\Omega}_n(\mathbf{k}) \cdot d\mathbf{S}, \quad (8)$$

where n denotes the band number and the Berry curvature is $\boldsymbol{\Omega}_n(\mathbf{k}) = i\nabla_{\mathbf{k}} \times \langle u_n(\mathbf{k}) | \nabla_{\mathbf{k}} | u_n(\mathbf{k}) \rangle$, expressed in terms of eigenstates of the effective Hamiltonian $|u_n(\mathbf{k})\rangle$. The Chern numbers of the three well-separated bands are $c_1 = 1$, $c_2 = -2$, and $c_3 = 1$.

Because the correction from Eq. (7) includes next-nearest-neighbor hopping terms, the elementary cell in real space is doubled [see Fig. 1(b)] and, as a consequence, the first Brillouin zone for the Hamiltonian $\hat{\mathcal{H}}_{\text{eff},1}$ is reduced by a factor of 2 compared to $\hat{\mathcal{H}}_{\text{eff},0}$. There are now eight lattice sites in the unit cell and eight energy bands, but the number of gaps depends on the driving frequency. The new bands touch in pairs, in such a way that there are always maximally three well-separated bands. When the driving frequency is high enough, the correction is small and the gaps between the three bands remain open; see Fig. 2(b). The original band structure of $\hat{\mathcal{H}}_{\text{eff},0}$ is recovered in the limit $\omega \rightarrow \infty$. The Berry curvature and the Chern number can be calculated using the efficient method presented in Ref. [43]. Our calculations confirm that the Chern numbers of $\hat{\mathcal{H}}_{\text{eff},1}$ are equal to those of $\hat{\mathcal{H}}_{\text{eff},0}$ ($c_1 = 1$, $c_2 = -2$, and $c_3 = 1$), as long as the gaps between the energy bands are open. The gaps close when the driving frequency is too low, see Fig. 2(c), and the Chern numbers of the subbands can no longer be properly defined.

C. Dynamics of incoherent bosons

We need to take into account a contribution of weak, repulsive interactions. Full numerical simulations of an interacting many-body problem are computationally demanding, so we need a reasonable, numerically tractable approximation. To this end we will use the classical field method [44], which

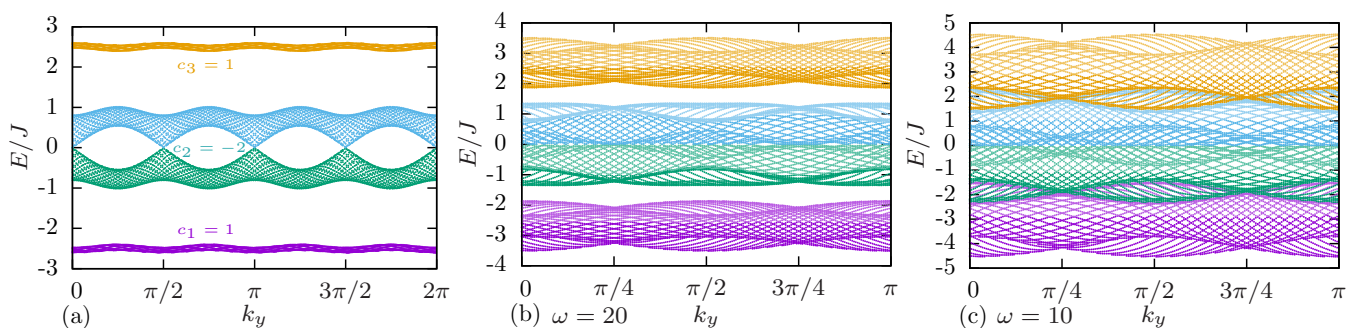


FIG. 2. Energy bands of the effective Hamiltonians. (a) $\hat{\mathcal{H}}_{\text{eff},0}(\mathbf{k})$ Eq. (B1), which is without the J_x^2/ω correction term. (b) $\hat{\mathcal{H}}_{\text{eff},1}(\mathbf{k})$ Eq. (B2), which includes the correction term. Driving frequency $\omega = 20$; gaps are open. (c) Same as (b), but with $\omega = 10$. Gaps are closed.

belongs to a broader class of truncated Wigner approaches [45]. This method is similar to the approach used to treat incoherent light in instantaneous media [46,47], known in optics as the modal theory.

The underlying idea of the method is to represent the initial state as an incoherent mixture of coherent states $|\psi\rangle$, $\hat{a}_{l,m}|\psi\rangle = \psi_{l,m}|\psi\rangle$ [44]. This is explained in more detail in Appendix C. In our study, we sample initial configurations of these coherent states with

$$|\psi(t=0)\rangle = \sum_{k=1}^{N_m} e^{i\phi_k} |k\rangle, \quad (9)$$

where $\phi_k \in [0, 2\pi)$ are random phases and the states $|k\rangle$ correspond closely to the lowest-band eigenstates of \hat{H}_{eff} . Each of N_{samples} initial states is time evolved and physical variables can be extracted by averaging over an ensemble of different initial conditions.

The time evolution of each of these coherent states is governed by

$$i \frac{d\psi_{l,m}(t)}{dt} = \sum_{ij} H_{lm,ij}(t) \psi_{i,j}(t) - F m \psi_{l,m}(t) + U |\psi_{l,m}(t)|^2 \psi_{l,m}(t), \quad (10)$$

where $H_{lm,ij}(t) = \langle l, m | \hat{H}(t) | i, j \rangle$ are matrix elements of $\hat{H}(t)$ from Eq. (3), F is the external force, and interactions U contribute with the last, nonlinear term. Formally, Eq. (10) takes the form of the Gross-Pitaevskii equation [48–50]. The performances and limitations of the method are discussed and reviewed in Ref. [51].

For comparison, we also consider the related time evolution governed by the effective Hamiltonian

$$i \frac{d\psi_{l,m}(t)}{dt} = \sum_{ij} h_{lm,ij}^{\text{eff}} \psi_{i,j}(t) - F m \psi_{l,m}(t) + U |\psi_{l,m}(t)|^2 \psi_{l,m}(t), \quad (11)$$

where $h_{lm,ij}^{\text{eff}} = \langle l, m | \hat{h}^{\text{eff}} | i, j \rangle$, with \hat{h}^{eff} being either $\hat{H}_{\text{eff},0}$ from Eq. (6), or $\hat{H}_{\text{eff},1}$ from Eq. (7). Equation (11) should be considered only as a tentative description of the system: the mapping between $\hat{H}(t)$ and \hat{H}_{eff} is strictly valid only in the noninteracting regime and the interaction term may introduce complex, nonlocal, higher-order corrections [27]. However, we expect their contribution to be small in the limit $U \rightarrow 0$, and for time scales which are not too long [52–55].

In the following we use $N_m = 300$ modes and accommodate $N_p = 300$ particles per mode, so in total in the simulations we have $N = N_m N_p = 90\,000$ bosons. Typical densities in real space are up to 100 particles per site and we choose the values of U in the range $U \in [0, 0.05]$. Other parameters: $J'_x = J_y = 1$, $\kappa/\omega = 0.58$, $\omega = 10, 20$, and $F = 0.25J/a$. The correction terms are non-negligible in this frequency range. In practice, we first numerically diagonalize the Hamiltonian (C2) from Appendix C and set our parameters in such a way that the lowest N_m modes have high overlap with the lowest band of the effective model. In the next step, we sample initial configurations (9). For each of $N_{\text{samples}} = 1000$ sets of initial conditions we then time evolve Eq. (10) and extract quantities of interest by averaging over resulting

TABLE I. Four different cases: the same effective Hamiltonian is always used for the initial state and band definitions, either with or without the correction. The evolution is governed either by the time-dependent Hamiltonian or by the same effective Hamiltonian as the one that was used for the initial state and calculation of band populations.

Case	Initial state	Band populations	Evolution
1	$\hat{H}_{\text{eff},1}$	$\hat{H}_{\text{eff},1}$	$\hat{H}_{\text{eff},1}$
2	$\hat{H}_{\text{eff},1}$	$\hat{H}_{\text{eff},1}$	$\hat{H}(t)$
3	$\hat{H}_{\text{eff},0}$	$\hat{H}_{\text{eff},0}$	$\hat{H}_{\text{eff},0}$
4	$\hat{H}_{\text{eff},0}$	$\hat{H}_{\text{eff},0}$	$\hat{H}(t)$

trajectories. This value of N_{samples} is chosen to be high enough, so that the fluctuations are weak. We present and discuss results of our numerical simulations in the following sections.

III. NONINTERACTING CASE

We start by addressing the dynamics of noninteracting bosons. In this case we set $U = 0$ in Eq. (10) and numerically solve the single-particle Schrödinger equation without further approximations. Our aim is to numerically validate and compare the two approximations, Eqs. (6) and (7), for the effective Hamiltonian. To this purpose, we juxtapose results of the two approximative schemes with the numerically exact results obtained by considering the full time evolution governed by $\hat{H}(t)$. For clarity, the four different time evolutions that we consider in this section are summarized in Table I. We calculate the center-of-mass position $x(t)$ and plot the results in Fig. 3. In this way we also find the regime of microscopic

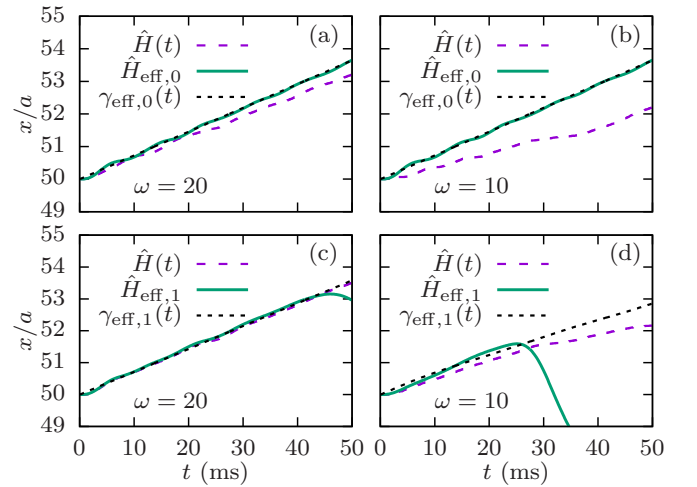


FIG. 3. Anomalous drift $x(t)$. Dashed purple lines: numerical simulations using the time-dependent Hamiltonian $\hat{H}(t)$ (cases 2 and 4 from Table I). Solid green lines: effective Hamiltonians $\hat{H}_{\text{eff},1}$ (c) and (d) and $\hat{H}_{\text{eff},0}$ (a) and (b) (cases 1 and 3). Dotted black lines: theoretical prediction (14) from $\gamma_{\text{eff},1}(t)$ or $\gamma_{\text{eff},0}(t)$. (a) Initial states and band populations obtained using the effective Hamiltonian $\hat{H}_{\text{eff},0}$ without the correction (cases 3 and 4). Driving frequency $\omega = 20$. (b) $\omega = 10$. (c) Hamiltonian $\hat{H}_{\text{eff},1}$ with the J_x^2/ω correction (cases 1 and 2). Driving frequency $\omega = 20$. (d) $\omega = 10$.

parameters where the Chern-number measurement can be optimally performed.

First, we consider the basic Harper-Hofstadter Hamiltonian (6) and select the occupied modes $|k\rangle$ of the initial state (C1) as eigenstates of the model from Eq. (9) for $\hat{h}_{\text{eff}} = \hat{H}_{\text{eff},0}$. As explained in the previous section, at the initial moment $t_0 = 0$, the confinement is turned off and the force $\mathbf{F} = -F\mathbf{e}_y$ is turned on. As a consequence of the applied external force and the nonzero Chern number of the lowest band of the model (6), the particles exhibit an anomalous velocity in the direction perpendicular to the force [56]. In the ideal case, when the lowest band is fully populated, the theoretical prediction for the center-of-mass position in the \mathbf{e}_x direction is [26]

$$x(t) = x(t_0) + c_1 \frac{2Fa^2}{\pi\hbar} t, \quad (12)$$

where $c_1 = 1$ is the Chern number (8) of the lowest band. However, even in the ideal case, due to the sudden quench of the linear potential, a fraction of particles is transferred to the higher bands. To take this effect into account, the authors of Ref. [26] introduced a filling factor $\gamma(t)$

$$\gamma(t) = \eta_1(t) - \eta_2(t) + \eta_3(t), \quad (13)$$

where $\eta_i(t)$ are populations of different bands of Hamiltonian (6) from Eq. (C4) in Appendix C and the plus and minus signs in Eq. (13) are defined according to the Chern numbers $c_1 = 1$, $c_2 = -2$, and $c_3 = 1$. The final theoretical prediction is then [26]

$$x(t) = x(t_0) + c_1 \frac{2Fa^2}{\pi\hbar} \int_0^t \gamma(t') dt'. \quad (14)$$

In Fig. 3(a) we consider the anomalous drift for a high value of the driving frequency $\omega = 20$, where we expect the expansion in $1/\omega$ to be reliable. We find an excellent agreement between the prediction (14) (dotted black line) and numerical calculation based on $\hat{H}_{\text{eff},0}$ (solid green line). However, some deviations between the full numerical results (dashed purple line) and the results of the approximation scheme (solid green line) are clearly visible. These deviations are even more pronounced for $\omega = 10$, Fig. 3(b).

Now we turn to the effective model (7). In this case we select the modes of the initial state as eigenstates of Eq. (9) for $\hat{h}_{\text{eff}} = \hat{H}_{\text{eff},1}$. Moreover, we also consider band populations (C4) of the same model. In the case when $\omega = 20$, Fig. 3(c), the anomalous drift obtained using the effective Hamiltonian (7) (solid green line) closely follows the theoretical prediction (14). Moreover, from the same figure we can see that the effective Hamiltonian $\hat{H}_{\text{eff},1}$ reproduces the behavior of the time-dependent Hamiltonian very well. All three curves almost overlap for intermediate times (5–40 ms); see Fig. 3(c). We attribute the long-time (>45 ms) deviations to the finite-size effects introduced by the next-nearest-neighbor hopping terms, which cause the atomic cloud to reach the edge of the lattice faster. This effect is explained in more detail in Sec. IV B.

For a lower driving frequency $\omega = 10$, the effective and the time-dependent Hamiltonians do not agree so well anymore; see Fig. 3(d). The finite-size effects can be observed even earlier in this case (around 25 ms). This happens because the next-nearest-hopping terms are inversely proportional to the

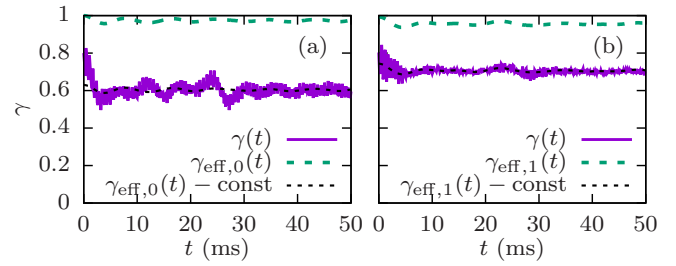


FIG. 4. Time evolution of the filling factor $\gamma(t)$ for driving frequency $\omega = 20$. Solid purple lines: evolution governed by the time-dependent Hamiltonian $\hat{H}(t)$ (cases 2 and 4 from Table I). Dashed green lines: evolution governed by the effective Hamiltonian $\hat{H}_{\text{eff},1}$ or $\hat{H}_{\text{eff},0}$ (cases 1 and 3). Dotted black lines: green lines shifted in order to compare them with purple lines. Shift is chosen so that the two lines approximately overlap. (a) Initial states and band populations obtained using the effective Hamiltonian $\hat{H}_{\text{eff},0}$, which is without the J_x^2/ω correction term (cases 3 and 4). (b) Hamiltonian $\hat{H}_{\text{eff},1}$ which is with the correction term (cases 1 and 2).

driving frequency. It is interesting to note that the prediction (14) is close to numerical data for short times even in this case when the gaps of the effective model are closed, see Fig. 2(c), and the Chern number of the lowest band is not well defined. In fact, it is surprising that the anomalous drift even exists in this case, as all subbands are now merged into a single band. We attribute this effect to our choice of the initial state. When the gaps are closed, it is hard to set the parameters in such a way that the lowest band is completely filled. The top of this band usually remains empty and the particles thus do not “see” that the gap is closed.

Time evolution of the filling factor $\gamma(t)$ is plotted in Fig. 4 for four different cases from Table I—evolution using the effective Hamiltonian without correction $\hat{H}_{\text{eff},0}$ [$\gamma_{\text{eff},0}(t)$, case 3, dashed green line in Fig. 4(a)], the effective Hamiltonian with correction $\hat{H}_{\text{eff},1}$ [$\gamma_{\text{eff},1}(t)$, case 1, dashed green line in Fig. 4(b)], or the time-dependent Hamiltonian $\hat{H}(t)$ [$\gamma(t)$, cases 2 and 4, solid purple lines]. At the initial moment $\gamma(t_0 = 0) < 1$, because the initial state was multiplied by the operator $e^{-i\hat{k}(0)}$. This introduces a shift between $\gamma(t)$ and $\gamma_{\text{eff},1}(t)$. Apart from the shift, these two curves behave similarly, unlike the $\gamma_{\text{eff},0}(t)$ curve that exhibits completely different behavior. Because of this, we use only $\gamma_{\text{eff},1}(t)$ to estimate the value of the prediction (14).

We find that the values of $\gamma_{\text{eff},1}(t)$ for $\omega = 20$ are high: ≥ 0.95 ; see Fig. 4. For this reason, up to 50 ms the center-of-mass position $x(t)$ exhibits roughly linear behavior with some additional oscillations. Interestingly, the anomalous drift $x(t)$ exhibits quadratic behavior on short time scales in all cases from Fig. 3. In Appendix D, we explain this feature using the time-dependent perturbation theory and Fermi’s golden rule.

IV. INTERACTING CASE

We now investigate the effects of weak repulsive interactions. We work in the high-frequency regime and set $\omega = 20$. As shown in Sec. II B, for $U = 0$ the effective Hamiltonian with correction, $\hat{H}_{\text{eff},1}$, is in this case equivalent to the Harper-Hofstadter Hamiltonian with flux $\alpha = 1/4$. Moreover, the

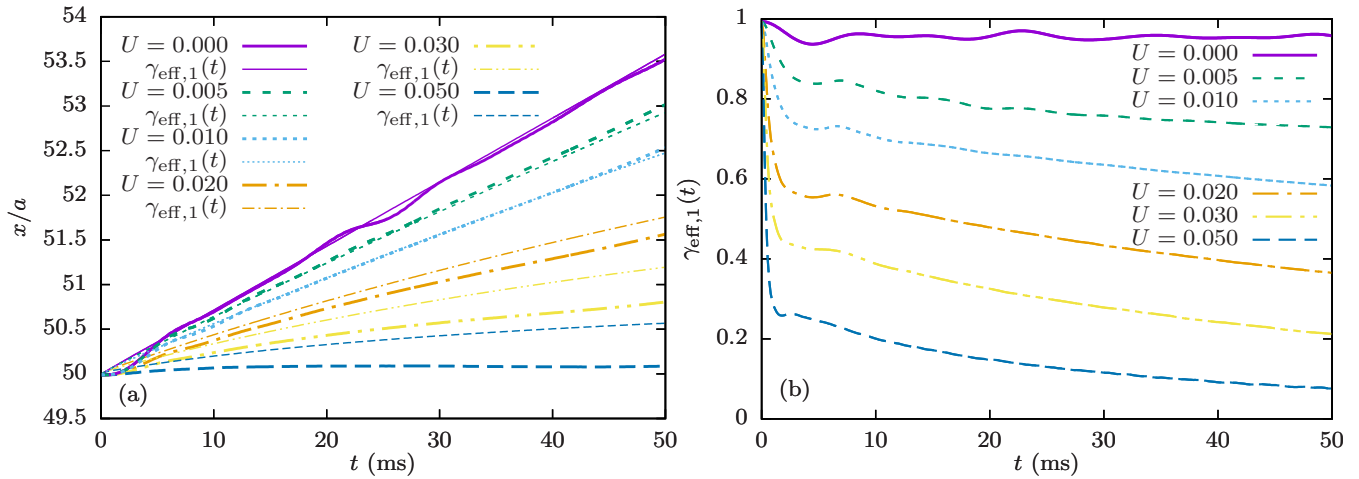


FIG. 5. Effects of interactions. (a) Anomalous drift $x(t)$ for several different values of the interaction coefficient U . U is given in units where $J = 1$. Thick lines: numerical simulations using the time-dependent Hamiltonian $\hat{H}(t)$. Thin lines: theoretical prediction (14) from $\gamma_{\text{eff},1}(t)$. (b) Corresponding $\gamma_{\text{eff},1}(t) = \eta_1(t) - \eta_2(t) + \eta_3(t)$, obtained from simulations using the effective Hamiltonian $\hat{H}_{\text{eff},1}$.

same approximative form of the full effective model accurately reproduces the behavior of the time-dependent Hamiltonian up to 50 ms and thus provides a good starting point for the study of weakly interacting particles. We first consider the anomalous drift of the center of mass of the atomic cloud and then we inspect the expansion dynamics more closely in terms of atomic density distributions in real and momentum space.

A. Anomalous drift and dynamics of band populations

To simulate the dynamics of many incoherent bosons, we use the classical field method presented in Sec. II C and propagate Eq. (10) in time. We assume that at $t_0 = 0$ atoms are uniformly distributed over the lowest band of $\hat{H}_{\text{eff},1}$. For this reason, the initial state is the same as the one that we use in the noninteracting regime. In this way, the dynamics is initiated by an effective triple quench: at $t_0 = 0$ the confining potential is turned off, atoms are exposed to the force $\mathbf{F} = -F\mathbf{e}_y$, and also the interactions between particles are introduced. The total number of particles is set to $N = 90\,000$, which amounts to approximately 100 particles per lattice site in the central region of the atomic cloud. We consider only weak repulsion $U \leq 0.05$.

The anomalous drift $x(t)$ obtained using the full time-dependent Hamiltonian is shown in Fig. 5(a) for several different values of the interaction strength U . In comparison to the noninteracting regime, we find that the weak repulsive interactions inhibit the response of the center of mass to the external force. In particular, at $t = 50$ ms the drift is reduced by about 15% for $U = 0.005$ and it is further lowered by an increase in U . Finally, at $U = 0.05$, the anomalous drift is barely discernible. Interestingly, for weak $U \in (0.001, 0.01)$ we find that the drift $x(t)$ in the range of $t \in (10, 50)$ ms looks “more linear” as a function of time in comparison to the noninteracting result.

We now analyze the anomalous drift in terms of the filling factor $\gamma(t)$ and compare the results of Eq. (10) with the description based on Eq. (11). By solving Eq. (11) we obtain the filling factor $\gamma_{\text{eff},1}(t)$ following Eq. (C4) and present

our results in Fig. 5(b). Whenever the results of Eq. (10) reasonably agree with the results obtained from Eq. (11), we are close to a steady-state regime with only small fluctuations in the total energy, as Eq. (11) preserves the total energy of the system. In this regime, during the expansion dynamics the interaction energy is converted into the kinetic energy and atoms are transferred to higher bands of the effective model. Consequently, the filling factor $\gamma_{\text{eff},1}(t)$ is reduced. Typically, we find three different stages in the decrease of $\gamma_{\text{eff},1}(t)$.

In an early stage, $t \leq t_1 = 5$ ms, a fast redistribution of particles over the bands of the effective model sets in due to the sudden quench of U . The factor $\gamma_{\text{eff},1}(t)$ decays quadratically as a function of time down to $\gamma_{\text{eff},1}(t_1) \approx 0.75$ for $U = 0.01$, and $\gamma_{\text{eff},1}(t_1) \approx 0.25$ for $U = 0.05$. In this process the interaction energy of the system is quickly lowered as described in Appendix E. At later times $t > 5$ ms, we observe a linear decay of the filling factor $\gamma_{\text{eff},1}(t)$ as a function of time, that finally turns into an exponential decay at even later times ($t > 10$ ms). Similar regimes are observed in other dynamical systems. For example, a decay rate of an initial state suddenly coupled to a bath of additional degrees of freedom exhibits these three stages [57]. The initial quadratic decay is often denoted as “the Zeno regime.” For longer propagation times, Fermi’s golden rule predicts the linear decay. At even longer time scales, when the repopulation of the initial state is taken into account, the time-dependent perturbation theory yields the exponential regime, known under the name of the Wigner-Weisskopf theory [57].

We now investigate this last regime in more detail. For the population of the lowest band $\eta_1(t)$, an exponential decay function $f(t) = a + b e^{-ct}$ provides high quality fits for $t \in (10, 50)$ ms; see Fig. 6(a) for an example. Similarly, the populations of two higher bands can also be fitted to exponential functions. The obtained exponential decay coefficients c for the lowest band population are plotted as a function of the interaction strength U in Fig. 6(b). The resulting dependence is approximately quadratic: $c(U) = \alpha_0 + \alpha_1 U + \alpha_2 U^2$. For small values of U , the exponents $c(U)$ obtained for the dynamics governed by $\hat{H}(t)$ and $\hat{H}_{\text{eff},1}$ agree very well and

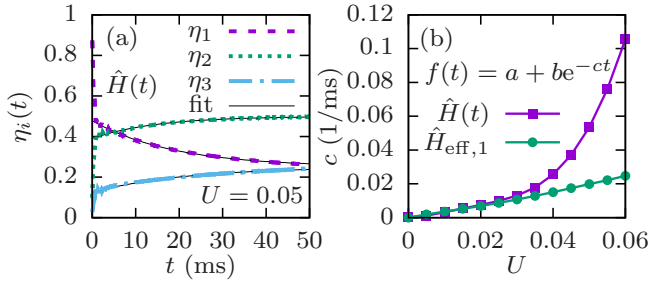


FIG. 6. (a) Evolution of the band populations $\eta_i(t)$. Dashed lines: numerical results obtained using the time-dependent Hamiltonian $\hat{H}(t)$. Solid black lines: exponential fit using $f(t) = a + b e^{-ct}$. The coefficient a was fixed to $a_1 = 0.25$, $a_2 = 0.50$, and $a_3 = 0.25$ for the first, second, and third band, respectively. (b) Dependence of the exponential decay coefficients for the lowest band population $\eta_1(t)$ on the interaction strength. U is given in units where $J = 1$.

exhibit linear behavior. At stronger interaction strengths $U \geq 0.03$, the approximation of Eq. (11) becomes less accurate as it omits the quadratic contribution in $c(U)$ found in the full time evolution. In addition, the values of the exponents c are affected by the force strength F and driving frequency ω .

As we now understand some basic features of $\gamma_{\text{eff},1}(t)$, we make an explicit comparison between the numerical results for the anomalous drift and the expectation (14). The dashed lines in Fig. 5(a) correspond to the theoretical prediction (14) calculated from $\gamma_{\text{eff},1}(t)$. For the intermediate interaction strengths $U \leq 0.01$, we find a very good agreement between the two. From this we conclude that the interaction-induced transitions of atoms to higher bands are the main cause of the reduced anomalous drift $x(t)$ as a function of U . When the interactions become strong enough ($U \sim 0.02$), the numerical results start to deviate from the theoretical prediction (14) with $\gamma_{\text{eff},1}(t)$. In this regime, Eq. (11) does not provide a reliable description of the dynamics, as higher-order corrections need to be taken into account.

B. Real and momentum-space dynamics

So far we have considered the averaged response of the whole atomic cloud. We now inspect the expansion dynamics in a spatially resolved manner. The real-space probability densities at the initial moment and after 50 ms (75 driving periods) are shown in Figs. 7 and 8, and the corresponding momentum-space probability densities in Appendix F.

At the initial moment, the atomic cloud is localized in the center of the lattice. By setting $r_0 = 20$ in the confining potential of Eq. (C2) and populating the lowest-lying states, we fix the cloud radius to $r = 20$, Fig. 7(a). The cloud density is of the order of 100 atoms per lattice site and a weak density modulation is visible along x direction. After the confining potential is turned off, and the external force in the $-\mathbf{e}_y$ direction is turned on, the cloud starts to expand and move in the $+\mathbf{e}_x$ direction. As shown in the previous subsection, the band populations and therefore the anomalous drift are significantly altered by the interaction strength, and this is also the case with the expansion dynamics; see Figs. 7 and 8.

In the noninteracting case, Fig. 7(b), the atomic cloud nearly separates into two parts moving in opposite directions

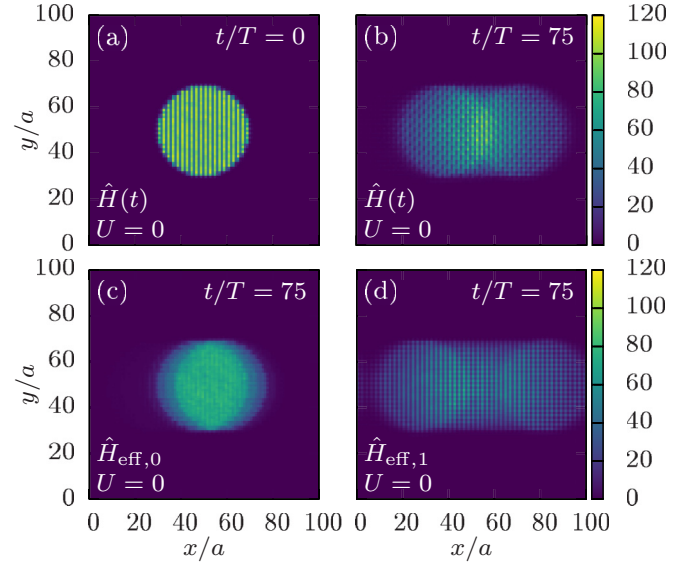


FIG. 7. Real-space density distribution, noninteracting case $U = 0$. (a) Initial state. (b) After 50 ms (75 driving periods), evolution using the time-dependent Hamiltonian $\hat{H}(t)$. (c) Evolution using effective Hamiltonian without correction $\hat{H}_{\text{eff},0}$. (d) Evolution using effective Hamiltonian with correction $\hat{H}_{\text{eff},1}$.

along x axes (while the center of mass still moves in the $+\mathbf{e}_x$ direction). By comparing Fig. 7(c) and Fig. 7(d), we conclude that this effect stems from the next-nearest-neighbor hopping along x present in the effective Hamiltonian (7), as it does not happen in the effective model without the correction term (6). This type of separation was already observed in Ref. [22], where the next-nearest-neighbor hopping terms were also present. When the interactions between particles are included,

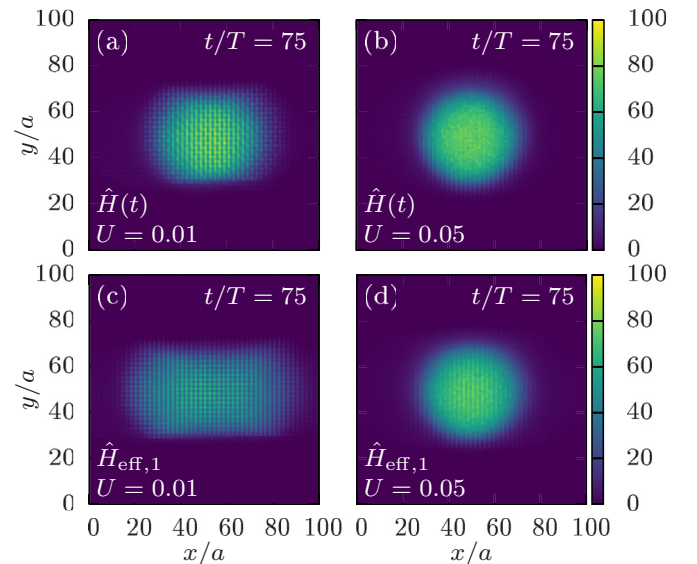


FIG. 8. Real-space density distribution after 50 ms (75 driving periods), interacting case. U is given in units where $J = 1$. (a) Evolution using the time-dependent Hamiltonian $\hat{H}(t)$, $U = 0.01$. (b) Same with $U = 0.05$. (c) Evolution using the effective Hamiltonian $\hat{H}_{\text{eff},1}$, $U = 0.01$. (d) Same with $U = 0.05$.

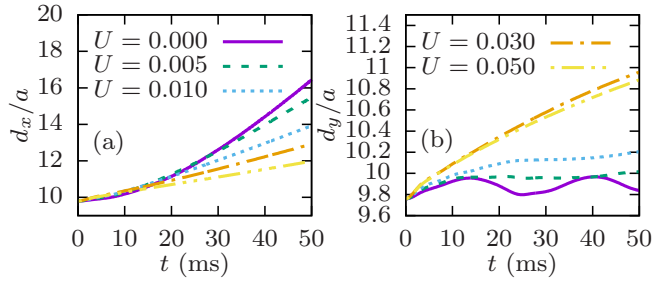


FIG. 9. Atomic cloud width for different interaction strengths, evolution using the time-dependent Hamiltonian $\hat{H}(t)$. U is given in units where $J = 1$. (a) $d_x = \sqrt{\langle x^2 \rangle - \langle x \rangle^2}$. (b) $d_y = \sqrt{\langle y^2 \rangle - \langle y \rangle^2}$.

this separation is not so prominent [Fig. 8(a), $U = 0.01$], and it almost completely disappears when the interactions are strong enough [Fig. 8(b), $U = 0.05$]. This is also the case when the evolution is governed by the effective Hamiltonian $\hat{H}_{\text{eff},1}$; see Figs. 8(c) and 8(d). Atomic cloud widths $d_x = \sqrt{\langle x^2 \rangle - \langle x \rangle^2}$ during the expansion are plotted in Fig. 9. We observe a slow expansion of the cloud in y direction, Fig. 9(b), and much faster expansion along x direction, Fig. 9(a), which comes about as a consequence of the cloud separation. On top of this, we observe that the interactions enhance expansion along y . Surprisingly, the opposite is true for the dynamics along x . This counterintuitive effect is often labeled as self-trapping and its basic realization is known for the double-well potential [58,59]. In brief, strong repulsive interactions can preserve the density imbalance between the two wells, as the system cannot release an excess of the interaction energy. In our case, the situation is slightly more involved as the cloud splitting is inherent (induced by the corrections of the ideal effective Hamiltonian). Apart from this, due to the driving the total energy is not conserved. However, our numerical results indicate that the interaction energy is slowly released in the second expansion stage, Fig. 14. Effectively, in this way the interactions cancel out the contribution of the next-nearest-neighbor hopping and favor the measurement of the properties of the model (6). In Fig. 10(a) we show that deviations between different approximations based on $\hat{H}(t)$,

$\hat{H}_{\text{eff},1}$, and $\hat{H}_{\text{eff},0}$ in the anomalous drift $x(t)$ nearly vanish at $U = 0.01$.

Another desirable effect might be that the interactions make the momentum-space probability density more homogeneous, see Appendix F, so that the real-space probability density becomes more localized. We can quantify momentum-space homogeneity using the inverse participation ratio $R(t) = \frac{1}{\sum_i P_i^2(t)}$, where $P_i(t) = |\psi_i(t)|^2$ is the probability that the state ψ_i is occupied at time t . Minimal value of the inverse participation ratio (IPR) is 1 and it corresponds to a completely localized state, while the maximal value is equal to the total number of states (in our case 10 000) and corresponds to the completely delocalized state, where the particles have the same probability of being at any quasi-momentum \mathbf{k} . As stated before, the first Brillouin zone of the lowest band has to be as homogeneously populated as possible in order to properly measure the lowest band Chern number. From Fig. 10(b), we see that IPR increases in time when the interaction coefficient U is large enough, so we can conclude that the interactions are actually beneficial for measuring the Chern number, as they can “smooth out” the momentum-space probability density. In Fig. 10(c) we give estimates for the Chern number that can be extracted from our numerical data for different values of U . We find the best estimate $c_1 \sim 0.99$ for the intermediate interaction strength $U \sim 0.01$.

C. Staggered detuning

Here we briefly consider the effects of staggered detuning that was introduced in the experimental study [26] during the loading and band mapping sequences. This detuning can be described by an additional term

$$\frac{\delta}{2} \sum_{l,m} [(-1)^l + (-1)^m] \hat{n}_{l,m} \quad (15)$$

in the Hamiltonians $\hat{H}(t)$ and $\hat{H}_{\text{eff},1}$. We will ignore the higher-order [at most $O(\frac{1}{\omega^2})$] corrections that this term introduces to the effective Hamiltonian. Staggered detuning does not break the symmetry of the effective Hamiltonian $\hat{H}_{\text{eff},1}$, but if δ is large enough, it can cause a topological phase

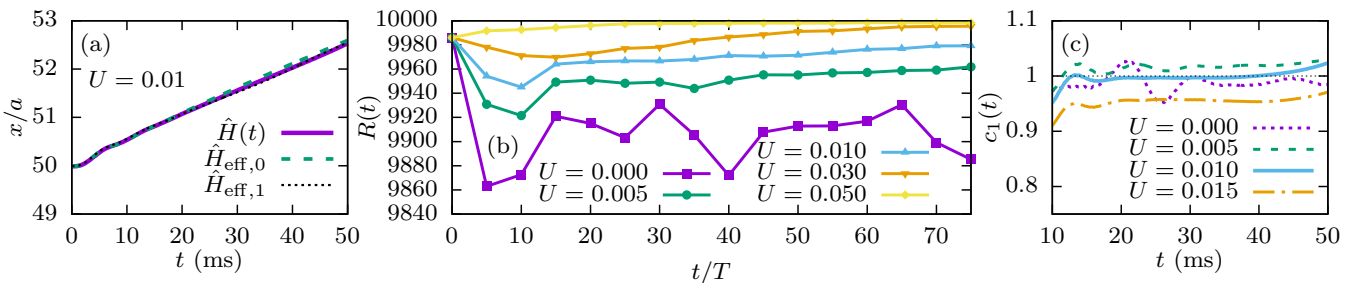


FIG. 10. (a) Comparison of anomalous drifts obtained from evolution using the time-dependent Hamiltonian $\hat{H}(t)$ (solid purple line), effective Hamiltonian without correction $\hat{H}_{\text{eff},0}$ (dashed green line) and effective Hamiltonian with correction $\hat{H}_{\text{eff},1}$ (dotted black line). Intermediate interaction strength $U = 0.01$. U is given in units where $J = 1$. (b) Time evolution of the inverse participation ratio in momentum space for several different values of U . Evolution is performed using the time-dependent Hamiltonian $\hat{H}(t)$. When the interactions are strong enough, IPR approaches the maximal possible value (10 000 in this case), which is equal to the total number of states and corresponds to the completely delocalized state. U is given in units where $J = 1$. (c) Chern number of the lowest band obtained for different interaction strengths as the ratio of the theoretical prediction for the anomalous drift and numerical results: $c_1(t) = (\frac{2fa^2}{\pi\hbar} \int_0^t \gamma_{\text{eff},1}(t') dt') / [x(t) - x(t_0)]$.

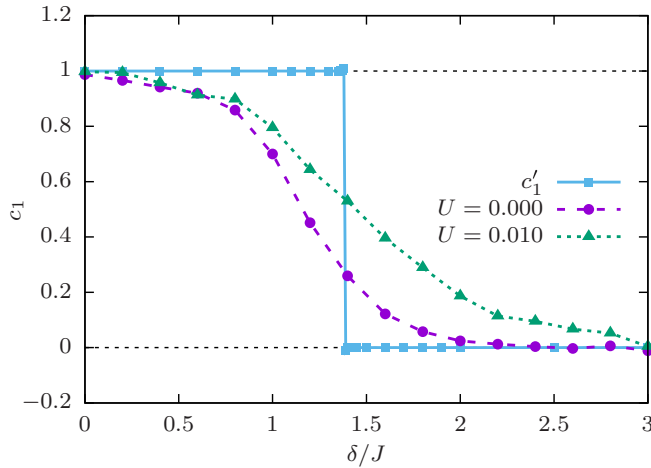


FIG. 11. Lowest band Chern numbers extracted from numerical data for several different values of detuning δ . Purple circles: non-interacting case, $U = 0$. Green triangles: $U = 0.01$. Blue squares: theoretical values of the lowest band Chern number c'_1 . A topological phase transition is visible at $\delta_c \approx 1.38$. The lines between points are only a guide to the eye.

transition and make all bands topologically trivial. By numerically calculating the Berry curvature and Chern numbers c'_i , we find that this transition occurs at $\delta_c \approx 1.38 J$; see Fig. 11. This value is lower than the one for the ordinary Harper-Hofstadter Hamiltonian for $\alpha = 1/4$, which is $\delta_c = 2 J$ [26], due to the different hopping amplitudes J'_x and J'_y , and due to the additional J_x^2/ω correction that we consider.

We now investigate how this topological transition can be probed through the dynamical protocol used in the experiment. We again numerically calculate the anomalous drift and the evolution of the filling factor, but now with staggered detuning (15) included in the Hamiltonian \hat{H}_{initial} (C2) used to obtain the initial state, in the equations of motion (10) and (11), and in the definitions of the band populations $\eta_i(t)$ (C4). Using these results, we repeat the procedure for the extraction of the lowest band Chern number from numerical data that was carried out in the previous section. The Chern number obtained by comparing the anomalous drift to the prediction calculated from the filling factor is then averaged over the time interval $t \in (20, 40)$ ms. This interval was chosen in order to avoid the initial quadratic regime and the finite-size effects at later times. The resulting lowest band Chern numbers for several different values of detuning δ in both the noninteracting case and the case of intermediate interaction strength $U = 0.01$ are presented in Fig. 11.

We can see that the calculated value of the Chern number decreases from $c_1 = 1$ to $c_1 = 0$ with increasing detuning δ . The obtained value of the Chern number is lower than 1 even before the phase transition occurs. This is due to our choice of the initial state, which is not perfectly homogeneous in momentum space. Close to the phase transition, both the energy bands and the Berry curvature have pronounced peaks at the same regions of the first Brillouin zone, and these regions are initially less populated. Because of this, the Berry curvature at these regions contributes less to the anomalous drift, which lowers the measured Chern number. This effect is

somewhat reduced by the interactions, as they smooth out the momentum-space probability density, and might also cancel out the detuning term. Similar interplay of interactions and staggering was observed in the fermionic Hofstadter-Hubbard model [60]. The obtained results are in line with experimental measurements [26].

V. CONCLUSIONS

Motivated by the recent experimental results reporting the Chern numbers of topological bands in cold-atom setups, we studied numerically bosonic transport in a driven optical lattice. The considered driving scheme and the range of microscopic parameters were chosen to be close to those in a recent experimental study [26]. The driving frequency was set to be high enough in order to avoid strong energy absorption for the relevant time scales. Additionally, the system was restricted to a two-dimensional lattice, even though the actual experimental setup had continuous transverse degrees of freedom. This restriction stabilizes the system [29,31,41] and leads to lower heating rates than those in the experiment. It corresponds to the case of strongly confined third dimension.

We investigated bosonic dynamics for the full time-dependent Hamiltonian, the effective Floquet Hamiltonian, and included the effects of weak repulsive interactions between atoms using the mean-field approximation. In the non-interacting case, we found that the effective Hamiltonian and its band structure depend on the frequency of the drive ω through an additional J_x^2/ω correction term. The initial state was set as a mixture of incoherent bosons homogeneously populating the lowest band, but a possible direction of future research could be to simulate the full loading sequence of an initial Bose-Einstein condensate and to try to obtain the incoherent state through driving, as it was done in the experiment.

The main focus of this work is on the effects of weak interactions. For a weak atomic repulsion, atomic transitions to higher effective bands obtained in our simulations mainly occur due to a release of the initial interaction energy during the atomic-cloud expansion. Although the effect is undesirable, it can be properly taken into account in the extraction of the Chern number. At larger interaction strengths, the transitions are more pronounced as the system absorbs energy from the drive. In this regime the good agreement between the full and effective description is lost and the measurement should become more complicated. In addition to causing redistribution of atoms over bands, our results show that weak interactions can also be beneficial in measuring the Chern number. Their desirable effect comes about due to smoothing the atomic distribution over the topological band and due to canceling out the contribution of some less relevant terms to the bosonic dynamics.

ACKNOWLEDGMENTS

This work was supported by the Ministry of Education, Science, and Technological Development of the Republic of Serbia under Projects ON171017, BKMh and TOP-FOP, the Croatian Science Foundation under Grant No. IP-2016-06-5885 SynthMagIA and the TOP-FOP project, and by DAAD (German Academic and Exchange Service) under the BKMh project. Numerical simulations were performed on the PARADOX supercomputing facility at the Scientific Computing

Laboratory of the Institute of Physics Belgrade. This research was funded by the Deutsche Forschungsgemeinschaft (DFG, German Research Foundation) via Research Unit FOR 2414 under project number 277974659. This work was also supported by the Deutsche Forschungsgemeinschaft (DFG) via the high-performance computing center LOEWE-CSC.

APPENDIX A: EFFECTIVE MODEL

After a unitary transformation into the rotating frame $\tilde{\psi} = e^{-i\hat{W}t}\psi$, where $\tilde{\psi}$ and ψ are the old and the new wave functions, and \hat{W} is the staggered potential, the new time-dependent Hamiltonian that describes the experimental setup is given by [26]

$$\hat{H}(t) = J_y \sum_{l,m} (\hat{a}_{l,m+1}^\dagger \hat{a}_{l,m} + \hat{a}_{l,m-1}^\dagger \hat{a}_{l,m}) + \hat{V}^{(+)} e^{i\omega t} + \hat{V}^{(-)} e^{-i\omega t} + \frac{U}{2} \sum_{l,m} \hat{n}_{l,m} (\hat{n}_{l,m} - 1), \quad (\text{A1})$$

where

$$\hat{V}^{(+)} = \kappa/2 \sum_{l,m} \hat{n}_{l,m} g(l, m) - J_x \sum_{l_{\text{odd}}, m} (\hat{a}_{l+1,m}^\dagger \hat{a}_{l,m} + \hat{a}_{l-1,m}^\dagger \hat{a}_{l,m}), \quad (\text{A2})$$

$$\hat{V}^{(-)} = \kappa/2 \sum_{l,m} \hat{n}_{l,m} g^*(l, m) - J_x \sum_{l_{\text{even}}, m} (\hat{a}_{l+1,m}^\dagger \hat{a}_{l,m} + \hat{a}_{l-1,m}^\dagger \hat{a}_{l,m}), \quad (\text{A3})$$

$$g(l, m) = \cos(l\pi/2 - \pi/4) e^{i(\phi_0 - m\pi/2)} + \cos(l\pi/2 + \pi/4) e^{i(m\pi/2 - \phi_0 - \pi/2)}. \quad (\text{A4})$$

The kick operator is given by

$$\hat{K}(t) = \frac{1}{i\omega} (\hat{V}^{(+)} e^{i\omega t} - \hat{V}^{(-)} e^{-i\omega t}) + O\left(\frac{1}{\omega^2}\right) \quad (\text{A5})$$

and the effective Hamiltonian by

$$\hat{H}_{\text{eff}} = \underbrace{\hat{H}_0}_{\hat{H}_{\text{eff}}^{(0)}} + \underbrace{\frac{1}{\omega} [\hat{V}^{(+)}, \hat{V}^{(-)}]}_{\hat{H}_{\text{eff}}^{(1)}} + \underbrace{\frac{1}{2\omega^2} ([[\hat{V}^{(+)}, \hat{H}_0], \hat{V}^{(-)}] + [[\hat{V}^{(-)}, \hat{H}_0], \hat{V}^{(+)}])}_{\hat{H}_{\text{eff}}^{(2)}} + O\left(\frac{1}{\omega^3}\right). \quad (\text{A6})$$

If we assume that the driving frequency is high and interactions are weak, the interaction term and almost all $O(\frac{1}{\omega^2})$ terms can be neglected. After substituting Eqs. (A1), (A2), and (A3) into Eq. (A6) we obtain

$$\hat{H}_{\text{eff}}^{(0)} = -J_y \sum_{l,m} (\hat{a}_{l,m+1}^\dagger \hat{a}_{l,m} + \hat{a}_{l,m-1}^\dagger \hat{a}_{l,m}), \quad (\text{A7})$$

$$\hat{H}_{\text{eff}}^{(1)} = \frac{1}{\omega} \left[\frac{\kappa}{2} \sum_{l,m} \hat{a}_{l,m}^\dagger \hat{a}_{l,m} g(l, m) - J_x \sum_{l_{\text{odd}}, m} (\hat{a}_{l+1,m}^\dagger \hat{a}_{l,m} + \hat{a}_{l-1,m}^\dagger \hat{a}_{l,m}), \right. \quad (\text{A8})$$

$$\left. \frac{\kappa}{2} \sum_{l,m} \hat{a}_{l,m}^\dagger \hat{a}_{l,m} g^*(l, m) - J_x \sum_{l_{\text{even}}, m} (\hat{a}_{l+1,m}^\dagger \hat{a}_{l,m} + \hat{a}_{l-1,m}^\dagger \hat{a}_{l,m}) \right] = \hat{H}_1 + \hat{H}_2 + \hat{H}_3 + \hat{H}_4.$$

We will now separately calculate each term:

$$\begin{aligned} \hat{H}_1 &= -\frac{J_x \kappa}{2\omega} \sum_{l_{\text{odd}}, m, l', m'} g^*(l', m') [\hat{a}_{l+1,m}^\dagger \hat{a}_{l,m} + \hat{a}_{l-1,m}^\dagger \hat{a}_{l,m}, \hat{a}_{l',m'}^\dagger \hat{a}_{l',m'}] \\ &= -\frac{J_x \kappa}{2\omega} \sum_{l_{\text{odd}}, m} [(g^*(l, m) - g^*(l+1, m)) \hat{a}_{l+1,m}^\dagger \hat{a}_{l,m} + (g^*(l, m) - g^*(l-1, m)) \hat{a}_{l-1,m}^\dagger \hat{a}_{l,m}], \end{aligned} \quad (\text{A9})$$

$$\begin{aligned} \hat{H}_2 &= -\frac{J_x \kappa}{2\omega} \sum_{l_{\text{even}}, m, l', m'} g(l', m') [\hat{a}_{l',m'}^\dagger \hat{a}_{l',m'}, \hat{a}_{l+1,m}^\dagger \hat{a}_{l,m} + \hat{a}_{l-1,m}^\dagger \hat{a}_{l,m}] \\ &= \frac{J_x \kappa}{2\omega} \sum_{l_{\text{even}}, m} [(g(l, m) - g(l+1, m)) \hat{a}_{l+1,m}^\dagger \hat{a}_{l,m} + (g(l, m) - g(l-1, m)) \hat{a}_{l-1,m}^\dagger \hat{a}_{l,m}], \end{aligned} \quad (\text{A10})$$

$$\begin{aligned} \hat{H}_3 &= \frac{J_x^2}{\omega} \sum_{l_{\text{odd}}, m, l'_{\text{even}}, m'} [\hat{a}_{l+1,m}^\dagger \hat{a}_{l,m} + \hat{a}_{l-1,m}^\dagger \hat{a}_{l,m}, \hat{a}_{l'+1,m'}^\dagger \hat{a}_{l',m'} + \hat{a}_{l'-1,m'}^\dagger \hat{a}_{l',m'}] \\ &= \frac{J_x^2}{\omega} \sum_{l_{\text{odd}}, m} (2\hat{a}_{l+1,m}^\dagger \hat{a}_{l+1,m} + \hat{a}_{l+3,m}^\dagger \hat{a}_{l+1,m} + \hat{a}_{l-1,m}^\dagger \hat{a}_{l+1,m} - 2\hat{a}_{l,m}^\dagger \hat{a}_{l,m} - \hat{a}_{l+2,m}^\dagger \hat{a}_{l,m} - \hat{a}_{l-2,m}^\dagger \hat{a}_{l,m}) \\ &= \frac{J_x^2}{\omega} \sum_{l,m} (-1)^l (2\hat{a}_{l,m}^\dagger \hat{a}_{l,m} + \hat{a}_{l+2,m}^\dagger \hat{a}_{l,m} + \hat{a}_{l-2,m}^\dagger \hat{a}_{l,m}), \end{aligned} \quad (\text{A11})$$

$$\hat{H}_4 = \frac{\kappa^2}{4\omega} \sum_{l,m,l',m'} g(l,m)g^*(l',m')[\hat{a}_{l,m}^\dagger \hat{a}_{l,m}, \hat{a}_{l',m'}^\dagger \hat{a}_{l',m'}] = 0. \quad (\text{A12})$$

Using trigonometric identities and

$$g(l,m) - g(l \pm 1, m) = \pm \sqrt{2}(\sin[(2l \pm 1 - 1)\pi/4]e^{i(\pi/4 - m\pi/2)} + \sin[(2l \pm 1 + 1)\pi/4]e^{i(m\pi/2 - 3\pi/4)}), \quad (\text{A13})$$

we can rewrite the sum of terms (A9) and (A10) in a more convenient form:

$$\hat{H}_1 + \hat{H}_2 = \frac{J_x \kappa}{\sqrt{2}\omega} \sum_{l,m} (e^{i(m-l)\pi/2 - \pi/4} \hat{a}_{l,m}^\dagger \hat{a}_{l-1,m} + e^{-i(m-l-1)\pi/2 - \pi/4} \hat{a}_{l,m}^\dagger \hat{a}_{l+1,m}). \quad (\text{A14})$$

The only $O(\frac{1}{\omega^2})$ ($\hat{H}_{\text{eff}}^{(2)}$) term that cannot be neglected in the parameter range that we use is [26]

$$\frac{J_y}{2} \frac{\kappa^2}{\omega^2} \sum_{l,m} (\hat{a}_{l,m+1}^\dagger \hat{a}_{l,m} + \hat{a}_{l,m-1}^\dagger \hat{a}_{l,m}). \quad (\text{A15})$$

Finally, the effective Hamiltonian becomes

$$\hat{H}_{\text{eff},1} = \frac{J_x \kappa}{\sqrt{2}\omega} \sum_{l,m} (e^{i(m-l-1)\pi/2 - \pi/4} \hat{a}_{l+1,m}^\dagger \hat{a}_{l,m} + e^{-i(m-l)\pi/2 - \pi/4} \hat{a}_{l-1,m}^\dagger \hat{a}_{l,m}) - J_y \left(1 - \frac{1}{2} \frac{\kappa^2}{\omega^2}\right) \sum_{l,m} (\hat{a}_{l,m+1}^\dagger \hat{a}_{l,m} + \hat{a}_{l,m-1}^\dagger \hat{a}_{l,m}) \quad (\text{A16})$$

$$+ \frac{J_x^2}{\omega} \sum_{l,m} (-1)^l (2\hat{a}_{l,m}^\dagger \hat{a}_{l,m} + \hat{a}_{l+2,m}^\dagger \hat{a}_{l,m} + \hat{a}_{l-2,m}^\dagger \hat{a}_{l,m}), \quad (\text{A17})$$

with the renormalized nearest-neighbor hopping amplitudes $J'_x = \frac{J_x \kappa}{\sqrt{2}\omega} = J_y$ and $J'_y = J_y(1 - \frac{1}{2} \frac{\kappa^2}{\omega^2})$, and a next-nearest-neighbor along \mathbf{e}_x hopping term proportional to $\frac{J_x^2}{\omega}$ in (A17).

APPENDIX B: EFFECTIVE HAMILTONIAN IN MOMENTUM SPACE

If we choose the unit cell as in Fig. 1(a) [lattice sites A = (1, 0), B = (2, 0), C = (3, 0), and D = (4, 0)], the momentum-space representation of the effective Hamiltonian without correction $\hat{H}_{\text{eff},0}$ (6) is given by a 4×4 matrix

$$\hat{\mathcal{H}}_{\text{eff},0}(\mathbf{k}) = \begin{pmatrix} 0 & J'_x e^{-i\frac{3\pi}{4}} - J'_y e^{-i\mathbf{k}\cdot\mathbf{R}_2} & 0 & J'_x e^{-i\frac{3\pi}{4} - i\mathbf{k}\cdot\mathbf{R}_1} - J'_y e^{i\mathbf{k}\cdot(\mathbf{R}_2 - \mathbf{R}_1)} \\ J'_x e^{i\frac{3\pi}{4}} - J'_y e^{i\mathbf{k}\cdot\mathbf{R}_2} & 0 & J'_x e^{-i\frac{\pi}{4}} - J'_y e^{-i\mathbf{k}\cdot\mathbf{R}_2} & 0 \\ 0 & J'_x e^{i\frac{\pi}{4}} - J'_y e^{i\mathbf{k}\cdot\mathbf{R}_2} & 0 & J'_x e^{i\frac{\pi}{4}} - J'_y e^{-i\mathbf{k}\cdot\mathbf{R}_2} \\ J'_x e^{i\frac{3\pi}{4} + i\mathbf{k}\cdot\mathbf{R}_1} - J'_y e^{i\mathbf{k}\cdot(\mathbf{R}_1 - \mathbf{R}_2)} & 0 & J'_x e^{-i\frac{\pi}{4}} - J'_y e^{i\mathbf{k}\cdot\mathbf{R}_2} & 0 \end{pmatrix}, \quad (\text{B1})$$

where \mathbf{R}_1 and \mathbf{R}_2 are the lattice vectors $\mathbf{R}_1 = (4, 0)$ and $\mathbf{R}_2 = (1, 1)$ and \mathbf{k} is in the first Brillouin zone, which is given by the reciprocal lattice vectors $\mathbf{b}_1 = \frac{\pi}{2}(1, -1)$ and $\mathbf{b}_2 = 2\pi(0, 1)$.

When the $\frac{J_x^2}{\omega}$ correction is included in the effective Hamiltonian, $\hat{H}_{\text{eff},1}$ (7), the unit cell is doubled, see Fig. 1(b), and the first Brillouin zone is therefore halved. If we now choose the lattice sites a = (1, 0), B = (2, 0), c = (3, 0), D = (4, 0), A = (2, 1), b = (3, 1), C = (4, 1), and d = (5, 1) for the unit cell, the momentum-space representation of the effective Hamiltonian will be an 8×8 matrix

$$\hat{\mathcal{H}}_{\text{eff},1}(\mathbf{k}) = \begin{pmatrix} -\frac{2J_x^2}{\omega} & J'_x e^{-i\frac{3\pi}{4}} & -\frac{J_x^2}{\omega}(1 + e^{i\mathbf{k}\cdot\mathbf{R}_1}) & J'_x e^{-i(\frac{3\pi}{4} - \mathbf{k}\cdot\mathbf{R}_1)} & 0 & -J'_y e^{i\mathbf{k}\cdot\mathbf{R}_2} & 0 & -J'_y e^{i\mathbf{k}\cdot\mathbf{R}_1} \\ J'_x e^{i\frac{3\pi}{4}} & \frac{2J_x^2}{\omega} & J'_x e^{-i\frac{\pi}{4}} & \frac{J_x^2}{\omega}(1 + e^{i\mathbf{k}\cdot\mathbf{R}_1}) & -J'_y & 0 & -J'_y e^{i\mathbf{k}\cdot\mathbf{R}_2} & 0 \\ -\frac{J_x^2}{\omega}(1 + e^{-i\mathbf{k}\cdot\mathbf{R}_1}) & J'_x e^{i\frac{\pi}{4}} & -\frac{2J_x^2}{\omega} & J'_x e^{i\frac{\pi}{4}} & 0 & -J'_y & 0 & -J'_y e^{i\mathbf{k}\cdot\mathbf{R}_2} \\ J'_x e^{i(\frac{3\pi}{4} - \mathbf{k}\cdot\mathbf{R}_1)} & \frac{J_x^2}{\omega}(1 + e^{-i\mathbf{k}\cdot\mathbf{R}_1}) & J'_x e^{-i\frac{\pi}{4}} & \frac{2J_x^2}{\omega} & -J'_y e^{-i\mathbf{k}\cdot(\mathbf{R}_1 - \mathbf{R}_2)} & 0 & -J'_y & 0 \\ 0 & 0 & 0 & -J'_y e^{i\mathbf{k}\cdot(\mathbf{R}_1 - \mathbf{R}_2)} & \frac{2J_x^2}{\omega} & J'_x e^{-i\frac{3\pi}{4}} & \frac{J_x^2}{\omega}(1 + e^{i\mathbf{k}\cdot\mathbf{R}_1}) & J'_x e^{-i(\frac{3\pi}{4} - \mathbf{k}\cdot\mathbf{R}_1)} \\ -J'_y e^{-i\mathbf{k}\cdot\mathbf{R}_2} & 0 & -J'_y & 0 & J'_x e^{i\frac{3\pi}{4}} & -\frac{2J_x^2}{\omega} & J'_x e^{-i\frac{\pi}{4}} & -\frac{J_x^2}{\omega}(1 + e^{i\mathbf{k}\cdot\mathbf{R}_1}) \\ 0 & -J'_y e^{-i\mathbf{k}\cdot\mathbf{R}_2} & 0 & -J'_y & \frac{J_x^2}{\omega}(1 + e^{-i\mathbf{k}\cdot\mathbf{R}_1}) & J'_x e^{i\frac{\pi}{4}} & \frac{2J_x^2}{\omega} & J'_x e^{i\frac{\pi}{4}} \\ -J'_y e^{-i\mathbf{k}\cdot\mathbf{R}_1} & 0 & -J'_y e^{-i\mathbf{k}\cdot\mathbf{R}_2} & 0 & J'_x e^{i(\frac{3\pi}{4} - \mathbf{k}\cdot\mathbf{R}_1)} & -\frac{J_x^2}{\omega}(1 + e^{-i\mathbf{k}\cdot\mathbf{R}_1}) & J'_x e^{-i\frac{\pi}{4}} & -\frac{2J_x^2}{\omega} \end{pmatrix}, \quad (\text{B2})$$

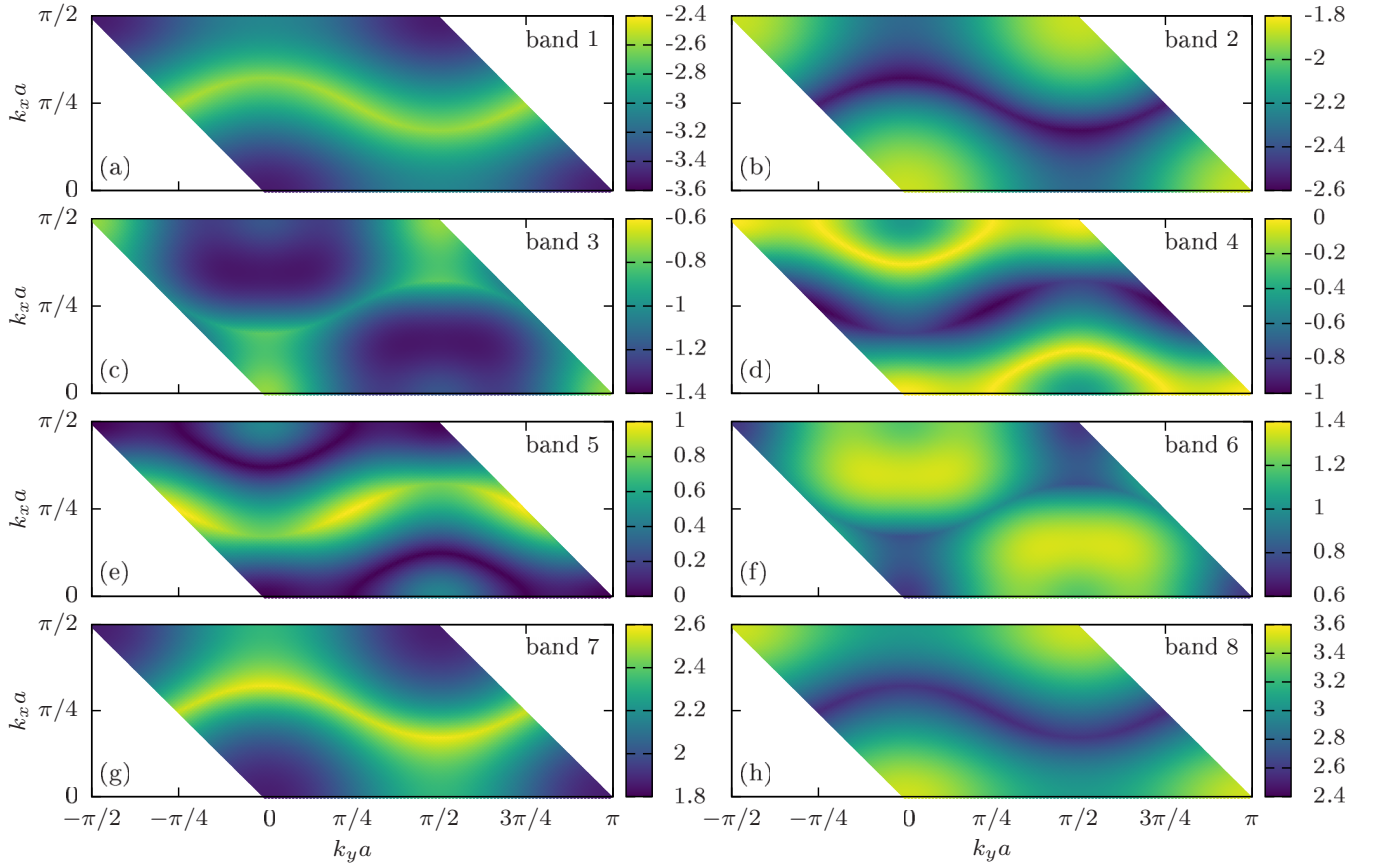


FIG. 12. Eight energy subbands of $\hat{\mathcal{H}}_{\text{eff},1}(\mathbf{k})$ for the driving frequency $\omega = 20$. Subbands 1 and 2 form the lowest band with Chern number $c_1 = 1$, subbands 3, 4, 5, and 6 form the middle band with $c_2 = -2$, and subbands 7 and 8 form the highest band with $c_3 = 1$.

with the lattice vectors $\mathbf{R}_1 = (4, 0)$ and $\mathbf{R}_2 = (2, 2)$. The reciprocal lattice vectors are then $\mathbf{b}_1 = \frac{\pi}{2}(1, -1)$ and $\mathbf{b}_2 = \pi(0, 1)$.

The energy bands of $\hat{\mathcal{H}}_{\text{eff},1}(\mathbf{k})$ are shown in Figs. 2 and 12.

APPENDIX C: DESCRIPTION OF INCOHERENT BOSONS

In a typical condensed-matter system constituent particles are electrons. Due to their fermionic statistics, at low enough temperatures, and with Fermi energy above the lowest band, that band of the topological model is uniformly occupied, and consequently the transverse Hall conductivity can be expressed in terms of the Chern number (8) [10]. In contrast, weakly interacting bosons in equilibrium form a Bose-Einstein condensate in the band minima and only probe the local Berry curvature [21].

Yet in the experiment [26] the Chern number was successfully measured using bosonic atoms of ^{87}Rb . This was possible because in the process of ramping up the drive (4), the initial Bose-Einstein condensate was transferred into an incoherent bosonic mixture. Conveniently, it turned out that the bosonic distribution over the states of the lowest band of the effective Floquet Hamiltonian was nearly uniform. Motivated by the experimental procedure, we model the initial

bosonic state by a statistical matrix

$$\rho(t=0) = \prod_{k=1}^{N_m} |k, N_p\rangle\langle k, N_p|, \quad (\text{C1})$$

where the states $|k\rangle = a_k^\dagger|0\rangle$ approximately correspond to the lowest-band eigenstates of \hat{H}_{eff} and each of these N_m states is occupied by N_p atoms $|k, N_p\rangle = \mathcal{N}(a_k^\dagger)^{N_p}|0\rangle$.

A procedure for selecting the states $|k\rangle$ is described in Refs. [22,26]. In order to probe the Chern number of the lowest band, the states $|k\rangle$ should correspond closely to the lowest-band eigenstates of \hat{H}_{eff} . At the same time, in the experiment in the initial moment the atomic cloud is spatially localized. According to Refs. [22,26] the optimal approach is to consider a steep confining potential and to use the low-lying eigenstates of

$$\hat{H}_{\text{initial}} = \hat{h}^{\text{eff}} + \left(\frac{r}{r_0}\right)^\zeta, \quad (\text{C2})$$

where in our calculations \hat{h}^{eff} is either $\hat{H}_{\text{eff},0}$ from Eq. (6) or $\hat{H}_{\text{eff},1}$ from Eq. (7) and the parameters of the confining potential are set to $r_0 = 20$, $\zeta = 20$.

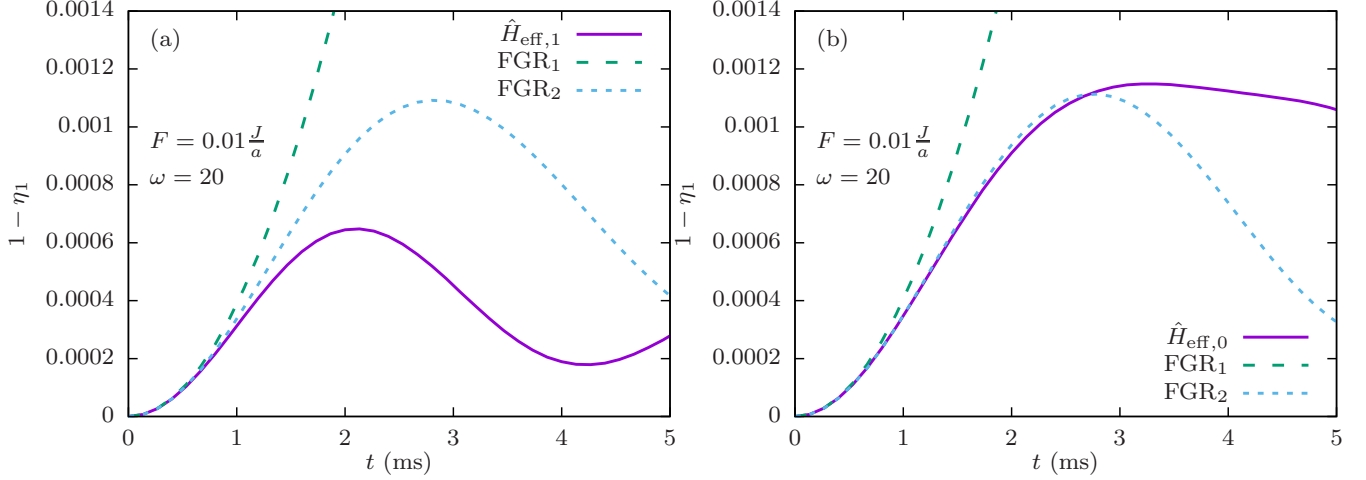


FIG. 13. Population in higher bands, comparison of numerical results (solid line) with the Fermi's golden rule in the first and second approximation (dashed lines). Band populations are calculated for an initial BEC in an eigenstate of the effective Hamiltonian and then averaged over (approximately) all states in the first band. (a) Initial state and evolution from the effective Hamiltonian with correction $\hat{H}_{\text{eff},1}$, Eq. (7). (b) Without the correction, $\hat{H}_{\text{eff},0}$, Eq. (6).

The dynamics of the initial state (C1) is induced by a double quench: at $t_0 = 0$ the atomic cloud is released from the confining potential and exposed to a uniform force of intensity F along the y direction. During the whole procedure the driving providing the laser-assisted tunneling, defined in Eq. (4), is running.

The main observables of interest are the center-of-mass position along x direction

$$x(t) = \left\langle \sum_{l,m} l |\psi_{l,m}(t)|^2 \right\rangle \quad (\text{C3})$$

and the population of the i th band of the effective model

$$\eta_i(t) = \left\langle \sum_{|k\rangle \in i\text{th band}} \left| \sum_{l,m} \alpha_{lm}^{k*} \psi_{lm}(t) \right|^2 \right\rangle, \quad (\text{C4})$$

where the states $|k\rangle = \sum_{l,m} \alpha_{lm}^k |l, m\rangle$ correspond to the eigenstates of the effective model. Here, angle brackets $\langle \rangle$ denote averaging over N_{samples} sets of initial conditions.

In the case of noninteracting particles, these and other quantities can be numerically accessed by solving the single-particle time-dependent Schrödinger equation for N_m different initial states $|k\rangle$. This is equivalent to sampling the initial state according to Eq. (9).

In the end, we give two technical remarks. First, all our calculations are done in the rotating frame; see Eq. (A1) in Appendix A. The staggered potential (2) is removed in this way. Second, in the case when the evolution is governed by the time-dependent Hamiltonian (10), the initial state is multiplied by the operator $e^{-i\hat{K}(0)}$ in order to properly compare these results to the ones obtained from the evolution governed by the effective Hamiltonian (11); see Eq. (5).

APPENDIX D: INITIAL QUADRATIC REGIME

For simplicity, we will consider only the case without the confining potential and with very weak force $F = 0.01$.

The initial state is a Bose-Einstein condensate in one of the eigenstates of the effective Hamiltonian. The results are later averaged over all first band eigenstates.

Fermi's golden rule predicts that the probability for transition from an initial state ψ_i to a final state ψ_f , induced by a perturbation $\Delta\hat{H}$, is proportional to the square of matrix elements $|\langle\psi_i|\Delta\hat{H}|\psi_f\rangle|^2$. In this case, the perturbation is $\Delta\hat{H} = F\hat{y}$. If we assume that the probability of a particle being in the initial state is always $P_i(t) = |\psi_i(t)|^2 \approx 1$, Fermi's golden rule predicts [61]

$$P_{i \rightarrow f}^{\text{FGR}_1}(t) = \frac{1}{\hbar^2} |\langle\psi_i|\Delta\hat{H}|\psi_f\rangle|^2 t^2. \quad (\text{D1})$$

If we now also consider transitions from the other states to the initial state, but keep the assumption that the populations in other states are small $P_{j \neq i}(t) = |\psi_{j \neq i}(t)|^2 \ll 1$, the time-dependent perturbation theory then predicts [61]

$$P_{i \rightarrow f}^{\text{FGR}_2}(t) = |\langle i|\Delta\hat{H}|f\rangle|^2 \frac{1 - 2e^{-\frac{\Gamma}{2\hbar}t} \cos\left(\frac{E_f - E_i}{\hbar}t\right) + e^{-\frac{\Gamma}{\hbar}t}}{(E_f - E_i)^2 + \frac{\Gamma^2}{4}}, \quad (\text{D2})$$

where $\Gamma = \frac{2\pi}{\hbar} |\langle i|\Delta\hat{H}|f\rangle|^2$ and E_i (E_f) is the energy of the initial (final) state.

We plot the numerical results and both theoretical predictions from Fermi's golden rule in Fig. 13. Here we can see that all three curves agree well for short times, the second approximation longer remains close to the numerical results, and that the initial quadratic regime is reproduced by theory. This is the so-called quantum Zeno regime [57].

APPENDIX E: ENERGY

Time evolution of kinetic and interaction energy per particle for different interaction strengths is plotted in Fig. 14. Here we define the kinetic energy per particle as the expectation value of the time-dependent Hamiltonian (A1) divided by the total number of particles $E_{\text{kin}}(t) = \frac{1}{N} \langle \sum_{l,m,i,j} \psi_{l,m}^* \psi_{l,m} \rangle$

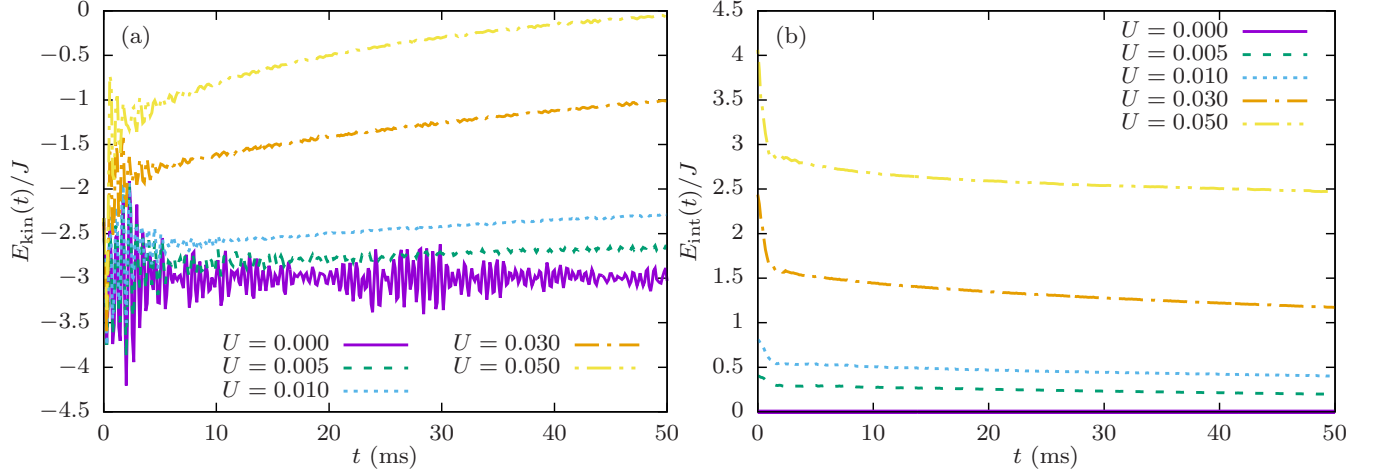


FIG. 14. (a) Kinetic energy per particle (expectation value of the time-dependent Hamiltonian $E_{\text{kin}}(t) = \frac{1}{N} \langle \sum_{l,m,i,j} \psi_{l,m}^*(t) H_{l,m,i,j}(t) \psi_{l,m}(t) \rangle$) divided by the total number of particles N for several different interaction strengths. (b) Interaction energy per particle $E_{\text{int}}(t) = \frac{1}{N} \frac{U}{2} \langle \sum_{l,m} |\psi_{l,m}(t)|^2 [|\psi_{l,m}(t)|^2 - 1] \rangle$. U is given in units where $J = 1$.

$H_{l,m,i,j}(t) \psi_{l,m}(t)$, while the interaction energy per particle is $E_{\text{int}}(t) = \frac{1}{N} \frac{U}{2} \langle \sum_{l,m} |\psi_{l,m}(t)|^2 [|\psi_{l,m}(t)|^2 - 1] \rangle$. Both energies grow with increasing interaction coefficient U .

When the interactions are strong enough and after long enough time, the atoms become equally distributed between the eigenstates of the Hamiltonian $\hat{H}(t)$. As the energy spectrum of $\hat{H}(t)$ is symmetric around zero, the expectation value of $\hat{H}(t)$ (kinetic energy) should be zero when all bands are equally populated. We can see this in Fig. 14(a), where the kinetic energy approaches zero at $t \approx 50$ ms for the case $U = 0.05$.

The interaction energy at first rapidly decreases, as the cloud rapidly expands after turning off the confinement

potential \hat{V}_{conf} , and after that continues to slowly decrease as the cloud slowly expands; see Fig. 14(b).

These considerations also provide a possibility to discuss the applicability of the approximative method introduced in Sec. IV. As we work in the regime of high frequency $\omega = 20$, we find that for weak interaction, at short enough times of propagation, the energy is approximately conserved. At stronger values of $U \geq 0.01$ we observe a slow increase in the total energy on the considered time scales. In both cases we do not find the onset of parametric instabilities [31]. If present, these instabilities are signaled by an order of magnitude increase in energy on a short time scale, that we do not find.

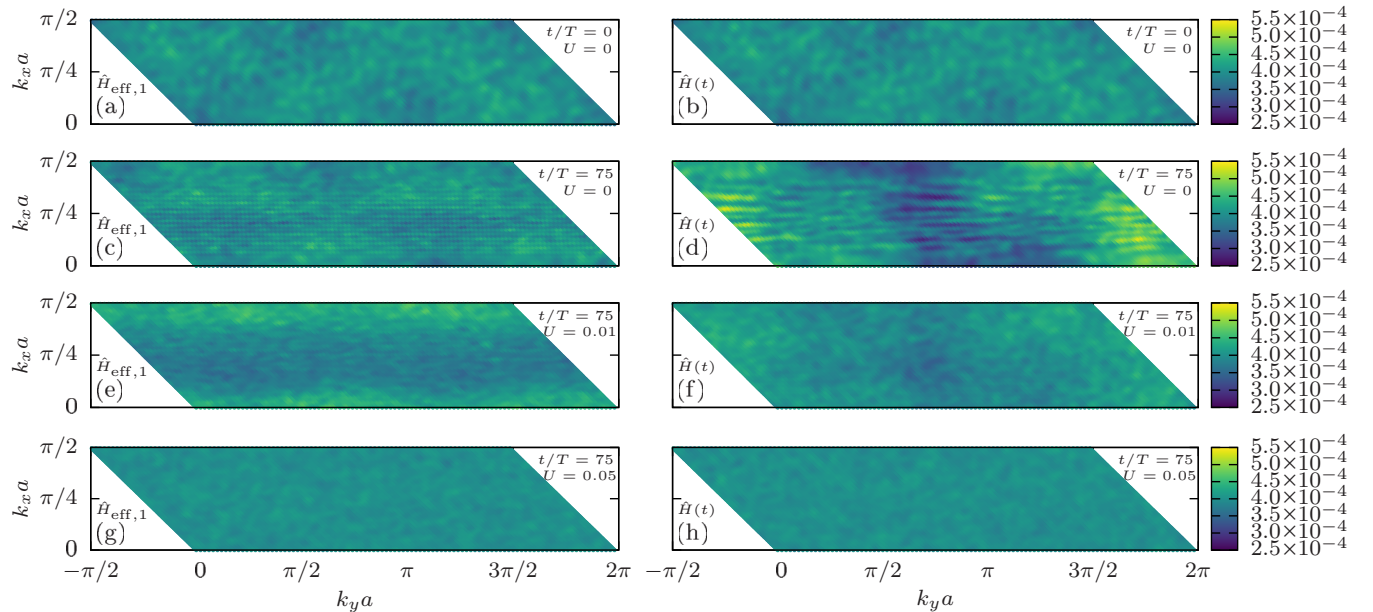


FIG. 15. Momentum-space density distribution in all bands, $\eta_1(\mathbf{k}) + \eta_2(\mathbf{k}) + \eta_3(\mathbf{k})$. U is given in units where $J = 1$. Left: evolution using the time-dependent Hamiltonian $\hat{H}_{\text{eff},1}$. Right: evolution using the time-dependent Hamiltonian $\hat{H}(t)$. (a), (b) Initial state. (c), (d) Final state after 50 ms (75 driving periods), noninteracting case $U = 0$. (e), (f) $U = 0.01$. (g), (h) $U = 0.05$.

In addition, the two-body interaction can deplete the occupancies of initial coherent modes [29,41] and limit the validity of our approach. In principle, these types of processes can be addressed by including quantum fluctuations along the lines of the full truncated Wigner approach [45]. Yet, we set our parameters in such a way that these additional contributions are small.

APPENDIX F: MOMENTUM-SPACE DENSITY DISTRIBUTION

The momentum-space probability densities at the initial moment and after 75 driving periods (50 ms) are shown in Fig. 15. The interactions deplete the lowest band, but also smooth out the density distribution.

-
- [1] I. Bloch, J. Dalibard, and W. Zwerger, *Rev. Mod. Phys.* **80**, 885 (2008).
- [2] Y.-J. Lin, R. L. Compton, K. Jiménez-García, J. V. Porto, and I. B. Spielman, *Nature (London)* **462**, 628 (2009).
- [3] J. Dalibard, F. Gerbier, G. Juzeliūnas, and P. Öhberg, *Rev. Mod. Phys.* **83**, 1523 (2011).
- [4] D. R. Hofstadter, *Phys. Rev. B* **14**, 2239 (1976).
- [5] F. D. M. Haldane, *Phys. Rev. Lett.* **61**, 2015 (1988).
- [6] M. Aidelsburger, M. Atala, M. Lohse, J. T. Barreiro, B. Paredes, and I. Bloch, *Phys. Rev. Lett.* **111**, 185301 (2013).
- [7] H. Miyake, G. A. Siviloglou, C. J. Kennedy, W. C. Burton, and W. Ketterle, *Phys. Rev. Lett.* **111**, 185302 (2013).
- [8] G. Jotzu, M. Messer, R. Desbuquois, M. Lebrat, T. Uehlinger, D. Greif, and T. Esslinger, *Nature (London)* **515**, 237 (2014).
- [9] M. E. Tai, A. Lukin, M. Rispoli, R. Schittko, T. Menke, D. Borgnia, P. M. Preiss, F. Grusdt, A. M. Kaufman, and M. Greiner, *Nature (London)* **546**, 519 (2017).
- [10] D. J. Thouless, M. Kohmoto, M. P. Nightingale, and M. den Nijs, *Phys. Rev. Lett.* **49**, 405 (1982).
- [11] G. Floquet, *Ann. Sci. Éc. Norm. Supér.* **12**, 47 (1883).
- [12] M. Grifoni and P. Hänggi, *Phys. Rep.* **304**, 229 (1998).
- [13] N. Goldman and J. Dalibard, *Phys. Rev. X* **4**, 031027 (2014).
- [14] N. Goldman, J. Dalibard, M. Aidelsburger, and N. R. Cooper, *Phys. Rev. A* **91**, 033632 (2015).
- [15] A. Eckardt and E. Anisimovas, *New J. Phys.* **17**, 093039 (2015).
- [16] M. Aidelsburger, S. Nascimbène, and N. Goldman, *C. R. Phys.* (2018), doi:10.1016/j.crhy.2018.03.002.
- [17] A. Eckardt, *Rev. Mod. Phys.* **89**, 011004 (2017).
- [18] N. R. Cooper, J. Dalibard, and I. B. Spielman, [arXiv:1803.00249](https://arxiv.org/abs/1803.00249) [Rev. Mod. Phys. (to be published)].
- [19] G. Sun and A. Eckardt, [arXiv:1805.02443](https://arxiv.org/abs/1805.02443).
- [20] K. M. Fujiwara, K. Singh, Z. A. Geiger, R. Senaratne, S. Rajagopal, M. Lipatov, and D. M. Weld, [arXiv:1806.07858](https://arxiv.org/abs/1806.07858).
- [21] H. M. Price and N. R. Cooper, *Phys. Rev. A* **85**, 033620 (2012).
- [22] A. Dauphin and N. Goldman, *Phys. Rev. Lett.* **111**, 135302 (2013).
- [23] M. Bukov and A. Polkovnikov, *Phys. Rev. A* **90**, 043613 (2014).
- [24] H. M. Price, O. Zilberberg, T. Ozawa, I. Carusotto, and N. Goldman, *Phys. Rev. B* **93**, 245113 (2016).
- [25] S. Mugel, A. Dauphin, P. Massignan, L. Tarruell, M. Lewenstein, C. Lobo, and A. Celi, *SciPost Phys.* **3**, 012 (2017).
- [26] M. Aidelsburger, M. Lohse, C. Schweizer, M. Atala, J. T. Barreiro, S. Nascimbène, N. R. Cooper, I. Bloch, and N. Goldman, *Nat. Phys.* **11**, 162 (2015).
- [27] L. D'Alessio and M. Rigol, *Phys. Rev. X* **4**, 041048 (2014).
- [28] M. Bukov, S. Gopalakrishnan, M. Knap, and E. Demler, *Phys. Rev. Lett.* **115**, 205301 (2015).
- [29] S. Choudhury and E. J. Mueller, *Phys. Rev. A* **92**, 063639 (2015).
- [30] C. J. Kennedy, W. C. Burton, W. C. Chung, and W. Ketterle, *Nat. Phys.* **11**, 859 (2015).
- [31] S. Lellouch, M. Bukov, E. Demler, and N. Goldman, *Phys. Rev. X* **7**, 021015 (2017).
- [32] K. Plekhanov, G. Roux, and K. Le Hur, *Phys. Rev. B* **95**, 045102 (2017).
- [33] S. Lellouch and N. Goldman, *Quantum Sci. Technol.* **3**, 024011 (2018).
- [34] E. Michon, C. Cabrera-Gutiérrez, A. Fortun, M. Berger, M. Arnal, V. Brunaud, J. Billy, C. Petitjean, P. Schlagheck, and D. Guéry-Odelin, *New J. Phys.* **20**, 053035 (2018).
- [35] J. Näger, K. Wintersperger, M. Bukov, S. Lellouch, E. Demler, U. Schneider, I. Bloch, N. Goldman, and M. Aidelsburger, [arXiv:1808.07462](https://arxiv.org/abs/1808.07462).
- [36] T. Boulier, J. Maslek, M. Bukov, C. Bracamontes, E. Magnan, S. Lellouch, E. Demler, N. Goldman, and J. V. Porto, [arXiv:1808.07637](https://arxiv.org/abs/1808.07637).
- [37] K. Lelas, N. Drpić, T. Dubček, D. Jukić, R. Pezer, and H. Buljan, *New J. Phys.* **18**, 095002 (2016).
- [38] J. Motruk and F. Pollmann, *Phys. Rev. B* **96**, 165107 (2017).
- [39] W. W. Ho and D. A. Abanin, [arXiv:1611.05024](https://arxiv.org/abs/1611.05024).
- [40] A. Dauphin, D.-T. Tran, M. Lewenstein, and N. Goldman, *2D Mater.* **4**, 024010 (2017).
- [41] T. Bilitewski and N. R. Cooper, *Phys. Rev. A* **91**, 063611 (2015).
- [42] M. V. Berry, *Proc. R. Soc. London A* **392**, 45 (1984).
- [43] T. Fukui, Y. Hatsugai, and H. Suzuki, *J. Phys. Soc. Jpn.* **74**, 1674 (2005).
- [44] Y. Kagan and B. V. Svistunov, *Phys. Rev. Lett.* **79**, 3331 (1997).
- [45] A. Polkovnikov, *Ann. Phys. (N.Y.)* **325**, 1790 (2010).
- [46] H. Buljan, O. Cohen, J. W. Fleischer, T. Schwartz, M. Segev, Z. H. Musslimani, N. K. Efremidis, and D. N. Christodoulides, *Phys. Rev. Lett.* **92**, 223901 (2004).
- [47] O. Cohen, H. Buljan, T. Schwartz, J. W. Fleischer, and M. Segev, *Phys. Rev. E* **73**, 015601 (2006).
- [48] F. Dalfovo, S. Giorgini, L. P. Pitaevskii, and S. Stringari, *Rev. Mod. Phys.* **71**, 463 (1999).
- [49] L. Pitaevskii and S. Stringari, *Bose-Einstein Condensation* (Clarendon Press, Oxford, 2003).
- [50] C. J. Pethick and H. Smith, *Bose-Einstein Condensation in Dilute Gases* (Cambridge University Press, Cambridge, UK, 2008).
- [51] M. D. S. Gardiner, N. Proukakis, and M. Szymanska, *Finite Temperature and Non-Equilibrium Dynamics* (Imperial College Press, London, 2013).
- [52] T. Mori, T. Kuwahara, and K. Saito, *Phys. Rev. Lett.* **116**, 120401 (2016).
- [53] T. Kuwahara, T. Mori, and K. Saito, *Ann. Phys. (N.Y.)* **367**, 96 (2016).

- [54] D. A. Abanin, W. De Roeck, W. W. Ho, and F. Huveneers, *Phys. Rev. B* **95**, 014112 (2017).
- [55] D. Abanin, W. De Roeck, W. W. Ho, and F. Huveneers, *Commun. Math. Phys.* **354**, 809 (2017).
- [56] D. Xiao, M.-C. Chang, and Q. Niu, *Rev. Mod. Phys.* **82**, 1959 (2010).
- [57] V. Debierre, I. Goessens, E. Brainis, and T. Durt, *Phys. Rev. A* **92**, 023825 (2015).
- [58] G. J. Milburn, J. Corney, E. M. Wright, and D. F. Walls, *Phys. Rev. A* **55**, 4318 (1997).
- [59] S. Raghavan, A. Smerzi, S. Fantoni, and S. R. Shenoy, *Phys. Rev. A* **59**, 620 (1999).
- [60] D. Cocks, P. P. Orth, S. Rachel, M. Buchhold, K. Le Hur, and W. Hofstetter, *Phys. Rev. Lett.* **109**, 205303 (2012).
- [61] E. Merzbacher, *Quantum Mechanics*, 3rd ed. (Wiley, New York, 1998).

Linear stability of periodic three-body orbits with zero angular momentum and topological dependence of Kepler's third law: a numerical test

V Dmitrašinović^{1,5}, Ana Hudomal², Mitsuru Shibayama³
and Ayumu Sugita⁴

¹ Institute of Physics Belgrade, University of Belgrade, Pregrevica 118, Zemun, PO Box 57, 11080 Beograd, Serbia

² Scientific Computing Laboratory, Center for the Study of Complex Systems, Institute of Physics Belgrade, University of Belgrade, Serbia

³ Department of Applied Mathematics and Physics, Graduate School of Informatics, Kyoto University, Yoshida-honmachi, Sakyo-ku, Kyoto 606-8501, Japan

⁴ Department of Applied Physics, Osaka City University, 3-3-138 Sugimoto, Sumiyoshi-ku, Osaka 558-8585, Japan

E-mail: dmitrasin@ipb.ac.rs

Received 30 January 2018, revised 18 May 2018

Accepted for publication 5 June 2018

Published 22 June 2018




CrossMark

Abstract

We test numerically the recently proposed linear relationship between the scale-invariant period $T_{s.i.} = T|E|^{3/2}$, and the topology of an orbit, on several hundred planar Newtonian periodic three-body orbits. Here T is the period of an orbit, E is its energy, so that $T_{s.i.}$ is the scale-invariant period, or, equivalently, the period at unit energy $|E| = 1$. All of these orbits have vanishing angular momentum and pass through a linear, equidistant configuration at least once. Such orbits are classified in ten algebraically well-defined sequences. Orbits in each sequence follow an approximate linear dependence of $T_{s.i.}$, albeit with slightly different slopes and intercepts. The orbit with the shortest period in its sequence is called the ‘progenitor’: six distinct orbits are the progenitors of these ten sequences. We have studied linear stability of these orbits, with the result that 21 orbits are linearly stable, which includes all of the progenitors. This is consistent with the Birkhoff–Lewis theorem, which implies existence of infinitely many periodic orbits for each stable progenitor, and in this way explains the existence and ensures infinite extension of each sequence.

⁵ Author to whom any correspondence should be addressed.

Keywords: celestial mechanics, three-body systems in Newtonian gravity, nonlinear dynamics and chaos

 Supplementary material for this article is available [online](#)

(Some figures may appear in colour only in the online journal)

1. Introduction

There is no general solution to the Newtonian three-body problem [1], so particular solutions, such as periodic orbits, are of special interest. Up until five years ago, only three topologically distinct families of periodic orbits were known [2–5], with the latest two discoveries being received with some fanfare. No theorem guaranteeing the existence of further periodic solutions was known at the time. Indeed contradictory claims [6], and counterclaims [7] in the 1950s and 1960s led to some confusion, which was (only partially) resolved by subsequent numerical discoveries—the corresponding formal existence proofs for these orbits are still being sought, and only in a few rare examples, have been supplied—for a brief history of this problem up to mid 1970’s see section 1⁶ in Broucke [8], and for subsequent developments, see section I in [9].

The questions of existence, density and distribution of *stable* orbits is of some importance for astronomy: stable orbits have at least a fighting chance of being produced in astrophysical processes and, therefore, of being subsequently observed. These questions can only be addressed by explicit discovery, or construction of new stable orbits⁷. Therefore any reliable new source of information about periodic orbits, even if it is (only) empirical and incomplete, ought to be welcomed by the community and subjected to further tests.

Several hundred demonstrably distinct families of periodic orbits have been found by numerical means over the past few years [9–14]. This progress in numerical studies has led to a new, wholly unexpected insight into the distribution of periodic orbits, that was, at first, rather tentative: soon after the papers [5, 10] appeared a relationship between an orbit’s period and its topology was observed—at first just in one class of orbits [10], and then more generally [15]. The initial set of orbits was fairly ‘sparse’, consisting of only about 45 orbits, so the observed regularities had large gulfs yet to be filled. In the meantime we have continued our search for new orbits, as well as tests of their stability, amounting to more than 200 orbits, this time with a clear indication that their number grows without bounds as the scale-invariant period increases, and still following the linear dependence of an orbit’s period on its topology [9].

Here we present a new, detailed numerical test of the previously observed regularities, based on more than 200 orbits, as well as several new regularities regarding (probably) infinite sequences of orbits. Moreover, we present a semi-empirical observation about the relation between stability of certain orbits and the existence of infinite sets of periodic orbits, as

⁶ However, the existence of periodic solutions for the general three-body problem has been considered a somewhat controversial question in the last few years. Vernić (1953) has published a detailed study containing a mathematical proof of the non-existence of periodic solutions other than the Lagrange solutions. Later it is seen that Merman (1956) and Leimanis (1958) have questioned Vernić’s non-existence proof. More recently Arenstorf (1967) has published a new existence proof for periodic solutions of the general problem, although his work contains no examples, whereas Kolenkiewicz and Carpenter have numerically computed a periodic solution with masses and configuration of the Sun–Earth–Moon system. Jefferys and Moser (1966) have also published existence proofs for almost periodic solutions in the three-dimensional case. However, the most convincing explicit examples of periodic solutions have recently been obtained numerically by Szebehely and Standish (1969), and Peters (1967). Their publications definitely settle the question of whether the general problem has non-trivial periodic solutions, although all of their examples are rather specialized; i.e. collision orbits or zero total angular momentum orbits’.

⁷ Only roughly one out of ten of the newly discovered orbits are linearly stable [9, 14].

related by the Birkhoff–Lewis theorem [16], as well as some analytic arguments about the causes of the linear relation between the period and topology, that still remain without rigorous proofs. These arguments have evolved from the study [44] of the three-body system in the so-called strong Jacobi–Poincaré potential, which system is simpler than the Newtonian one, and therefore allows certain theorems about the existence of solutions to be proven and analytical arguments to be made. The extension of these analytic arguments to the Newtonian three-body system may seem straightforward at first, but a closer inspection might prove more complicated. We have tried and pointed out lacunae in our arguments, in the hope that experts will either complete the proofs, or definitely disprove the conjectures.

If our numerical and empirical arguments withstand a more rigorous mathematical scrutiny, they should have: (1) significant implications for the distribution of periodic three-body orbits in all homogeneous potentials with singularities at the two-body collision points: at least one such potential (the Coulomb one) is of direct physical interest; and (2) ready generalizations for 4-, 5-, ... n -body periodic orbits in the Newtonian potential.

In this paper, after the present Introduction, in section 2 we provide the necessary preliminaries for our work. Then in section 3 we provide more than 200 periodic zero-angular-momentum orbits and identify their topologies using two integers, n_w and \bar{n}_w , defined in section 2. There we test their $T_{s.i.}$ versus $(n_w + \bar{n}_w)$ relationship(s) and refine the quasi-linear rule, equation (2), by classifying the new orbits into ten algebraically well-defined sequences. In section 4 we study the linear stability of three-body orbits, which leads us to the identification of six orbits as progenitors of ten sequences of orbits. There, we offer a possible explanation for the existence of infinitely many orbits in each sequence, in terms of the Birkhoff–Lewis theorem, which we do not prove in this case, however. In section 5 we offer a possible explanation of the observed linear regularities, using the virial theorem and the analyticity of the action. Finally, in section 6 we summarize and discuss our results, as well as present some open questions. Appendices A–E are devoted to various necessary technical topics, that would distract the flow of our arguments, if they were kept in the main text.

2. Preliminaries: topology and period of periodic three-body orbits

For a quantitative relationship between topology and period to be possible one has to have an algebraic method for the description of an orbit’s topology. There are several such methods in the literature, variously based on the braid group B_2 , [2], on the free group F_2 on two elements [17], and on three symbols [18], see appendices B and C.

The original discovery of the linear relationship between period and topology was based on Montgomery’s free group method [17], which was used to identify and label periodic orbits.

The topology of a periodic three-body orbit O can be algebraically described by a finite sequence of symbols, e.g. letters (a, b) and (A, B) , that we shall call ‘word’ w_O ⁸, as defined in [17], and presented in detail in [19], and briefly reviewed in appendix B. For an alternative method of assigning symbols to a topology, see appendix C.

With such an algebraic description one could, for the first time, search for relations between topological and dynamical properties of orbits. At first, the curious approximate linear functional relation

$$\frac{T_{s.i.}(w_8^k)}{T_{s.i.}(w_8)} \equiv \frac{T(w_8^k)|E(w_8^k)|^{3/2}}{T(w_8)|E(w_8)|^{3/2}} \simeq k = 1, 2, 3, \dots \quad , \quad (1)$$

⁸ More precisely, the conjugacy class of the free group element.

was noticed between the periods T , energies E and the free-group elements $w_8 = (\text{ab})(\text{AB})$ for the figure-eight orbit [3] and their topological-power satellite orbits with topologies $w^k = [(\text{ab})(\text{AB})]^k$, ($k = 1, 2, 3, \dots$). We define ‘topological-power satellite’ orbits as those whose topologies can be described as k times repeated topology, i.e. integer powers w^k of the simplest (‘progenitor’) orbit described by the word w [10]. Here \simeq means equality within the estimated numerical precision of [10]. In the meantime, with improved numerics, several cases have been found where this relation breaks down at higher decimal places.

Initially, only the ‘topological-power satellites’ of the figure-eight orbit were known⁹, but, in the meantime new examples of topological-power satellites¹⁰ have been found to obey equation (1) within their respective numerical errors. This naturally raises the question: why do only some orbits have topological-power satellites and not others? We shall argue below that the linear stability of the shortest-period (‘progenitor’) orbit plays a crucial role in this regard.

Following this observation, [15] investigated all of the 45 orbits known at the time and not just the topological-power satellites, and observed the following more general¹¹ quasi-linear relation

$$\frac{T_{\text{s.i.}}(w)}{T_{\text{s.i.}}(w_p)} \simeq \frac{N_w}{N_{w_p}} = \frac{n_w + \bar{n}_w}{n_{w_p} + \bar{n}_{w_p}} \tag{2}$$

for three-body orbits with zero angular momentum. Here $N_w = n_w + \bar{n}_w$ is one half of the minimal total number of letters¹², in the free group element $w = w(O)$ characterizing the (family of) orbit O , and similarly for $w_p = w(\text{progenitor})$, the word describing the progenitor orbit in a sequence, where n_w is the number $n_w = \frac{1}{2}(n_a + n_b)$, of small letters a, or b, and $\bar{n}_w = \frac{1}{2}(n_A + n_B)$ is the number of capital letters A, or B.

Equation (2) suggested ‘at least four and at most six’ distinct sequences among the 45 orbits considered in [15]. Precise algebraic definitions of these sequences, analogous to the definition w^k of the topological-power satellites, were not known at the time, again due to the dearth of distinct orbits¹³. This clearly demanded further, finer searches to be made.

Equation (2) predicts (infinitely) many new, as yet unobserved orbits together with their periods; if true, even approximately, equation (2) would be a spectacular new and unexpected property of three-body orbits, that would open new insights into the Newtonian three-body problem, as well as provide help in practical searches to find new orbits. Therefore equation (2) merits a thorough investigation, which we shall attempt below. The scope, of course, is limited by the number and type of available orbits.

3. Classification of orbits in sequences

Using equation (2) we predicted the periods and numbers of letters of new orbits, and then searched for them, with the results first reported in [9]. We did so by first identifying the linearly stable orbits among the original 13 orbits, and then by ‘zooming in’ our search on smaller windows around the stable orbits. Thus we found new periodic orbits that have ‘filled’

⁹ With one exception: the yarn orbit $w_{\text{yarn}} = (\text{babABabaBA})^3 = w_{\text{moth I}}^3$, where $w_{\text{moth I}} = \text{babABabaBA}$ in [5].

¹⁰ E.g. of the ‘moth I’ orbit, as well as several topological-power satellites of three other orbits, see [9, 20, 39].

¹¹ Equation (1) is manifestly a special case of equation (2).

¹² Here, by ‘minimal total number of letters’ we mean the number of letters after all pairs of adjacent identical small and capital letters, such as aA , have been eliminated, as explained in [9].

¹³ Many distinct satellite orbits’ points almost overlapped on the $T_{\text{s.i.}} - N_w$ graph, due to identical values of N_w and similar periods, which further reduced the number of distinct data points. Moreover, there were significant ‘gaps’ between the data points, as well as one ‘outlier point’ (orbit), in figure 1 in [15], that was roughly 8% off the conjectured straight line.

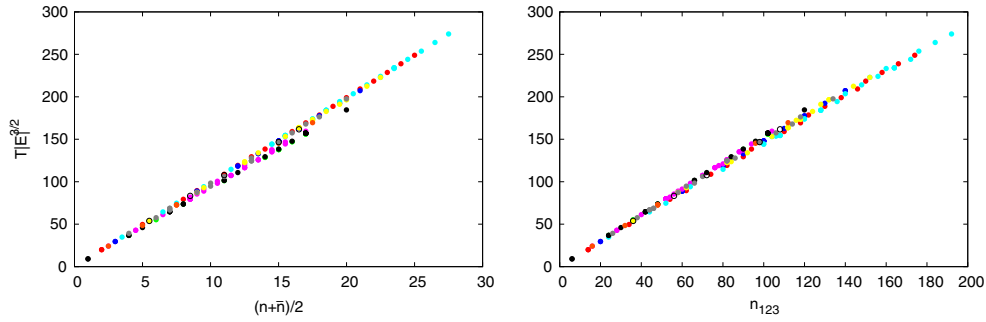


Figure 1. (a) Left panel: the scale-invariant periods $|E|^{3/2}T(w)$ of more than 200 presently known zero-angular-momentum three-body orbits versus one half of the number of all letters in the free-group word w describing the orbit, $N_w = n_w + \bar{n}_w$, where n_w is the number of small letters a, or b, and \bar{n}_w is the number of capital letters A, or B in the word w . (b) Right panel: same as (a), only in terms of the number of symbols n_{123} in the sequence of symbols (1,2,3) describing the topology of the orbit, see appendix C. Color code: (1) red = sequence I—butterfly I; (2) green = sequence II—dragonfly; (3) dark blue = sequence III—yin-yang; (4) pink = sequence IVa—moth I; (5) light blue = sequence IVb—butterfly III; (6) yellow = sequence IVc—moth III; (7) black = sequence V—figure-eight; (8) orange = sequence VI—yarn; (9) grey = sequence VII—moth; (10) empty circles = other.

Table 1. Typical (non-minimal) free group elements’ w structure for orbits in various sequences, their progenitors, the line parameters c_1, c_2 , where the $T_{s.i.}(N_w)$ dependence is fitted as $f(x) = c_1x + c_2$. Not all words $w(n_i)$ in any particular sequence need have the presented structure, however, see supplementary notes.

Sequence number and name	Free group element $w(n)$	progenitor	c_1	c_2
I butterfly I (n, n)	$(AB)^2(abaBAB)^n(ab)^2(ABAbab)^n$	Schubart	9.957 ± 0.011	-0.2 ± 0.2
II dragonfly (n, n)	$bA(baBA)^n aB(abAB)^n$	isosceles	9.194 ± 0.004	0.04 ± 0.06
III yin-yang (n, n)	$(abaBAB)^n a(babABA)^n A$	S-orbit	9.8667 ± 0.0003	0.002 ± 0.004
IVa moth I $(n, n + 1)$	$(abAB)^n A(baBA)^n B$	moth I	9.34 ± 0.06	0.7 ± 0.7
IVb butterfly III $(n, n + 1)$	$[(ab)^2(AB)^2]^n b[(ba)^2(BA)^2]^n a$	butterfly III	9.967 ± 0.012	-0.3 ± 0.3
IVc moth III $(n, n + 1)$	$(babABA)^n A(abaBAB)^n B$	Schubart	9.94 ± 0.04	-1.2 ± 0.7
V figure-eight (n, n)	$(abAB)^n$	figure-8	9.2377 ± 0.0014	-0.03 ± 0.02
VI moth I—yarn $(2n, 3n)$	$[(abAB)A(baBA)B]^n$	moth I	9.683 ± 0.002	0.01 ± 0.02
VIIa moth (n, n)	$(abAB)^{(n+1)} a(baBA)^n b$	Schubart	9.61 ± 0.07	-0.2 ± 0.7
VIIb moth (n, n)	$(abaBAB)^{(n+1)} b(babABA)^n a$	Schubart	9.88 ± 0.04	-0.7 ± 0.5

many of the ‘gaps’ in the older versions of the $T_{s.i.} - N_w$ graph, see figure 1(a), the website [20] and the supplementary notes (stacks.iop.org/JPhysA/51/315101/mmedia). The ‘outlier’ point, in figure 1 in [15], has become just another orbit in a new sequence with a slightly steeper slope on the same graph. The totality of the $T_{s.i.} - N_w$ points is shown in figure 1.

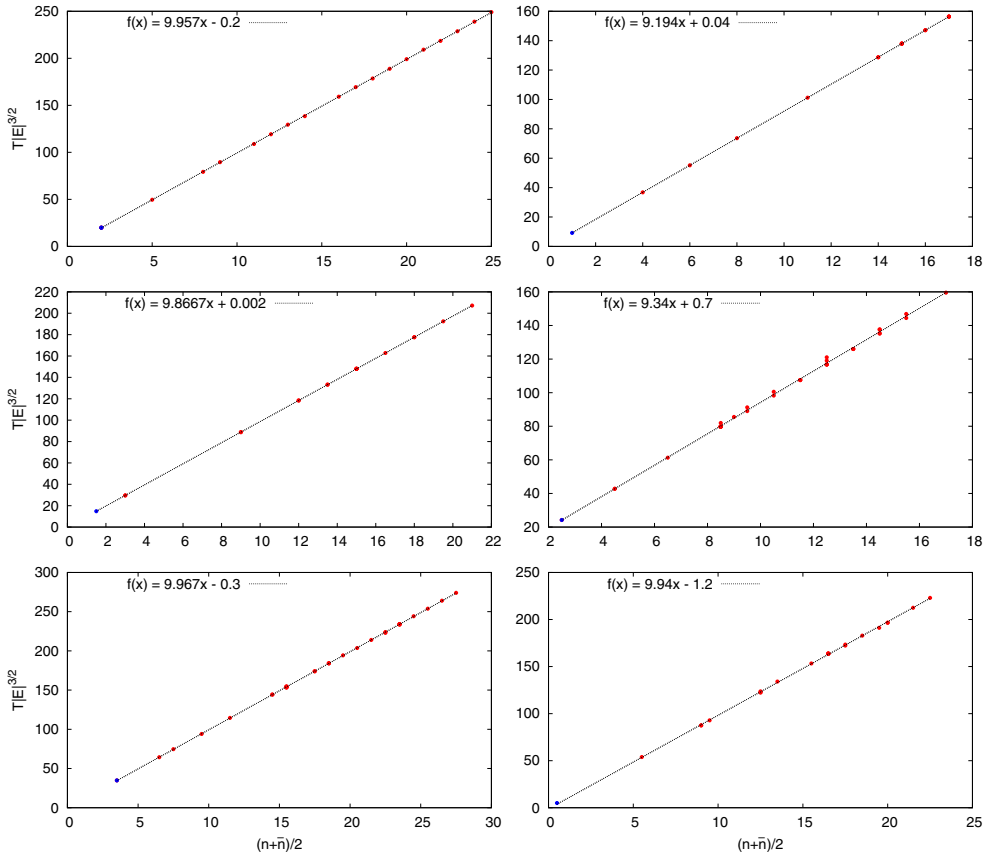


Figure 2. The scale-invariant periods $|E|^{3/2}T(w)$ of zero-angular-momentum three-body orbits versus one half of the number of all letters in the free-group word w describing the orbit, $N_w = n_w + \bar{n}_w$, where n_w is defined as in figure 1. (a) Top left: sequence I—butterfly I, ; (b) top right: sequence II—dragonfly; (c) center left: sequence III—yinyang; (d) center right: sequence IVa—moth I; (e) bottom left: sequence IVb—butterfly III; (f) bottom right: sequence IVc—moth III. The blue points at the lower ends of sequences are the progenitors of the respective sequences, see the text. Progenitors of sequences II, III and IVc, that involve collisions were not used in the fitting procedure, so the validity of the linear Ansatz for these sequences can be evaluated by inspection.

It is clear that the scale-invariant periods $T_{s.i.}$ do not lie on one straight line, but rather on several lines with slightly different slopes, emerging from a small ‘vertex’ area, forming a (thin) wedge-like structure in figure 1. All the newly found orbits passing through an Euler configuration, see supplementary notes, fit into one of ten sequences, where the fourth (‘moth I’) sequence in [15] has now been divided into three: (a) ‘moth I ($n, n + 1$)’; (b) ‘butterfly III–IV ($n, n + 1$)’; (c) ‘moth III ($n, n + 1$)’. Moreover, we found two entirely new sequences: (1) ‘VIIa moth (n, n)’ and (2) ‘VIIb moth (n, n)’, and one sequence of pure ‘topological-power satellites’ of the moth I orbit.

Each of these ten sequences has an algebraic pattern of free-group elements, see table 1, associated with it. Here we use the sequence label (n, m) to denote the general form of (n_w, \bar{n}_w) in that sequence: for example (n, n) means that n_w and \bar{n}_w are equal integers: $n = n_w = \bar{n}_w = 1, 2, 3, \dots$. Then, n can be used to label orbits within the sequence, see supplementary notes. By setting $n = 0$, or $n = 1$, in the second column of table 1, in each sequence,

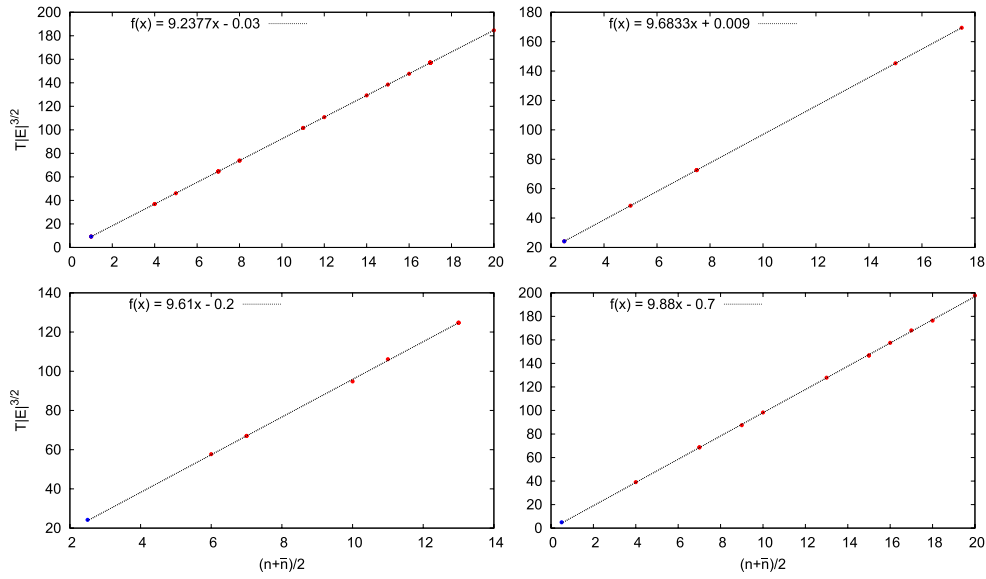


Figure 3. Same as in figure 2, except for the following sequences: (a) top left: sequence V—figure-eight; (b) top right: sequence VI—yarn; (c) bottom left: sequence VIIa—moth III (n, n); (d) bottom right: sequence VIIb—moth III (n, n). The progenitors of sequence VIIa and VIIb were not used in the fitting procedure.

we can read off the topology of their respective progenitor, which is shown in the third column of table 1.

The individual $T_{s.i.} - N_w$ graphs are shown in figures 2 and 3, and their free-group patterns are in table 1. The agreement of separate sequences with the linear functional Ansatz, equation (2), see figures 1(b)–(d), is much better than for the aggregate of all orbits, Figure 1, but the (root-mean-square) variations of line parameters (c_1, c_2) reported in table 1 are generally larger than the estimates numerical errors, thus indicating that equation (2) is still *approximate*, and *not exact*, even in these sequences.

Whereas the approximate empirical rule equation (2) now appears established, and its extension to ever-longer periods just a technical difficulty, some deeper questions remain open. For example, the *raison d’être* of so many periodic orbits remains obscure, let alone the linear relation among their periods.

4. Linear stability and progenitor orbits

Perhaps the first hint at a solution to this puzzle was given in [39], where it was noticed that the topological satellite orbits in the Broucke–Hadjidemetriou–Hénon (BHH), [8, 35, 36, 40–43], family of orbits with non-zero angular momentum, exist only when their progenitor is linearly stable. There is a theorem, due to Birkhoff and Lewis [16], see also section 3.3 (by Jürgen Moser) in [25], which holds for systems with three degrees-of-freedom and implies the existence of infinitely many periodic orbits¹⁴. So, whereas the Birkhoff–Lewis theorem might solve

¹⁴ In [12], it was conjectured that the topological-power satellites of the figure-eight orbit are a consequence of the Poincaré–Birkhoff theorem [22], see also section 24 in [23] and section 2.7 in [24], as applied to the figure-eight orbit. That conjecture is incorrect, however, because the Poincaré–Birkhoff theorem applies only to systems with two degrees-of-freedom, to which class the planar three-body problem does not belong.

Table 2. The Floquet exponents ν_j , where $\lambda_j = \exp(\pm 2\pi i \nu_j)$ define the linear stability coefficients of linearly stable periodic three-body orbits.

Label	ν_1	ν_2
S-orbit	0.131 093	0.470 591
Moore 8	0.298 093	0.00 842 275
NC1 (8^7)	0.27 216	0.158 544
V.17.H (O13 = 8^{17})	0.31 573	0.0002 988
V.17.I (O14 = 8^{17})	0.0435 411	0.00 262 681
V.17.J (O15 = 8^{17})	0.0435 411	0.00 262 681
II.11.A (bumblebee)	0.1371 49	0.0325 135
IVa.2.A (moth I)	0.1590 13	0.491 881
IVa.4.A (moth II)	0.108 451	0.0886 311
IVb.3.A (butterfly III)	0.378 728	0.00 173 642
I.5.A	0.170 764	0.001 476
I.14.A	0.443 006	0.000 121 435
II.17.B	0.138 698	0.0335 924
III.13.A. β	0.175 816	0.000 655 417
IVb.9.A	0.194 186	0.000 561 819
IVc.12.B	0.0863 933	0.00 394 124
IVc.17.A	0.0442 047	0.00 206 416
VIIa.11.A	0.416 228	0.0088 735
VIIb.7.A	0.27 753	0.0360 425
VIIb.9.A	0.216 455	0.0584 561
VIIb.13.A	0.0621 421	0.0141 894

one part of the puzzle, it does not say anything about the relation of topologies and periods. There is, however, another (the so-called ‘twist’) condition underlying this theorem, which we shall not try to check here—we simply conjecture that the Birkhoff–Lewis theorem holds for the linearly stable periodic three-body orbits. Linear stability of periodic orbits is tested numerically, see below, and thus the conjecture of Birkhoff–Lewis theorem can be falsified.

We have analyzed linear stability of all zero-angular-momentum three-body orbits and tabulated the linearly stable ones in table 2. The Floquet exponents ν_j , and the linear stability coefficients $\lambda_j = \exp(\pm 2\pi i \nu_j)$, are the standard ones, as defined in [9]. We note that two orbits, ‘butterfly III’ and ‘moth I’, lie at the origins of two ‘linear sequences¹⁵’ of ‘non-topological-power satellite’ orbits observed among the original 13 orbits [15].

Thus, the manifest candidates for progenitors are: (1) ‘figure-eight’ for the sequence V ‘figure-eight (n, n)’; (2) ‘butterfly III’ for the sequence IVb ‘butterfly III ($n, n + 1$)’; and (3) ‘moth I’ for the sequences IVa ‘moth I ($n, n + 1$)’ and VI ‘moth I—yarn ($2n, 3n$)’. These three progenitors are collisionless orbits with three degrees-of-freedom, that are linearly stable.

Next we extend this reasoning to sequences of periodic three-body orbits with collisional progenitors.

- (1) The parent orbit of sequence II ‘dragonfly (n, n)’ is Broucke’s isosceles triangle orbit [37, 38], that involves two-body collisions. This orbit always stays in an isosceles triangle configuration, thus eliminating one degree-of-freedom, and is linearly stable [37, 38], so it also satisfies the Poincaré–Birkhoff theorem.
- (2) The parent orbit of the ‘yin-yang’ sequence is the collisional ‘S-orbit’ of [4, 11]¹⁶.

¹⁵ The orbits ‘moth I’ and ‘moth II’ have different topologies, but belong to the same sequence.

¹⁶ See the initial condition #20 in table I in [11].

- (3) The Schubart orbit [34] is the progenitor of four sequences: I, IVc, VIIa and VIIb, see table 1 and supplementary notes. The Schubart orbit is linearly stable in three spatial dimensions, [35, 36], but due to its collinear nature, it has only two degrees-of-freedom. As it has two degrees-of-freedom, it satisfies the Poincaré–Birkhoff theorem [22–24], which also predicts the existence of infinitely many orbits¹⁷.

Thus, we have shown a definite correlation between the sequences in table 1 and linear stability of the progenitor orbit in each sequence.

5. Virial theorem and analyticity of the action

The remaining mysteries are: (i) why are the $T_{s.i.}(N_w)$ graphs linear, and (ii) why are the slopes of different sequences so close to each other?

Our answers to these questions are still not proven in a sufficiently rigorous way. Therefore, we shall present them here in the same, or similar way, as they were discovered; otherwise the motivation, and the weak points of our arguments might be lost.

It should be clear that the mere formulation of $T_{s.i.} = T|E|^{3/2}$ depends crucially on the homogeneity of the Newtonian potential: the exponent 3/2 follows from the Newtonian potential's degree of homogeneity $\alpha = 1$, see [15, 19]. So, one may ask if the same, or similar behaviour occurs in other homogeneous potentials? A (partial) answer to this question was provided in [44], where periodic three-body orbits in the so-called strong potential $V^{\alpha=2}(r) \simeq -1/r^2$ and their relation to topology were studied, which has led to our proposed answer to question (i). The strong potential $V^{\alpha=2}(r) \simeq -1/r^2$, is also homogeneous, see appendix D.

It was shown in [44] that the periodic solutions to the three-body problem in the strong potential form sequences, very much like those in the Newtonian potential shown in section 3, but their periods do *not* increase linearly with the topological complexity N_w of the orbit. Rather, it is the action integral, $S_{\min} \simeq N_w$, that rises linearly with N_w , which fact can be understood using Cauchy's residue theorem, which is based on the analyticity of the action integral,

$$S_{\min}^{\alpha=2} = -2 \int_0^T V^{\alpha=2}(\mathbf{r}(t)) dt,$$

where $\mathbf{r}(t)$ is a periodic solution to the equations-of-motion (e.o.m.) at fixed energy $E = 0$, see appendix E.

But, in the Newtonian potential the action of (any) periodic orbit is proportional to its period $S_{\min}^{\alpha=1}(T) = 3|E|T$, see equation (D.5), derived in appendix D.2. So, the scale-invariant period $T_{s.i.}$ must depend in the same way on the topological complexity N_w of the orbit as the corresponding action $S_{\min}^{\alpha=1}(T)$. The question now arises if the same argument as in [44], about the analyticity of the action $S_{\min}^{\alpha=1}(T)$ can be extended to the Newtonian potential?

In the Newtonian potential this argument becomes more complicated because the hyper-radius $R = |Z|$ is not constant in Newtonian three-body orbits, and the problem becomes one in the calculus of two complex variables, see appendices A and E. This leads to new possibilities that have not been considered thus far. Indeed, the second complex variable in the Newtonian potential immediately leads to the possibility that there is a pole in the second complex variable Z , which could lead to non-zero contributions to the integral, and thus change the $T_{s.i.}(N_w)$ functional dependence, under right conditions.

Assuming that the variation of periodic orbits in the second complex variable Z is limited such that no new poles arise in the action integral, see appendix E, we may conclude that

¹⁷ We see that one colliding orbit is the progenitor of more than one sequence of collisionless orbits.

$$S_{\min}^{\alpha} = \left(\frac{\alpha + 2}{\alpha - 2} \right) E T \simeq N_w.$$

This cannot be true in general, however: a moment's thought shows that the linear dependence cannot hold in the harmonic oscillator, as all harmonic oscillatory motions have the same period there. More formally, equation $S_{\min}^{\alpha} = \left(\frac{\alpha+2}{\alpha-2} \right) E T$, implies that the action of a periodic orbit in the harmonic oscillator always vanishes $S_{\min}^{\alpha=-2} = 0$. Moreover, we note that the action integral equation (D.4) must have (at least one) pole if the residue theorem should hold. Consequently, there is an upper bound on the exponent: $\alpha \geq 0$, for which this kind of action-topology dependence can exist.

These arguments provide also a (possible) answer to question (ii) above, as the slope of of the $T_{s.i.}(N_w)$ graph depends on the residue(s) at the same poles in all sequences, the main difference being the ordering of circles around the poles, i.e. of the Riemann sheet(s) one is on ('crossings of branch cuts'), see appendix E.

Of course, the foregoing arguments do not constitute a mathematical proof—the missing dots on the i's and crosses on the t's, or, perhaps more interestingly, counter-arguments/proofs—ought to be supplied by the interested reader.

6. Summary, discussion and outlook

We have shown that:

- (1) The presently known periodic three-body orbits with vanishing angular momentum and passing through an Euler configuration, can be classified into 10 sequences according to their topologies. Each sequence probably extends to infinitely long periods, and emerges from one of six linearly stable (shortest-period) progenitor orbits.
- (2) Numerically, the scale-invariant periods of orbits in each sequence obey linear dependences on the number of symbols in the algebraic description of the orbit's topology.
- (3) There is a possible explanation for the existence of this infinity of periodic orbits, in the form of Birkhoff–Lewis theorem, provided that each progenitor orbit also satisfies the 'twist' condition [16].
- (4) Some of the longer-period orbits are linearly stable: (a) the seventh satellite of 'figure-eight' orbit¹⁸; (b) moth II, which lies in, but is not the progenitor of the 'moth I' sequence; and (c) the 'bumblebee' orbit, which lies in, but is not the progenitor of the 'dragonfly' sequence.

We note that in 1976 [35], Hénon established the linear stability of many orbits with non-vanishing angular momenta ($L \neq 0$) in the Broucke–Hadjidemetriou–Hénon family. The topological-power satellites of these linearly stable BHH orbits were discovered only recently [39], where an $L \neq 0$ version of the period-topology linear dependence equation (2) was checked numerically, as well. The agreement there is also (only) approximate, as a small, but numerically significant discrepancy exists.

Furthermore, [44] indicates that a linear dependence of the action, but not of the period, on the topology exists also in the case of periodic three-body orbits in the so-called strong Jacobi–Poincaré potential, which is in agreement with the virial theorem, see appendix D. The argument in [44] can be extended to the Newtonian potential, but it becomes a complicated question in the calculus of two complex variables¹⁹.

¹⁸ The stability of 'figure-eight' orbit was established in [32, 33].

¹⁹ Indeed, the second complex variable in the Newtonian potential immediately leads to new possibilities: there is a pole in the second variable, which could lead to non-zero contributions, and thus change the $T_{s.i.}(N_w)$ function, under right conditions.

Our results are generic, so they imply that similar linear relations may be expected to hold for 3-body orbits in the Coulombian²⁰, and in all other homogeneous potentials containing poles.

Moreover, similar functional dependences might also hold for 4-, 5-, 6-body etc orbits in the Newtonian potential.

Our results also raise new questions:

- (1) Each of the six progenitors generates a family of orbits, at different masses and non-vanishing angular momenta, e.g. the Schubart colliding orbit [34], generates the BHH family of collisionless orbits with non-zero angular momenta, that describe the majority of presently known triple-star systems. The remaining five progenitors may now be viewed as credible candidates for astronomically observable three-body orbits, provided that their stability persists under changes of mass ratios and of the angular momentum. Those dependences need to be explored in detail.
- (2) Checking the ‘twist’ condition of the Birkhoff–Lewis theorem, for each progenitor orbit, is a task for mathematicians, as is the explanation of the topologies of the so-predicted orbits: why do these sequences exist and not some others?
- (3) The question of existence of other stable two-dimensional colliding orbits, and of new sequences of periodic orbits that they (may) generate. Rose’s new linearly stable colliding orbits [13] are particularly interesting in this regard. Turning the foregoing argument around, one can use any newly observed sequence of orbits to argue for the the existence of its, perhaps as yet unknown, progenitor.
- (4) A remaining mystery is why are the slopes of different sequences so close to each other?

Acknowledgments

VD and AH thank Aleksandar Bojarov, Marija Janković and Srdjan Marjanović, for their help with setting up the website, running the codes on the Zefram cluster and general programming. VD was financially supported by the Ministry of Education, Science, and Technological Development of the Republic of Serbia under Grants No. OI 171037 and III 41011 and MS was supported by the Japan Society for the Promotion of Science (JSPS), Grant-in-Aid for Young Scientists (B) No. 26800059. AH was financially supported by the Ministry of Education, Science, and Technological Development of the Republic of Serbia under project ON171017, and was a recipient of the ‘Dositeja’ stipend for the year 2014/2015, from the Fund for Young Talents (Fond za mlade talente—stipendija ‘Dositeja’) of the Serbian Ministry for Youth and Sport. The computing cluster Zefram (zefram.ipb.ac.rs) at the Institute of Physics Belgrade has been extensively used for numerical calculations.

Appendix A. Three-body variables

The graphical representation of the three-body system can be simplified with the use of translational and rotational invariance—by changing the coordinates to the Jacobi ones [30]. Jacobi or relative coordinates are defined by two relative coordinate vectors, see figure A1:

²⁰ Several such periodic orbits have been found in [45, 46], but their topological classification was not considered.

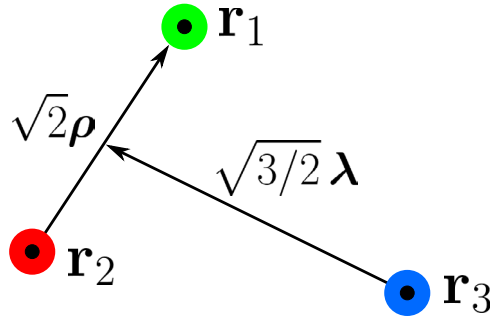


Figure A1. The two three-body Jacobi coordinates ρ, λ .

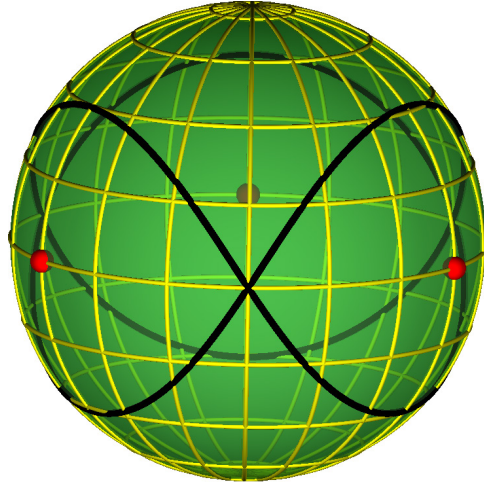


Figure A2. The shape-space sphere: the figure-eight orbit (solid black curve); three two-body collision points (red), singularities of the potential, lie on the equator.

$$\rho = \frac{1}{\sqrt{2}}(\mathbf{r}_1 - \mathbf{r}_2), \quad \lambda = \frac{1}{\sqrt{6}}(\mathbf{r}_1 + \mathbf{r}_2 - 2\mathbf{r}_3). \quad (\text{A.1})$$

Three independent scalar variables can be constructed from Jacobi coordinates: ρ^2 , λ^2 and $\rho \cdot \lambda$. The overall size of the orbit is characterized by the hyperradius $R = \sqrt{\rho^2 + \lambda^2}$. These scalar variables are connected to the unit vector with Cartesian components [17]:

$$\hat{\mathbf{n}} = \left(\frac{2\rho \cdot \lambda}{R^2}, \frac{\lambda^2 - \rho^2}{R^2}, \frac{2(\rho \times \lambda) \cdot \mathbf{e}_z}{R^2} \right). \quad (\text{A.2})$$

Therefore, every configuration of three bodies (shape of the triangle formed by them, independent of size) can be represented by a point on a unit sphere. This sphere is called the shape-sphere.

Every relatively periodic orbit of a three-body system is therefore represented on the shape-sphere by a closed curve (collisionless solutions), a finite open section of a curve (free-fall and colliding solutions), or a point (Lagrange–Euler solutions). One example, the figure-eight orbit, is illustrated in figure A2.

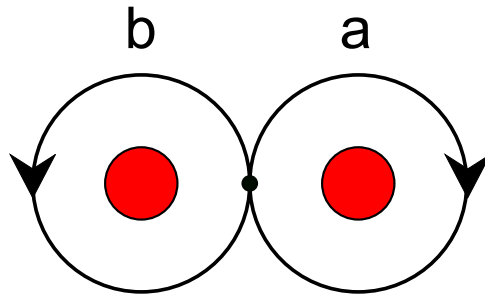


Figure B1. The two elements (a, b) of the free group.

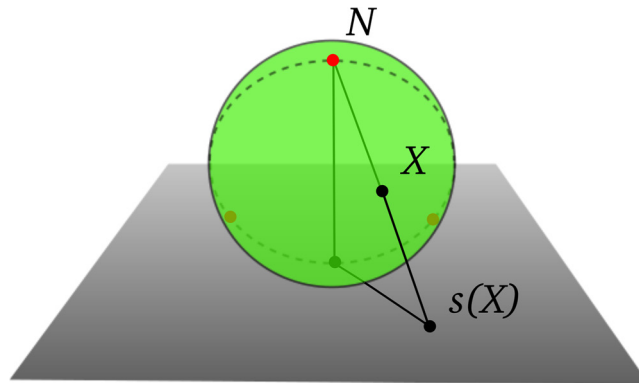


Figure B2. Stereographic projection of a sphere onto a plane. Three two-body collision points (solid red) lie on a meridian (dashed circle), with one of them being at the north pole (denoted by the letter N).

The north and the south pole of the shape-sphere correspond to equilateral triangles, while the equator corresponds to degenerate triangles, where the bodies are in collinear configurations (syzygies). There are three points on the equator that correspond to two-body collision points—the singularities of the potential, see figure A2.

Two orbits with identical representations on the shape-sphere are considered to be the same solution. For example, periodic orbits subjected to symmetry transformations, such as translations, rotations, dilations, reflections of space and time, all have identical curves on the shape-sphere and are counted as one.

Size or energy scaling, $\mathbf{r} \rightarrow \alpha \mathbf{r}$, and the equations of motion imply $t \rightarrow \alpha^{3/2} t$ [31]. Therefore, the velocity scales as $\mathbf{v} \rightarrow \mathbf{v}/\sqrt{\alpha}$, the total energy scales as $E \rightarrow \alpha^{-1} E$, and the period T as $T \rightarrow \alpha^{3/2} T$. Consequently, the combination $|E|^{3/2} T$ is invariant under scale transformations and we call it scale invariant period $T_{\text{s.i.}} = |E|^{3/2} T$. It is always possible to remove one of the three scalar variables by changing the hyper-radius to the desired value by means of these scaling rules.

Appendix B. Montgomery’s topological identification method

A curve corresponding to a collisionless periodic orbit can not pass through any one of the three two-body collision points. Stretching this curve across a collision point would therefore change its topology. The classification problem of closed curves on a sphere with three

punctures is given by the conjugacy classes of the fundamental group, which is in this case the free group on two letters (a, b), see figure B1.

This abstract notation has a simple geometric interpretation: it classifies closed curves in a plane with two punctures according to their topologies. The shape sphere can be mapped onto a plane by a stereographic projection using one of the punctures as the north pole, see figure B2. The selected puncture is thusly removed to infinity, which leaves two punctures in the (finite) plane. Any closed curve on the shape sphere (corresponding to a periodic orbit) can now be classified according to the topology of its projection in the plane with two punctures. Topology of a curve can be algebraically described by a ‘word’—a sequence of letters a, b, A and B —which is, more formally, an element of the free group F_2 . Here a denotes a clockwise full turn around the right-hand-side puncture, b the counter-clockwise full turn around the left-hand-side puncture (see figure B1), and the upper case letters denote their inverse elements $a^{-1} = A$ and $b^{-1} = B$.

A specific periodic orbit can be equally well described by several different sequences of letters. As there is no preferred starting point of a closed curve, any other word that can be obtained by a cyclic permutation of the letters in the original word represents the same curve.

The conjugacy class of a free group element (word) contains all cyclical permutations of the letters in the original word. For example, the conjugacy class of the free group element aB also contains the cyclically permuted word Ba . The class of topologically equivalent periodic orbits therefore corresponds not merely to one specific free group element, but to the whole conjugacy class.

Time-reversed orbits are represented by the inverse elements of the original free group elements. Naturally, they correspond to physically identical solutions, but they generally form different words (free group elements) with different conjugacy classes.

Another ambiguity is related to the choice of the puncture to be used as the north pole of the stereographic projection (of the sphere onto the plane). A single loop around any one of the three punctures on the original shape sphere (denoted by a or b) must be equivalent to the loop around either of the two remaining punctures. But as can be seen in figure B2, a simple loop around the third (‘infinite’) puncture on the shape sphere corresponds to aB , a loop around both poles in the plane. Therefore, aB must be equivalent to a and b .

Some periodic solutions have free group elements that can be written as $w^k = w^k(a, b, A, B)$, where $w = w(a, b, A, B)$ is a word that describes some solution, and k is an integer. Such orbits will be called topological-power satellites. For example, the orbits with free group element $(abAB)^k$ are called figure-eight (k) satellites, and are all free from the stereographic projection ambiguity.

Appendix C. Tanikawa and Mikkola’s (syzygy) method of topological identification

There is an alternative method of assigning a sequence of three symbols, in this case three digits (1,2,3), to any given ‘word’ in the free group F_2 . It has been proposed for collisionless orbits, by [18], see also [21], to use the sequence of syzygies (collinear configurations) as a symbolic dynamics for the 3-body problem.

The rules for converting ‘words’ consisting of letters a, b, A, B into ‘numbers’ consisting of three digits—(1, 2, 3)—are as follows: (i) make the substitution $a = 12, A = 21, b = 32, B = 23$; (ii) $11 = 22 = 33 =$ empty sequence (‘cancellation in pairs rule’). So, for example:

- (1) The symbolic sequence corresponding to the BHH family of orbits, $aB = 1223 = 13$ is equivalent, by way of cyclic permutations, to: $a = 12$ and to $B = 23$, as one would expect intuitively. Thus we see that the ‘lengths’ N_n , i.e. the number of symbols in a sequence are identical for all three symbolic sequences representing the BHH family, $N_n(13) = N_n(12) = N_n(23)$, unlike the Montgomery’s method, where $N_w(aB) \neq N_w(a) = N_w(B)$. This indicates that the ‘lengths’ $N_n(w)$ are good algebraic descriptors of the complexity of an orbit’s topology.
- (2) The symbolic sequence $abAB = (12) (32) (21) (23) = 12322123 = 123123 = (123)^2$ corresponding to the figure-eight orbit is now manifestly invariant under cyclic permutations, $1 \rightarrow 2 \rightarrow 3$ and $1 \rightarrow 3 \rightarrow 2$, whereas it is so only in a non-manifest way in the two-letter scheme. Here, also, the ‘length’ $N_n(w)$ is also a good algebraic descriptor of the complexity of an orbit’s topology.

Note that:

1. As stated above, the numbers 1, 2, and 3 can be viewed as denoting syzygies, i.e. crossings of the equator on the shape sphere, in one of three corresponding segments on the said equator, where the index of the body passing between the other two is used as a symbol.
2. Each symbol is its own inverse, which accounts for the ‘cancellation in pairs’ rule²¹. This circumstance leads to the reduction (by a factor of two) of the number of symbolic sequences denoting one topology, as the time-reversed orbit has an identical symbolic sequence to the original one (which is not the case in the two-letter scheme); and
3. That the cyclic permutation symmetry indicates irrelevance of which syzygy is denoted by which digit.

In this way, we have restored the three-body permutation symmetry of the problem into the algebraic notation describing the topology of a periodic three-body orbit, albeit at the price of having three symbols, rather than two. This restoration of permutation symmetry also implies an absence of the ‘automorphism ambiguity’ [15]. Such three-symbol sequences have been used e.g. in [18, 21] to identify the topology of periodic three-body orbits.

The length of a sequence of symbols necessary to describe any given topology generally increases by a factor close to 1.5 as one switches from two letters N_w to three digits N_s , as symbols used, i.e. $N_s \simeq 1.5N_w$. The precise value of this proportionality factor ($\simeq 1.5$) is not important for our purposes, as we shall be concerned with the length(s) of symbolic sequences with a well-defined algebraic form, such as $w_1(w_2)^n w_3(w_4)^n$, where $n = 1, 2, 3, \dots$. In such a case, the following relation holds $N[w_1(w_2)^n w_3(w_4)^n] \simeq N[w_1 w_3] + nN[w_2 w_4]$ using either set of symbols for w_i . Only the value of the slope parameter changes as one switches from one set to another. Of course, it is an additional mystery if and when the slopes of different sequences happen to coincide.

Appendix D. Virial theorem and the action of periodic orbits in homogeneous potentials

D.1. The Lagrange–Jacobi identity and the virial theorem

We know that the Lagrange–Jacobi identity [30],

²¹ This is only possible for periodic orbits that form closed loops on the shape sphere; otherwise one would have to define one symbol for crossing the equator from above and another one for crossing from below.

$$\frac{1}{2} \frac{dG}{dt} = 2K_{\text{total}} + \alpha V_{\text{total}}^{\alpha}, \quad (\text{D.1})$$

where $G = \sum_{i=1}^N \mathbf{q}_i \cdot \mathbf{p}_i$ is the so-called virial, gives a relation between kinetic $K_{\text{total}} = \sum_i K_i$ and potential energy $V_{\text{total}}^{\alpha}$, for homogeneous potentials with homogeneity degree $-\alpha$. One example of such a homogeneous potential is the sum of two-body terms $\sum_{i<j} V_{\alpha}(r_{ik})$, where $V_{\alpha}(r_{ik}) \simeq -1/r_{ik}^{\alpha}$ is a power-law interaction. Here r_{ik} is the distance between two particles, and α is a positive real number.

For periodic motions, with period T , this identity can be integrated to yield

$$\begin{aligned} \frac{1}{2} \int_0^T dt \frac{dG}{dt} &= \frac{1}{2} (G(T) - G(0)) = 0 \\ &= \int_0^T (2K_{\text{total}} + \alpha V_{\text{total}}^{\alpha}) dt \end{aligned} \quad (\text{D.2})$$

which tells us that the time integral of the kinetic energy is related to the time integral of the potential energy:

$$\int_0^T dt K_{\text{total}} = -\frac{\alpha}{2} \int_0^T dt V_{\text{total}}^{\alpha}.$$

Energy conservation

$$E = K_{\text{total}} + V_{\text{total}}^{\alpha}$$

implies

$$E = \frac{1}{T} \int_0^T (K_{\text{total}} + V_{\text{total}}^{\alpha}) dt = \frac{1}{T} \int_0^T \left(-\frac{\alpha}{2} V_{\text{total}}^{\alpha} + V_{\text{total}}^{\alpha}\right) dt$$

which leads to the equipartition of energy (or ‘virial’) theorem:

$$E = \left(\frac{\alpha-2}{-2}\right) \frac{1}{T} \int_0^T V^{\alpha}(r(t)) dt \equiv \left(\frac{\alpha-2}{-2}\right) \langle V^{\alpha}(r) \rangle \quad (\text{D.3})$$

$$E = \left(\frac{\alpha-2}{\alpha}\right) \frac{1}{T} \int_0^T K(\dot{r}(t)) dt \equiv \left(\frac{\alpha-2}{\alpha}\right) \langle K(\dot{r}(t)) \rangle \quad (\text{D.4})$$

which holds exactly for periodic orbits. This, in turn, reduces the action S to one or another time integral.

D.2. The action for three-body orbits in a homogeneous potential

The (minimized) action of a periodic n -body orbit in a homogeneous potential $V^{\alpha}(r) \simeq -1/r^{\alpha}$ is

$$S_{\text{min}} = \int_0^T L(q(t), \dot{q}(t)) dt = \int_0^T (T(\dot{r}(t)) - V^{\alpha}(r(t))) dt,$$

leads to

$$S_{\text{min}}^{\alpha}(T) = \left(\frac{\alpha+2}{\alpha-2}\right) E T, \quad (\text{D.5})$$

which depends only on the energy E and period T of the orbit. Note the singularity on the right-hand-side of equation (D.5) at $\alpha = 2$, which demands that $E = 0$ in that case. For the Newtonian case, $\alpha = 1$, equation (D.5) leads to

$$S_{\min}^{\alpha=1}(T) = -3ET = 3|E|T,$$

as claimed in [15].

Appendix E. Complex variables and analytic properties of the action

Here we follow closely appendix C in [44]. The minimized action $S_{\min}^{\alpha} = \int_0^T L(q(t), \dot{q}(t)) dt$ of a periodic orbit $q(t)$ in the homogeneous (power) potential $V^{\alpha}(r)$, written as a time integral of twice the kinetic energy K over period T ,

$$S_{\min}^{\alpha}(T) = \left(\frac{\alpha+2}{\alpha}\right) \sum_{i=1}^3 \int_0^T \frac{\mathbf{p}_i^2}{2m} dt = \left(\frac{\alpha+2}{\alpha}\right) \sum_{i=1}^3 \int_{\mathbf{r}_i(0)}^{\mathbf{r}_i(T)} \mathbf{p}_i \cdot d\mathbf{r}_i \quad (\text{E.1})$$

where $m = 1$, can be expressed as a closed-contour integral of two complex variables. After shifting to the relative-motion variables, $(\boldsymbol{\rho}, \boldsymbol{\lambda})$, one finds

$$S_{\min}^{\alpha}(T) = \left(\frac{\alpha+2}{\alpha}\right) \left(\int_{\boldsymbol{\rho}(0)}^{\boldsymbol{\rho}(T)} \mathbf{p}_{\boldsymbol{\rho}} \cdot d\boldsymbol{\rho} + \int_{\boldsymbol{\lambda}(0)}^{\boldsymbol{\lambda}(T)} \mathbf{p}_{\boldsymbol{\lambda}} \cdot d\boldsymbol{\lambda} \right).$$

The real Jacobi two-vectors $\boldsymbol{\rho}$ and $\boldsymbol{\lambda}$ may be replaced with two complex variables

$$z_{\rho} = \rho_x + i\rho_y, \quad z_{\lambda} = \lambda_x + i\lambda_y,$$

so that the action S_{\min}^{α} , can be rewritten as a (double) closed contour integral in two complex variables:

$$S_{\min}^{\alpha}(T) = \left(\frac{\alpha+2}{\alpha}\right) \left(\int_{z_{\rho}(0)}^{z_{\rho}(T)} \dot{z}_{\rho}^* dz_{\rho} + \int_{z_{\lambda}(0)}^{z_{\lambda}(T)} \dot{z}_{\lambda}^* dz_{\lambda} \right).$$

Note that the periodicity of motion $\boldsymbol{\rho}(0) = \boldsymbol{\rho}(T)$, $\boldsymbol{\lambda}(0) = \boldsymbol{\lambda}(T)$ implies $z_{\rho}(T) = z_{\rho}(0)$ and $z_{\lambda}(T) = z_{\lambda}(0)$, which makes this integral a closed contour one

$$S_{\min}^{\alpha} = \left(\frac{\alpha+2}{\alpha}\right) \left(\oint_{C_{\rho}} \dot{z}_{\rho}^* dz_{\rho} + \oint_{C_{\lambda}} \dot{z}_{\lambda}^* dz_{\lambda} \right).$$

If there were only one complex variable, then the so-defined function would be analytic. Indeed, the action of two-body elliptic motion in the Newtonian potential has been evaluated using Cauchy's residue theorem in section 18.16 of [26], and in section 11.8 in [27]. With two complex variables, there is no such guarantee, however. Moreover, the residue theorem for functions of two complex variables is a more complicated matter, see [48–51].

The existence and positions of poles in this (double) contour integral are not manifest in its present form; the same integral is given by equation (D.3) in appendix D.2, $S_{\min}^{\alpha}(T) = \left(\frac{\alpha+2}{-2}\right) \int_0^T V^{\alpha}(r(t)) dt$, due to the virial theorem, however, where the potential $V^{\alpha}(r(t))$ is known to have three singularities (simple poles) at three binary collisions and the time-evolution dependence $r(t)$ of the periodic orbit, which parametrizes the contour. For the Newtonian potential $\alpha = 1$ the binary collisions are regularizable, and this integral has been studied by Sundman [28] with the result that the functions $r_k(u)$, $1 \leq k \leq 3$, are holomorphic

in a strip $|\text{Im } u| < \delta$ of the complex plane $u \in \mathbb{C}$ which contains the real axis, see section 2.3 in [29]. Since $S_{\min}^{\alpha=1}(T) = S(T) = -\left(\frac{3}{2}\right)u(T)$, we know that the trajectories $r_k(S)$, $1 \leq k \leq 3$ are holomorphic functions of the action S in a strip $|\text{Im } S| < \delta$ of the complex plane $S \in \mathbb{C}$ which contains the real axis.

Note the following implications of this result: (1) for non-singular potentials ($\alpha < 0$) there are no poles in the potential, and consequently no poles encircled by the contour, so the residue vanishes; (2) for singular potentials ($2 > \alpha > 0$) there are poles in the potential, but the residue depends on the integration contour, i.e. on the trajectory on the shape sphere and its topology w ; (3) if the integration contour, i.e. the trajectory on the shape sphere repeats k times the topologically equivalent path, then, for singular potentials ($2 > \alpha > 0$), the residue equals k times the single path residue.

Next, we switch from the real (ρ, λ) , or complex (z_ρ, z_λ) Cartesian Jacobi variables to the curvilinear hyper-spherical variables: the real hyper-radius R and the overall rotation angle $\Phi = \frac{1}{2}(\varphi_\rho + \varphi_\lambda)$, and the two angles parametrizing the shape-sphere, e.g. $(\theta = (\varphi_\rho - \varphi_\lambda), \chi = 2\text{Tan}^{-1}(\frac{\rho}{\lambda}))$. Here $(\varphi_\rho, \varphi_\lambda)$ are the angles subtended by the vectors (ρ, λ) and the x -axis. Equivalently, we may use the complex variables Z , defined by (R, Φ) and z , defined by way of a stereographic projection from the shape-sphere parametrized by (θ, χ) .

The variable Z has limited (bounded) variation for all periodic orbits (with zero angular momentum) studied in this paper. Indeed, the value of $R = |Z| = 0$ occurs only in the ‘triple collision’ (‘der Dreierstoss’) orbits, which does not happen in our case. The condition $\Phi = \text{const.}$ is trickier, however, because there are ‘relatively periodic’ solutions with vanishing angular momentum ($L = 0$) and a non-zero change $\Delta\Phi \neq 0$ of angle Φ over one period. All of the orbits considered in this paper are absolutely periodic, i.e. they have $\Delta\Phi = 0$ over one period, so this *caveat* does not apply. Therefore one may eliminate the complex variable Z from further consideration, at least for the orbits considered here, and the problem becomes (much) simpler.

Thus, we see that the complex integration contour C_z relevant to Cauchy’s theorem, $S_{\min} = 2i\pi \sum \text{Res}$, for the considered periodic orbits, is determined solely by the orbit’s trajectory on the shape sphere: the only poles relevant to this contour integral are the two-body collision points on the shape sphere. Consequently, the periodic orbits’ minimized action (integral) is determined (predominantly) by the topology of the closed contour on the shape sphere, i.e. by the homotopy group element of the periodic orbit, unless there is a closed contour in the $Z = (R, \Phi)$ variable, as well.

Repeated k -fold loops of the contour lead to k times the initial integral, i.e. $S_{\min}(w^k) = 2ki\pi \sum \text{Res} = kS_{\min}(w)$, or, equivalently $T_{\text{s.i.}}(w^k) = kT_{\text{s.i.}}(w)$, as observed in topological satellite orbits in section 3. Crossings of branch cuts²² provide for the change of residue(s) of the pole(s) at different values of k , which may account for the different values of Res, i.e. for different slopes of $T_{\text{s.i.}}(N_w)$ graphs in different sequences.

Detailed study of analytic properties of the action should be a subject of interest to pure mathematicians, however, [47].

ORCID iDs

V Dmitrašinović  <https://orcid.org/0000-0003-0192-921X>

²² We have shown in [44] that in the strong potential each of the three poles is also a logarithmic branch cut, which implies a complicated structure of branch cuts and different residues. Similar situation ought to be expected in the Newtonian potential as well.

References

- [1] Bruns E H 1887 *Acta Math.* **11** 25 (in German)
- [2] Moore C 1993 *Phys. Rev. Lett.* **70** 3675–9
- [3] Chenciner A and Montgomery R 2000 *Ann. Math.* **152** 881–901
- [4] Martynova A I, Orlov V V and Rubinov A V 2009 *Astron. Rep.* **53** 710
- [5] Šuvakov M and Dmitrašinović V 2013 *Phys.Rev.Lett.* **110** 114301
- [6] Vernić R 1953 *Hrvatsko Prirod. Društvo Clas. Mat. Fiz. Astron. Ser. 2* **8** 247–66
- [7] Arenstorf R F 1967 *Differential Equations and Dynamical Problems* ed J K Hale and J P Lasalle (London: Academic) pp 55–68
- [8] Broucke R and Boggs D 1975 *Celest. Mech.* **11** 13
- [9] Dmitrašinović V, Hudomal A, Shibayama M and Sugita A 2017 Newtonian periodic three-body orbits with zero angular momentum: linear stability and topological dependence of the period (arXiv:1705.03728v2 [physics.class-ph])
- [10] Šuvakov M 2014 *Celest. Mech. Dyn. Astron.* **119** 369–77
- [11] Iasko P P and Orlov V V 2014 *Astron. Rep.* **58** 869–79
- [12] Šuvakov M and Shibayama M 2016 *Celest. Mech. Dyn. Astron.* **124** 155–62
- [13] Rose D 2016 Geometric phase and periodic orbits of the equal-mass, planar three-body problem with vanishing angular momentum *PhD Thesis* University of Sydney (<https://ses.library.usyd.edu.au/handle/2123/14416>)
- [14] Li X and Liao S 2017 *Sci. China—Phys. Mech. Astron.* **60** 129511 (<http://numericaltank.sjtu.edu.cn/three-body/three-body.htm>)
- [15] Dmitrašinović V and Šuvakov M 2015 *Phys. Lett. A* **379** 1939–45
- [16] Birkhoff G D and Lewis D C 1933 *Ann. Mat.* **12** 117–33
- [17] Montgomery R 1998 *Nonlinearity* **11** 363–76
- [18] Tanikawa K and Mikkola S 2008 A trial symbolic dynamics of the planar three-body problem (arXiv:0802.2465)
- [19] Šuvakov M and Dmitrašinović V 2014 *Am. J. Phys.* **82** 609–19
- [20] ‘Sequences’ Institute of Physics Belgrade (<http://three-body.ipb.ac.rs/sequences.php>)
- [21] Moeckel R and Montgomery R 2015 Realizing all reduced syzygy sequences in the planar three-body problem *Nonlinearity* **28** 1919
- [22] Birkhoff G D 1935 *Mem. Pon. Acad. Sci. Novi Lyncaei* **1** 85–216
- [23] Siegel C L and Moser J K 1971 *Lectures on Celestial Mechanics* (Berlin: Springer)
- [24] Moser J K and Zehnder E J 2000 *Notes on Dynamical Systems* (Providence, RI: American Mathematical Society)
- [25] Klingenberg W 1978 *Lectures on Closed Geodesics* (Berlin: Springer)
- [26] Pars L A 1965 *Analytical Dynamics* (Portsmouth, NH: Heinemann)
- [27] Fasano A and Marmi S 2006 *Analytical Mechanics: an Introduction* (Oxford: Oxford University Press)
- [28] Sundman K F 1907 *Acta Soc. Sci. Fennicae* **34** 144–51
Sundman K F 1912 *Acta Math.* **36** 105–79 (in French)
- [29] Arnold V I, Kozlov V V and Neishtadt A I 2006 *Mathematical Aspects of Classical and Celestial Mechanics (Encyclopaedia of Mathematical Sciences Volume 3: Dynamical Systems III)* 3rd edn (Berlin: Springer)
- [30] Jacobi C G J 1843 *Vorlesungen über Dynamik* (Chelsea: Gesammelte Werke)
- [31] Landau L D and Lifshitz E M 1976 *Mechanics* 3rd edn (Oxford: Butterworth-Heinemann) section 10
- [32] Simó C 2002 *Celestial Mechanics (Contemporary Mathematics vol 292)* ed A Chenciner *et al* (dedicated to Donald Saari, Evanston, IL, 1999) (Providence, RI: American Mathematical Society) pp 209–28
- [33] Galán J, Muñoz-Almaraz F J, Freire E, Doedel E and Vanderbauwhede A 2002 *Phys. Rev. Lett.* **88** 241101
- [34] Schubart J 1956 *Astron. Nachr.* **283** 17
- [35] Hénon M 1976 *Celest. Mech.* **13** 267
- [36] Hénon M 1977 *Celest. Mech.* **15** 243
- [37] Broucke R 1979 *Astron. Astrophys.* **73** 303
- [38] Zare K and Chesley S 1998 *Chaos* **8** 475

- [39] Janković M R and Dmitrašinović V 2016 *Phys. Rev. Lett.* **116** 064301
- [40] Broucke R 1975 *Celest. Mech.* **12** 439
- [41] Hadjidemetriou J D 1975 *Celest. Mech.* **12** 155
- [42] Hadjidemetriou J D and Christides Th 1975 *Celest. Mech.* **12** 175
- [43] Hadjidemetriou J D 1975 *Celest. Mech.* **12** 255
- [44] Dmitrašinović V, Petrović L V and Šuvakov M 2017 *J. Phys. A: Math. Theor.* **50** 435102
- [45] Richter K, Tanner G and Wintgen D 1993 *Phys. Rev. A* **48** 4182
- [46] Yamamoto T and Kaneko K 1993 *Phys. Rev. Lett.* **70** 1928
- [47] Feynman R P 1999 *Feynman's Lost Lecture: the Motion of Planets Around the Sun* ed DL Goodstein and J R Goodstein (New York: W-W. Norton & Company)
- [48] Fuks B A 1963 *Theory of Analytic Functions of Several Complex Variables* (Providence, RI: American Mathematical Society)
- [49] Hörmander L 1973 *An Introduction to Complex Analysis in Several Variables* (Amsterdam: North-Holland)
- [50] Shabat B V 1992 *Introduction to Complex Analysis Part II Functions of Several Variables* (Providence, RI: American Mathematical Society)
- [51] Freitag E 2011 *Complex Analysis 2 Riemann Surfaces, Several Complex Variables, Abelian Functions, Higher Modular Functions* (Heidelberg: Springer)

Transport in optical lattices with flux

A. Hudomal¹, I. Vasić¹, H. Buljan², W. Hofstetter³, and A. Balaz̄¹

¹ *Scientific Computing Laboratory, Center for the Study of Complex Systems,
Institute of Physics Belgrade, University of Belgrade, Serbia*

² *Department of Physics, University of Zagreb, Croatia*

³ *Institut für Theoretische Physik, Johann Wolfgang Goethe-Universität, Frankfurt am Main, Germany*
e-mail: hudomal@ipb.ac.rs

Different condensed matter systems, such as electrons in a crystal lattice, can be simulated using ultracold atoms in optical lattices. Unlike electrons, atoms are electrically neutral and therefore do not feel the effects of magnetic field. Artificial gauge potentials have been recently realized in cold-atom experiments with periodically driven optical lattices [1, 2]. In such systems, atoms subjected to a constant external force gain an anomalous velocity in the direction transverse to the direction of the applied force.

Taking into consideration realistic experimental conditions, we perform numerical simulations in order to investigate the dynamics of atomic clouds and relate it to the Chern number of the effective model. We consider incoherent bosons and the full time-dependent Hamiltonian. The effects of weak repulsive interactions between atoms are taken into account using the mean-field approximation.

Our results show that driving, external force and interactions all cause heating and transitions to higher bands, which have significant effects on the dynamics. It turns out that weak interactions can be beneficial, because they make the momentum-space probability density more homogeneous. In the future, we also plan to study the details of the atomic-cloud expansion dynamics, and to simulate the full loading sequence of an initial Bose-Einstein condensate, as it was done in the experiment [2].

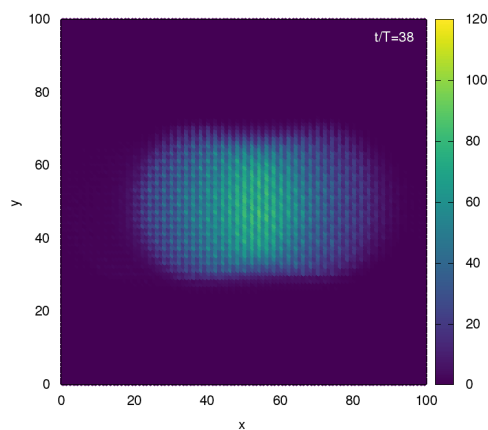


Figure 1: Density profile of an atomic cloud during expansion dynamics after release from a trap in the presence of an artificial gauge field and external force.

- [1] G. Jotzu, M. Messer, R. Desbuquois, M. Lebrat, T. Uehlinger, D. Greif, and T. Esslinger, *Nature* **515**, 237 (2014).
- [2] M. Aidelsburger, M. Lohse, C. Schweizer, M. Atala, J. T. Barreiro, S. Nascimbène, N. R. Cooper, I. Bloch, and N. Goldman, *Nat. Phys.* **11**, 162 (2015).

Q 35: Quantum Gases (Fermions) II

Tuesday 14:00–16:15

K 1.022

Talk Q 35.1 Tue 14:00 K 1.022

Artificial gauge potentials in periodically driven optical lattices: numerical simulations of atomic transport — ●ANA HUDOMAL¹, IVANA VASIĆ¹, HRVOJE BULJAN², WALTER HOFSTETTER³, and ANTUN BALAZI¹ — ¹Scientific Computing Laboratory, Center for the Study of Complex Systems, Institute of Physics Belgrade, University of Belgrade, Serbia — ²Department of Physics, University of Zagreb, Croatia — ³Institut für Theoretische Physik, Johann Wolfgang Goethe-Universität, Frankfurt am Main, Germany

Artificial gauge potentials have been recently realized in cold-atom experiments with periodically driven optical lattices [1,2]. In such systems, atoms subjected to a constant external force gain an anomalous velocity in the direction transverse to the direction of the applied force. Taking into consideration realistic experimental conditions, we perform numerical simulations in order to investigate the dynamics of atomic clouds and relate it to the Chern number of the effective model. We use the full time-dependent Hamiltonian and take into account the effects of weak repulsive interactions between atoms. The results are compared to the semiclassical approximation.

[1] G. Jotzu et al., *Nature* **515**, 237 (2014).

[2] M. Aidelsburger et al., *Nature Phys.* **11**, 162 (2015).

Talk Q 35.2 Tue 14:15 K 1.022

Experimental characterization and control of Floquet states in a periodically driven two-body quantum system — ●KILIAN SANDHOLZER, RÉMI DESBUQUOIS, MICHAEL MESSER, FREDERIK GÖRG, JOAQUÍN MINGUZZI, GREGOR JOTZU, and TILMAN ESSLINGER — Institute for Quantum Electronics, ETH Zürich, Zürich, Switzerland

Floquet engineering is a powerful tool to modify properties of a static system such as opening topological gaps or controlling magnetic order. The versatility of cold atom experiments offers the possibility to implement many of these schemes. Nonetheless, preparing a certain Floquet state that has the desired properties in this out-of-equilibrium situation is a more difficult task, especially when the driving frequency is close to a characteristic energy scale of the system. In this work, we prepare fermionic atoms in a driven optical lattice such that the system can be described by two interacting particles on a double well potential with a periodically modulated tilt. In the case of near-resonant driving we achieve to enter adiabatically individual Floquet states by using a two-step ramping protocol. In addition, the fast coherent dynamics inherently connected to the drive are studied in detail. Finally, an analytical derivation of the effective time-independent Hamiltonian of the realized system is presented and then compared to numerical studies and experimental data.

Talk Q 35.3 Tue 14:30 K 1.022

Dynamics of driven interacting many-body systems — ●MICHAEL MESSER, FREDERIK GÖRG, KILIAN SANDHOLZER, JOAQUÍN MINGUZZI, RÉMI DESBUQUOIS, and TILMAN ESSLINGER — Institute for Quantum Electronics, ETH Zurich, 8093 Zurich, Switzerland

Periodic driving can be used to coherently control the properties of a many-body state and to engineer new phases which are not accessible in static systems. The successful implementation of a periodically driven Fermi-Hubbard model on a 3D hexagonal lattice offers the possibility to explore the intriguing dynamics of Floquet many-body systems. A theoretical analysis of driven many-body Hamiltonians is inherently challenging, however, in combination with our experiments a deeper understanding seems feasible.

By controlling the detuning between shaking frequency and interactions, and setting a variable strength of the periodic drive, we achieve independent control over the single particle tunneling and the magnetic exchange energy. This control allows us to investigate the dynamics and build-up of nearest-neighbor spin-spin correlations. Furthermore, we explore possible mechanisms behind the formation of correlations in interacting Floquet systems. In addition, we can analyze the creation of double occupancies, as one mechanism to form excitations.

Talk Q 35.4 Tue 14:45 K 1.022

Enhancement and sign change of magnetic correlations in a driven quantum many-body system — ●FREDERIK GÖRG¹, MICHAEL MESSER¹, KILIAN SANDHOLZER¹, JOAQUÍN MINGUZZI¹, GREGOR JOTZU^{1,2}, RÉMI DESBUQUOIS¹, and TILMAN ESSLINGER¹ — ¹Institute for Quantum Electronics, ETH Zurich, 8093 Zurich, Switzerland — ²Max Planck Institute for the Structure and Dynamics of Mat-

ter, 22761 Hamburg, Germany

Strong periodic driving can be used to control the properties of interacting quantum systems. In solid state experiments, ultrashort laser pulses are employed to tune the charge order as well as magnetic and superconducting properties of materials. At the same time, continuous driving has been used in cold atom experiments to engineer novel effective Floquet-Hamiltonians which feature for example a topological bandstructure. We realize a strongly interacting Fermi gas in a periodically driven hexagonal optical lattice and investigate its charge and magnetic properties. We first demonstrate that in the high-frequency regime, the effective description of the many-body system by a renormalized tunnelling amplitude remains valid by comparing our results to an equivalent static system. When driving at a frequency close to the interaction energy, we show that anti-ferromagnetic correlations can be enhanced or even switched to ferromagnetic ordering. Our observations can be explained by a microscopic model, in which the particle tunnelling and magnetic exchange energies can be controlled independently. Therefore, Floquet engineering constitutes an alternative route to experimentally investigate unconventional pairing.

Talk Q 35.5 Tue 15:00 K 1.022

Manipulating and probing excitations of a Chern insulator by Floquet engineering an optical solenoid — ●BOTAO WANG, NUR ÜNAL, and ANDRÉ ECKARDT — Max Planck Institute for the Physics of Complex Systems, Dresden, Germany

The realization of artificial gauge fields in optical lattice systems has paved a way to the experimental investigation of various topological quantum effects. Here we propose a realistic scheme for realizing tunable local (solenoid type) artificial magnetic fields by means of Floquet engineering. We show that such an optical solenoid field can be used to coherently manipulate and probe Chern insulator states of the Hofstadter Hamiltonian. In particular, we investigate the possibility to create local quasiparticle and quasihole excitations, to coherently populate edge modes, and to achieve quantized charge pumping. All these effects are manifested on the spatial density distributions, which can be measured directly in quantum-gas microscopes.

Talk Q 35.6 Tue 15:15 K 1.022

Characterizing topology by dynamics: Chern number from linking number — ●MATTHIAS TARNOWSKI^{1,2}, NUR ÜNAL³, NICK FLÄSCHNER^{1,2}, BENNO REM^{1,2}, ANDRÉ ECKARDT³, KLAUS SENGSTOCK^{1,2,4}, and CHRISTOF WEITENBERG^{1,2} — ¹Institut für Laserphysik, Universität Hamburg, 22761 Hamburg, Germany — ²The Hamburg Centre for Ultrafast Imaging, 22761 Hamburg, Germany — ³Max-Planck-Institut für Physik komplexer Systeme, Nöthnitzer Straße 38, 01187 Dresden, Germany — ⁴Zentrum für Optische Quantentechnologien, Universität Hamburg, 22761 Hamburg, Germany

Topology plays an important role in modern solid state physics describing intriguing quantum states such as topological insulators. It is an intrinsically non-local property and therefore challenging to access, often studied only via the resulting edge states. Here, we report on a new approach by connecting the Chern number with the dynamical evolution of highly excited states of the system and demonstrate it experimentally with cold atoms in hexagonal optical lattices. We study the contour of dynamically created vortex pairs in momentum space following a sudden quench into the system of interest and infer the Chern number of the post-quench Hamiltonian from the topology of the contour, quantified by the linking number with the static vortices. Our work exploits a direct mapping between two topological indices and allows detecting topology by the naked eye.

Talk Q 35.7 Tue 15:30 K 1.022

1D fermionic Floquet topological insulators with Hubbard interaction — ●HAIXIN QIU¹ and JOHANN KROHA^{1,2} — ¹Physikalisches Institut and Bethe Center for Theoretical Physics, Universität Bonn, Nussallee 12, 53115 Bonn, Germany — ²Center for Correlated Matter, Zhejiang University, Hangzhou, Zhejiang 310058, China

The fermionic Rice-Mele model is a standard model for quantum ratchet transport in periodically driven, one-dimensional, bipartite chains. In the adiabatic limit, this model exhibits quantized transport (Thouless pump), while in the limit of fast drive quasistatic approximations with effective hopping parameters are possible. Here we study the Rice-Mele model with periodic drive of both, the hopping amplitudes and the onsite energy modulation, in the intermediate regime

Topological Matter in Artificial Gauge Fields

[Home](#)[Scientific Program](#)[Participants](#)[Poster Contributions](#)[Useful information](#)[Social Events](#)[Scientific Report](#)

For each poster contribution there will be one poster wall (width: 97 cm, height: 250 cm) available. Please do not feel obliged to fill the whole space. Posters can be put up for the full duration of the event.

POSTER	
Sonic Landau levels and synthetic gauge fields in mechanical metamaterials <i>Abbaszadeh, Hamed</i>	+
Probing quantum turbulence in He II by quantum evaporation measurements <i>Amelio, Ivan</i>	+
Topology and dynamics in driven hexagonal lattices <i>Asteria, Luca</i>	+
Spin-orbitcoupling in a Bose-Einstein condensate: Triple-well in momentum space <i>Cabedo Bru, Josep</i>	+
Tailoring the Fermi velocity in 2D Dirac Materials <i>Diaz Fernández, Álvaro</i>	+
A new machine for dysrosium experiment <i>Du, Li</i>	+
Exact Edge and Bulk States of Topological Models and their Robustness Against an Impurity <i>Duncan, Callum</i>	+
Enhanced chiral anomaly in Floquet Schwinger model <i>Ebihara, Shu</i>	+
Synthetic dimensions and chiral currents with spin-orbit-coupled two-electron ultracold fermions <i>Franchi, Lorenzo</i>	+
Realizing and detecting a topological insulator in the AIII symmetry class <i>García Velasco, Carlos</i>	+
Real and imaginary part of conductivity of strongly interacting bosons in optical lattices <i>Grygiel, Barbara</i>	+
Topological Phases in Ultracold Fermionic Ladders <i>Haller, Andreas</i>	+
Characterizing interacting topological states of matter via charge pumps and single-particle topological invariants <i>Hayward, Andrew</i>	+
Transport in optical lattices with flux <i>Hudomal, Ana</i>	
Recent cold atom experiments have realized artificial gauge fields in periodically modulated optical lattices [1,2]. We study the dynamics of atomic clouds in these systems by performing numerical simulations using the full time-dependent Hamiltonian and comparing these results to the semiclassical approximation. Under constant external force, atoms in optical lattices with flux exhibit an anomalous velocity in the transverse direction. We investigate in detail how this transverse drift is related to the Berry curvature and Chern number, taking into account realistic experimental conditions. [1] G. Jotzu et al., Nature 515, 237 (2014). [2] M. Aidelsburger et al., Nature Phys. 11, 162 (2015).	
Time-periodic driving of spinor condensates in a hexagonal optical lattice <i>Ilin, Alexander</i>	
Local topological invariant of the Interacting Hofstadter Interface	

Transport dynamics in optical lattices with flux

A. Hudomal¹, I. Vasić¹, H. Buljan², W. Hofstetter³, and A. Balaž¹

¹*Scientific Computing Laboratory, Center for the Study of Complex Systems,
Institute of Physics Belgrade, University of Belgrade, Serbia*

²*Department of Physics, University of Zagreb, Croatia*

³*Institut für Theoretische Physik, Johann Wolfgang Goethe-Universität,
Frankfurt am Main, Germany
e-mail:ana.hudomal@ipb.ac.rs*

Recent cold atom experiments have realized artificial gauge fields in periodically modulated optical lattices [1,2]. We study the dynamics of atomic clouds in such systems by performing numerical simulations using the full time-dependent Hamiltonian and compare results with the semiclassical approximation. Under constant external force, atoms in optical lattices with flux exhibit an anomalous velocity in the transverse direction. We investigate in detail how this transverse drift is related to the Berry curvature and Chern number, taking into account realistic experimental conditions.

REFERENCES

- [1] G. Jotzu, M. Messer, R. Desbuquois, M. Lebrat, T. Uehlinger, D. Greif, T. Esslinger, *Nature* **515**, 237 (2014).
- [2] M. Aidelsburger, M. Lohse, C. Schweizer, M. Atala, J. T. Barreiro, S. Nascimbène, N. R. Cooper, I. Bloch, N. Goldman, *Nat. Phys.* **11**, 162 (2015).

the Feshbach resonance.

Poster Q 53.10 Thu 17:00 P OG2
Spin and Charge Correlation Measurements in the 2D Hubbard Model — JAN DREWES¹, LUKE MILLER^{1,2}, EUGENIO COCCHI^{1,2}, CHUN FAI CHAN¹, NICOLA WURZ¹, ●MARCELL GALL¹, DANIEL PERTOT¹, FERDINAND BRENECKE¹, and MICHAEL KÖHL¹ — ¹Physikalisches Institut, University of Bonn, Wegelerstrasse 8, 53115 Bonn, Germany — ²Cavendish Laboratory, University of Cambridge, JJ Thomson Avenue, Cambridge CB3 0HE, United Kingdom

We experimentally study the emergence of correlations in an ultracold, fermionic 2D lattice system, representing a realisation of the Hubbard model. Our ability to precisely tune the system parameters over a large range and the possibility to simultaneously detect the density distribution of both spin components in-situ enables us to examine the emergence of density and spin correlations as a function of doping interaction strength and temperature. In addition we gain from the measurement of the equation of state insight into the full thermodynamics of the 2D Hubbard model. To improve our preparation and detection capabilities, we use a spin spiral technique which allows us to detect the spin structure factor at arbitrary wave vectors. Further we employ a spatial light modulator to reshape the underlying trapping potential of the optical lattice to realize the homogeneous Hubbard model and reach lower temperatures by redistributing entropy between different spatial regions.

Poster Q 53.11 Thu 17:00 P OG2
BEC of ⁴¹K in a Fermi Sea of ⁶Li — RIANNE S. LOUS^{1,2}, ISABELLA FRITSCHKE^{1,2}, ●FABIAN LEHMANN^{1,2}, MICHAEL JAG^{1,2}, EMIL KIRILOV^{1,2}, BO HUANG¹, and RUDOLF GRIMM^{1,2} — ¹IQOQI, Austrian Academy of Science, Innsbruck, Austria — ²Inst. for Experimental Physics, University of Innsbruck, Innsbruck, Austria

We report on the production of a double-degenerate Fermi-Bose mixture of ⁶Li and ⁴¹K. In our experimental sequence the potassium atoms are sympathetically cooled by the lithium atoms, which are evaporatively cooled in an optical dipole trap. We obtain 10⁴ ⁴¹K atoms with a BEC fraction close to 1 and a $T/T_F \approx 0.05$ with 10⁵ ⁶Li atoms in each spin state. To measure the temperature of our fermionic sample we use the ⁴¹K BEC as a tool for thermometry. As the system is in thermal equilibrium we evaluate the condensed fraction of our ⁴¹K atoms and extract the temperature of the atoms. To investigate the properties of the ⁶Li-⁴¹K mixture near the inter-species Feshbach resonance at 335.8 G we use another scheme of evaporation around 300 G which enables us to achieve similar temperatures. We explore both the repulsive side and attractive side of the Feshbach resonance and observe phase separation for strong repulsive interactions and collapse for attractive interactions. This work is supported by the Austrian Science Fund FWF within the SFB FoQuS.

Poster Q 53.12 Thu 17:00 P OG2
Probing Many-body physics with an ultra-narrow clock transition in an Ytterbium quantum gas — ●BODHADITYA SANTRA¹, BENJAMIN ABELN¹, BASTIAN HUNDT¹, ANDRÉ KOCHANKE¹, THOMAS PONATH¹, ANNA SKOTKE¹, KLAUS SENGSTOCK^{1,2}, and CHRISTOPH BECKER^{1,2} — ¹Zentrum für Optische Quantentechnologien, Universität Hamburg, Luruper Chaussee 149, 22761 Hamburg, Germany — ²Institut für Laserphysik, Universität Hamburg, Luruper Chaussee 149, 22761 Hamburg, Germany

During the last decade ultracold fermionic alkaline earth quantum gas attracted a lot of attention due to their unique properties such as long-lived meta-stable state, an ultra-narrow optical clock transition, SU(N) symmetric interactions as well as the existence of an interorbital Feshbach resonance. In particular fermionic Yb quantum gas allow for quantum simulation of lattice systems with orbital degrees of freedom, like the Kugel-Khomskii model or the Kondo lattice model (KLM).

We will present recent progress of the Hamburg Yb experiment towards realizing the KLM and correlated KLM, including measurements on spin polarized as well as on interacting Fermi gases with an improved clock laser setup.

This work is supported by the DFG within the SFB 925 and the Marie Curie Initial Training Network QTea.

Poster Q 53.13 Thu 17:00 P OG2
Local control of transport in an atomic quantum wire: from one scanning gate to a finite size lattice — ●SAMUEL HÄUSLER¹, MARTIN LEBRAT¹, DOMINIK HUSMANN¹, LAURA CORMAN¹, SEBASTIAN KRINNER¹, SHUTA NAKAJIMA², JEAN-PHILIPPE BRANTUT¹, and TILMAN ESSLINGER¹ — ¹Institute for Quantum Electronics, ETH

Zürich, 8093 Zürich, Switzerland — ²Department of Physics, Graduate School of Science, Kyoto University, Kyoto 606-8502, Japan

Building on the holographic shaping of optical potentials and a high-resolution microscope, we demonstrate the local control of fermionic lithium atoms flowing through a one-dimensional structure. We first image the transport through a quantum wire, in a way similar to the scanning gate technique applied to solid state devices. By scanning the position of a sharp, repulsive optical gate over the wire and measuring the subsequent variations of conductance, we spatially map the transport at a resolution close to the transverse wavefunction inside the wire. The control of the gate at the scale of the Fermi wavelength makes it sensitive to quantum tunnelling. Furthermore, our knowledge of the optical potential allows a direct comparison of the experimental maps with a numerical and an analytical model for non-interacting particles.

The flexibility offered by our setup makes it relatively simple to imprint more complex structures. By projecting several consecutive scatterers, a lattice of variable length can be built inside the quantum wire. This opens the path to study metal-insulator physics with strong attractive interactions.

Poster Q 53.14 Thu 17:00 P OG2
Interacting Anyons in a One-Dimensional Optical Lattice — ●MARTIN BONKHOF, KEVIN JÄGERING, SEBASTIAN EGGERT, and AXEL PELSTER — State Research Center OPTIMAS and Fachbereich Physik, Technische Universität Kaiserslautern, 67663 Kaiserslautern, Germany

We analyze in detail the properties of the one-dimensional Anyon-Hubbard model, which can be mapped to a corresponding Bose-Hubbard model with a density-dependent Peierls phase via a generalized Jordan-Wigner transformation [1]. At first we extend the modified version of the classical Gutzwiller-mean-field ansatz of Ref. [2] in order to obtain the pair-correlation function for both the bosonic and the anyonic system. A comparison of the resulting quasi-momentum distributions with high-precision DMRG calculations reveals in general a parity breaking, which is due to anyonic statistics. Afterwards, we determine how the boundary of the superfluid-Mott quantum phase transition changes with the statistical parameter. We find in accordance with Ref. [1] that the statistical interaction has the tendency to destroy superfluid coherence.

[1] T. Keilmann, S. Lanzmich, L. McCulloch, and M. Roncaglia, Nat. Commun. **2**, 361 (2011)

[2] G. Tang, S. Eggert, and A. Pelster, New J. Phys. **17**, 123016 (2015)

Poster Q 53.15 Thu 17:00 P OG2
Creating topological interfaces and detecting chiral edge modes in a two-dimensional optical lattice — ●FREDERIK GÖRG¹, NATHAN GOLDMAN², GREGOR JOTZU¹, MICHAEL MESSER¹, KILIAN SANDHOLZER¹, RÉMI DESBUQUOIS¹, and TILMAN ESSLINGER¹ — ¹Institute for Quantum Electronics, ETH Zurich, Zurich, Switzerland — ²CENOLI, Université Libre de Bruxelles, Brussels, Belgium

The appearance of topological properties in lattice systems caused by a non-trivial topological band structure in the bulk is closely related to the existence of chiral edge modes via the bulk-edge correspondence. These edge states appear at the interface of two spatial regions with a distinct topology, which for example naturally arise at the boundaries of a sample surrounded by vacuum. In cold atom systems, these edge modes are difficult to detect, since the underlying harmonic trapping potential does not feature sharp boundaries. Therefore, we propose a different method to design topological interfaces within the bulk of the system. We illustrate this scheme by an optical lattice realization of the Haldane model, where a spatially varying lattice beam leads to the appearance of distinct topological phases in separated regions of space. The versatility of the method allows to tune the position, the localization length and the chirality of the edge modes. We numerically study the propagation of wave packets in such a system and demonstrate the feasibility to experimentally detect chiral edge states. Finally, we show that the edge modes, unlike the bulk states, are topologically protected against the effects of disorder, which makes a random potential a powerful tool to detect edge states in cold atom setups.

Poster Q 53.16 Thu 17:00 P OG2
Transport dynamics in optical lattices with flux — ●ANA HUDOMAL¹, IVANA VASIĆ¹, WALTER HOFSTETTER², and ANTUN BALAZ¹ — ¹Scientific Computing Laboratory, Center for the Study of Complex Systems, Institute of Physics Belgrade, University of Belgrade, Serbia — ²Institut für Theoretische Physik, Johann Wolfgang Goethe-Universität, Frankfurt am Main, Germany

Recent cold atom experiments have realized artificial gauge fields in periodically modulated optical lattices [1,2]. We study the dynamics of atomic clouds in these systems by performing numerical simulations using the full time-dependent Hamiltonian and comparing these results to the semiclassical approximation. Under constant external force, atoms in optical lattices with flux exhibit an anomalous velocity in the transverse direction. We investigate in detail how this transverse drift is related to the Berry curvature and Chern number, taking into account realistic experimental conditions.

[1] G. Jotzu et al., *Nature* **515**, 237 (2014).

[2] M. Aidelsburger et al., *Nature Phys.* **11**, 162 (2015).

Poster Q 53.17 Thu 17:00 P OG2
Towards the investigation of collective scattering in nanofiber-trapped atomic ensembles — ●ADARSH S. PRASAD, JAKOB HINNEY, SAMUEL RIND, PHILIPP SCHNEEWEISS, JÜRGEN VOLZ, CHRISTOPH CLAUSEN, and ARNO RAUSCHENBEUTEL — TU Wien - Atominstitut, Stadionallee 2, 1020 Wien, Austria

We realize an efficient optical interface between guided light and laser-cooled atoms which are arranged in two linear arrays in a two-color evanescent-field dipole trap created around an optical nanofiber [1]. In this configuration, the probability of a nanofiber-guided photon being absorbed and then re-emitted into free space by a trapped atom is as high as 10%. For a periodic array of atoms, interference of the fields scattered by different atoms result in a collective emission into a cone with a well-defined angle with respect to the fiber axis. We plan to study this collective emission and its dependence on various experimental parameters. The next step will be to adjust the periodicity of the atomic array to fulfill the Bragg condition such that fiber-guided light is strongly back-reflected [2]. Here, the interaction between the atomic array and the fiber-guided light depends strongly on the polarization of the light field. In particular, light that is polarized in (orthogonal to) the plane of atoms will be weakly (strongly) reflected. We want to implement such highly reflecting atomic arrays, which could then be used to implement cavity quantum electrodynamics experiments in which the resonator itself is made of quantum emitters.

[1] E. Vetsch et al., *Phys. Rev. Lett.* **104**, 203603 (2010).

[2] Fam Le Kien et. al., *Phys. Rev. A* **90**, 063816 (2014).

Poster Q 53.18 Thu 17:00 P OG2
Setup of a new micro-structured linear Paul trap with integrated solenoids and reduced axial micromotion — ●H. SIEBENEICH, D. KAUFMANN, T. GLOGER, P. KAUFMANN, M. JOHANNING, and CH. WUNDERLICH — Department Physik, Universität Siegen, 57068 Siegen, Germany

We present the status of a new 3d segmented ion trap setup with integrated solenoids, in which an improved design allows for a substantial reduction of axial micromotion and for an increased magnetic gradients. Our trap consists of three layers of gold plated alumina, where the segmented outer layers provide the trapping potentials [1], and the middle layer contains solenoids that are used to create a magnetic field gradient [2]. The gradient gives rise to coupling between the ions' internal and motional states. The trap is mounted on a ceramic chip carrier that, at the same time, acts as an ultra-high vacuum interface, featuring about 100 thick-film printed current and voltage feedthroughs. The thick film interface has been improved by replacing previously used Ag-Pd layers by Au layers which reduced their resistivity by a factor of eight. The previously high resistivity used to be a bottleneck for achieving high solenoid currents and thus a magnetic gradient. The shape of the solenoids was redesigned, leading to an expected reduction of axial micromotion by four orders of magnitudes.

[1] S.A. Schulz et al.: Sideband cooling and coherent dynamics in a microchip multi-segmented ion trap, *New Journal of Physics*, Volume 10, April 2008 [2] D. Kaufmann et al.: Thick-film technology for ultra high vacuum interfaces of micro-structured traps, *Appl Phys B* (2012) 107:935-943

Poster Q 53.19 Thu 17:00 P OG2
Design and construction of a Perpetual Atom Laser Machine — ●CHUN-CHIA CHEN, SHAYNE BENNETTS, BENJAMIN PASQUIOU, and FLORIAN SCHRECK — Institute of Physics, University of Amsterdam, Amsterdam, The Netherlands

We have developed a machine aimed at producing a perpetual atom laser, a long standing goal within atomic physics. Continuous production of Bose-Einstein condensate (BEC) or an atom laser requires two incompatible cooling processes, laser cooling a gas sample, then cooling evaporatively until degeneracy is reached. In order to produce a perpetual output these stages take place simultaneously in different

parts of our machine. To protect the condensate from scattered photon heating we use a combination of physical separation, baffles and a "transparency" beam. Our machine has now demonstrated a perpetual MOT of 2×10^9 ^{88}Sr atoms with temperatures as low as $20\mu\text{K}$ on a 7.4-kHz wide laser cooling transition with a continuous loading rate of 7×10^8 atoms/s. Using a different set of parameters and location we have also demonstrated a perpetual MOT of 2×10^8 ^{88}Sr at $2\mu\text{K}$ with a loading rate of 9×10^7 atoms/s which we have successfully loaded into a dipole trap. By switching to the 0.5% abundance ^{84}Sr isotope we are able to evaporate to BECs of 3×10^5 ^{84}Sr atoms. Critically, for the second location we have validated the effectiveness of our architecture in protecting a BEC from scattered broad-linewidth laser cooling light, which is used in the first cooling stages. We will describe our design and the performance demonstrated so far.

Poster Q 53.20 Thu 17:00 P OG2
Optical trapping of neutral mercury — ●HOLGER JOHN and THOMAS WALTHER — Technische Universität Darmstadt, Institut für Angewandte Physik, Schlossgartenstraße 7, 64289 Darmstadt

Laser-cooled mercury constitutes an interesting starting point for various experiments, in particular in light of the existence of bosonic and fermionic isotopes. On the one hand the fermionic isotopes could be used to develop a new time standard based on an optical lattice clock employing the $^1S_0 - ^3P_0$ transition. Another interesting venue is the formation of ultra cold Hg-dimers employing photo-association and achieving vibrational cooling by employing a special scheme.

The laser system is based on an interference-filter stabilized external cavity diode laser with excellent spectral properties combined with a home built non-cryogenic fiber amplifier for the 1015nm fundamental wavelength with a slope-efficiency of more than 35% delivering up to 4W of pump limited output power. The fundamental wavelength is frequency doubled twice to reach the cooling transition at 253.7nm. The challenging requirements meeting the natural linewidth of 1.27 MHz are mastered by use of a ULE reference resonator.

After integrating a 2D-MOT as an atom source to the vacuum system the first measurements of ultra-cold atoms with the new laser system will be reported.

Poster Q 53.21 Thu 17:00 P OG2
Diffusion of Single Atoms in Bath — ●DANIEL ADAM, FARINA KINDERMANN, TOBIAS LAUSCH, DANIEL MAYER, FELIX SCHMIDT, STEVE HAUPT, MICHAEL HOHMANN, NICOLAS SPETHMANN, and ARTUR WIDERA — TU Kaiserslautern, Department of Physics, Kaiserslautern, Germany

Diffusion is an essential phenomenon occurring in various systems such as biological cells, traffic models or stock markets. While most systems are well described by standard Brownian motion, anomalous diffusion can lead to markedly different dynamical properties.

Experimentally, we study the diffusion of individual atoms illuminated by near-resonant light and trapped in a periodic potential. All relevant parameters such as damping coefficient and potential height can be controlled in order to realize different diffusive regimes.

We explore the amount of information contained in the Kramers rate, i. e. the rate at which a diffusing atom can escape from a potential well. Furthermore we exploit the excellent control over the optical trapping potential and study the diffusion of the atom in a time-varying periodic trap, complemented by numerical simulations of the dynamics.

Poster Q 53.22 Thu 17:00 P OG2
Kinetic Monte Carlo simulation of percolation in driven-dissipative Rydberg gases — ●STEPHAN HELMRICH, PHILIPP FABRITIUS, GRAHAM LOCHHEAD, and SHANNON WHITLOCK — Physikalisches Institut, Universität Heidelberg, Im Neuenheimer Feld 226, 69120 Heidelberg

Directed percolation is perhaps the most prominent example of a unique class of phenomena which exhibit genuine non-equilibrium phase transitions and non-trivial critical behaviour. We explore whether highly tunable gases of ultracold atoms excited to long-range interacting Rydberg states can serve as a clean experimental realisation of percolation phenomena in two and three dimensions. The mechanism investigated is the cooperative excitation of Rydberg atoms triggered when the excitation laser is resonant for atoms within a characteristic distance of another Rydberg atom (facilitated excitation). To simulate the dynamics of this system we use a kinetic Monte Carlo algorithm which is able to reproduce many of the experimental features of laser excited Rydberg gases. We investigate the scaling behavior for the fraction of Rydberg excitations (active sites) and their spa-

26th INTERNATIONAL CONFERENCE ON ATOMIC PHYSICS

22
27
JULY



CERTIFICATE

This document certifies that:

Ana Hudomal

has presented the poster entitled

Transport in optical lattices with flux

and authored by

Ana Hudomal; Ana Hudomal; Ivana Vasic; Hrvoje Buljan; Walter Hofstetter; Antun Balaz

at the 26th International Conference on Atomic Physics,
held at the Barcelona Conference Center from July 22nd to July 27th, 2018.

Barcelona, July 27th, 2018

Prof. Verónica Ahufinger
(Vice-chair)

Prof. Maciej Lewenstein
(Chair)

Prof. Bruno Juliá-Díaz
(Vice-chair)





**SUMMER
SCHOOL**

16 - 20
JULY
Barcelona, Spain

CERTIFICATE

This document certifies that:

Ana Hudomal

has attended and participated with the Poster entitled

Transport in optical lattices with flux

at the ICAP 2018 Summer school, held at the University of Barcelona, Faculty of
Physics & Chemistry from July 16th to July 20th 2018.

Barcelona, 20th July, 2018



Prof. Verònica Ahufinger
(Vice-chair)



Prof. Maciej Lewenstein
(Chair)



Prof. Bruno Juliá-Díaz
(Vice-chair)





Република Србија
Универзитет у Београду
Физички факултет
Д.Бр.2015/8006
Датум: 29.10.2018. године

На основу члана 161 Закона о општем управном поступку и службене евиденције издаје се

УВЕРЕЊЕ

Худомал (Франц) Ана, бр. индекса 2015/8006, рођена 08.03.1991. године, Београд, Београд-Савски Венац, Република Србија, уписана школске 2018/2019. године, у статусу: самофинансирање; тип студија: докторске академске студије; студијски програм: Физика.

Према Статуту факултета студије трају (број година): три.
Рок за завршетак студија: у двоструком трајању студија.

Ово се уверење може употребити за регулисање војне обавезе, издавање визе, права на дечији додаток, породичне пензије, инвалидског додатка, добијања здравствене књижице, легитимације за повлашћену возњу и стипендије.



Овлашћено лице факултета

[Handwritten signature]



Република Србија

УБ

Универзитет у Београду
Физички факултет, Београд



Оснивач: Република Србија

Дозволу за рад број 612-00-02666/2010-04 од 10. децембра 2010.
године је издало Министарство просвете и науке Републике Србије

Диплома

Ана, Франц, Худомал

рођена 8. марта 1991. године у Београду, Савски венац, Република Србија, уписана
школске 2010/2011. године, а дана 23. јула 2014. године завршила је основне академске
студије, првог степена, на студијском програму Теоријска и експериментална физика,
обима 240 (двеста четрдесет) бодова ЕСПБ са просечном оценом 10,00 (десет и 0/100).

На основу тога издаје јој се ова диплома о стеченом високом образовању и стручном називу

дипломирани физичар

Број: 5401600

У Београду, 27. маја 2016. године

Декан
Проф. др Јаблан Дојчиловић

Ректор
Проф. др Владимир Бумбаширевић

00054415



Република Србија

УБ

Универзитет у Београду
Физички факултет, Београд



Оснивач: Република Србија

Дозволу за рад број 612-00-02666/2010-04 од 10. децембра 2010.
године је издало Министарство просвете и науке Републике Србије

Диплома

Ана, Франц, Худомал

рођена 8. марта 1991. године у Београду, Савски венац, Република Србија, уписана
школске 2014/2015. године, а дана 12. октобра 2015. године завршила је мастер
академске студије, другог степена, на студијском програму Теоријска и експериментална
физика, обима 60 (шездесет) бодова ЕСПБ са просечном оценом 10,00 (десет и 0/100).

На основу тога издаје јој се ова диплома о стеченом високом образовању и академском називу

мастер физичар

Број: 5401500

У Београду, 27. маја 2016. године

Декан

Проф. др Јаблан Дојчиловић

Ректор

Проф. др Владимир Бумбаширевић

00054416

**ДОКТОРСКЕ СТУДИЈЕ****ПРЕДЛОГ ТЕМЕ ДОКТОРСКЕ ДИСЕРТАЦИЈЕ
КОЛЕГИЈУМУ ДОКТОРСКИХ СТУДИЈА**Школска година
2018/2019**Подаци о студенту**

Име

Ана

Презиме

Худомал

Број индекса

8006/2015

Научна област дисертације

физика кондензоване материје и
статистичка физика**Подаци о ментору докторске дисертације**

Име

Ивана

Презиме

Васић

Научна област

физика кондензоване материје
и статистичка физика

Звање

виши научни сарадник

Институција

Институт за физику у Београду

Предлог теме докторске дисертације

Наслов

Numerical study of quantum gases in optical lattices with flux

(Нумеричко проучавање квантних гасова у оптичким решеткама са флуksom)

Уз пријаву теме докторске дисертације Колегијуму докторских студија, потребно је приложити следећа документа:

1. Семинарски рад (дужине до 10 страница)
2. Кратку стручну биографију писану у трећем лицу јединине
3. Фотокопију индекса са докторских студија

Датум	<input type="text" value="24.10.2018."/>	Потпис ментора	<input type="text" value="M. Banti"/>
		Потпис студента	<input type="text" value="Ana Rudomal"/>

Мишљење Колегијума докторских студија

Након образложења теме докторске дисертације Колегијум докторских студија је тему

прихватио није прихватио

Датум

Продекан за науку Физичког факултета